UNIVERSITY OF PADUA

DEPARTMENT OF CIVIL, ENVIRONMENTAL AND ARCHITECTURAL ENGINEERING

Master's Degree in Water and Geological Risk Engineering

MASTER THESIS

Integrated Surface – Subsurface Hydrological Modeling of An Agricultural Plot Affected by Salinization

Supervisor:

Associate Professor Matteo Camporese

Graduate: Muhammad Khalif Arda

Student ID. 2042278

ACADEMIC YEAR 2023-2024

ABSTRACT

Understanding the hydraulic properties of the vadose zone, crucial for understanding water movement dynamics in agricultural areas with diverse soil characteristics. Catchment hydrology (CATHY) is considered as an effective tool for the estimation of soil-water dynamic behaviours comparing to field observations such as volumetric water content (VWC), soil-water pressure head (ψ) and groundwater table (h). The laboratory-derived results underwent rigorous validation through the Rosetta model and the Multipoint Triangle method. The primary aim of this study is to incorporate both hydraulic and Van Genuchten (VGM) parameters in the simulation and to optimize each parameter to achieve the best model performance by calibrating the model through SCE-UA method in the research site area of a 21-ha agricultural field situated along the southern edge of the Venice Lagoon affected by salinization. The calibration was aimed at optimizing three variables of pressure head, water content, and water table at the same time, which is very challenging. As the results, the model produces calibrated hydraulic and VGM parameters with hydraulic conductivity (K_s) of silt loam of 22.4 cm/day,porosity (θ_s) of 0.367, n of 1.28, residual porosity (θ_r) of 0.0912, and inverse α of 0.229. Furthermore, the CATHY simulation provides insight into soil-water dynamics. The simulations of water content dynamics reveal discrepancies across borehole, with notable underestimations observed, particularly at certain depths. Challenges also arise in replicating pressure head fluctuations due to data gaps. In water table comparisons, it initially shows underestimations but gradually increase over time. Statical analysis of Kling-Gupta Efficiency (KGE) index highlights varied model performance, emphasizing the importance of continuous data collection and comprehensive modeling approaches for understanding and managing hydrological processes of soil-water dynamics in heterogeneous geological environments. Overall, ongoing efforts are essential to enhance the model's accuracy in capturing soil-water dynamics in the vadose zone.

Keywords: CATHY, soil-water dynamic, KGE index, hydraulic parameter, VGM parameters, SCE-UA method, Rosetta model

ACKNOWLEDGEMENTS

Praise and gratitude to Allah سبحانه و تعالى for His blessings and His grace so that this master's thesis can be completed well. Master thesis entitled "Integrated Surface-Subsurface Hydrological Modelling of An Agricultural Plot Affected by Salinization" was prepared to fulfill the academic requirements for completion of the Master's Program in Water and Geological Risk Engineering, Department of Civil, Environmental and Architectural Engineering, University of Padua. The support of various parties was very helpful in preparing this thesis. Therefore, the author expresses his sincere thanks to:

1. Parents and family for the prayers, love, advice, understanding, attention both moral and material, and encouragement that have been given.
2. Professor Matteo Camporese, Ph.D. as supportive thesis supervisor for all the guidance, learning, insights, patience and support that have been invaluable in shaping this work.
3. All my friends for the support and encouragement.

CONTENTS

List of Tables

LIST OF FIGURES

CHAPTER 1

1. INTRODUCTION

1.1 GROUNDWATER HYDROLOGY OVERVIEW

The circulation of water in the atmosphere, land and ocean is called the hydrologic cycle. Figure 1 illustrates the flow-system concept of the hydrologic cycle. The hydrologic cycle includes evaporation, precipitation, condensation, runoff and groundwater flow. Evapotranspiration is the consequence of a complicated interaction between the atmosphere, soil, and plants. The hydrologic cycle and the energy balance are both affected by changes in land use and climate. Despite the numerous complicated processes and interactions involved in evapotranspiration, it is more a consideration that available energy and water are the fundamental determinants of evapotranspiration rate [4].

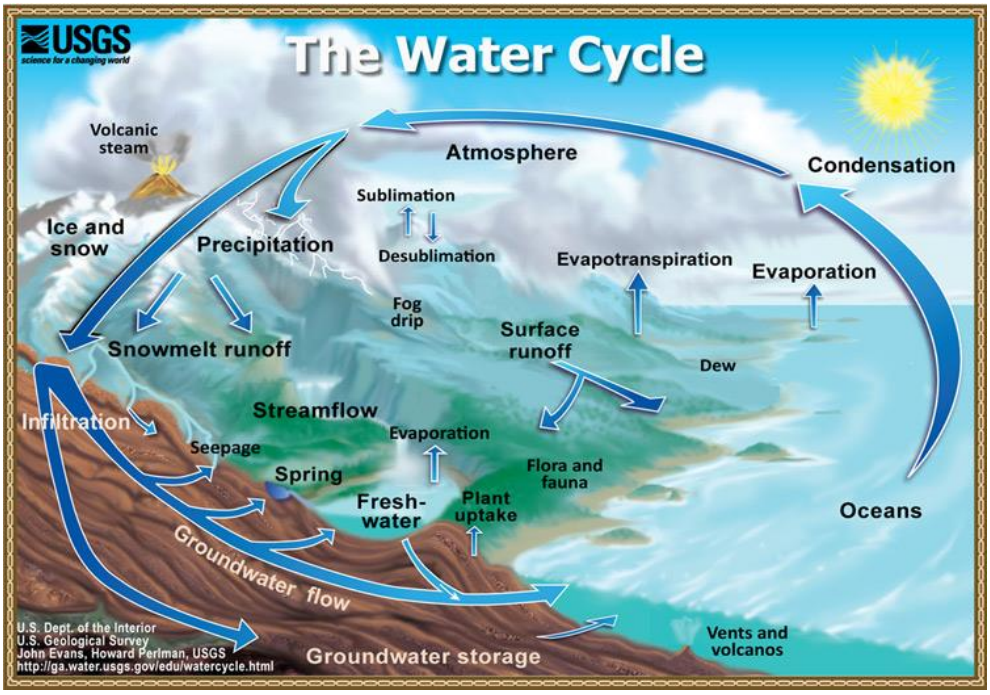

Figure 1. Hydrologic cycle (Source: U.S.G.S)

When the average annual volumes of worldwide terrestrial evapotranspiration and runoff are compared, it shows that annual terrestrial evapotranspiration is currently around 54 percent bigger than annual runoff out of the continents [36].

The streamflow reflects changes in the terrestrial hydrologic cycle, influenced by both spatial and temporal variations. It mirrors short-term weather patterns and precipitation fluctuations over days to weeks. Additionally, it signifies the water passing through aquifers and dams, known as the "water yield" which is the portion of precipitations not lost to evapotranspiration. Over longer periods, typically spanning years, streamflow captures changes in catchment storage, albeit relatively smaller compared to overall water flow. The average water flux that can be used for human benefit in a sustainable manner is represented by the water yield.

In drylands, vegetation influences the water cycle by factors like soil surface protection and habitat creation for soil organisms, rather than directly altering infiltration capacity. These vegetation-infiltration dynamics are increasingly incorporated into hydrological models to predict rainfall-runoff, soil moisture, vegetation changes, and dryland geomorphology.

Despite the fact that there is a clear link between average evapotranspiration and streamflow, a lot of researches have looked at both fluxes at the same time. Estimation of the water balance is a complicated task since some of its constituents, especially changes in groundwater storage, are difficult to measure directly and are often estimated indirectly through various hydrological models or using empirical methods. Empirical methods have been developed for the computation of various water budget components, such as evapotranspiration (ET), groundwater recharge (GR) and surface runoff.

Groundwater, ranking as the world's second largest freshwater reservoir after surface water, plays a crucial role in supplying the drinking water, supporting agriculture and sustaining industrial purposes. Its global significance extends to ensuring water supply, ecosystem stability and human welfare. Furthermore, the overall importance is expected to grow as its resilience against seasonal and multi-year climate variability than surface water. Increasing groundwater demand to supply drinking water, agriculture and industry in combination with climate change has highlighted the importance of groundwater protection [14]. Timely detection of negative groundwater level trends is crucial to make appropriate decisions and ensure sustainable groundwater management [1], while reliable information on groundwater levels is a prerequisite prior any groundwater resources assessment [34].

Groundwater flow represents a crucial aspect of complex dynamic hydrologic cycle. Beneath the Earth's surface, saturated layers below the surface act as conduits for the transmission of groundwater, and as reservoirs for water storage. Water infiltrates to these formations from the surface and is transmitted slowly for varying distances until it returns

to the surface by action of natural flow, vegetation, or man [37]. Groundwater exists in the in two main zones underground: the unsaturated zone, also called as the vadose zone, comprising soil pores containing varying mixtures of air and water, and the saturated zone, where water-filled pores are under hydrostatic pressure. In unconfined aquifers, the saturated zone is overlain by an unsaturated zone extending from the water table to the ground surface.

Understanding the hydraulic properties of the vadose zone is essential for comprehending the dynamics of water movement, especially in agricultural areas with diverse soil characteristics. Soil hydraulic properties such as soil water retention and hydraulic conductivity can be directly estimated by laboratory techniques applied on relatively small soil samples. However, these methods are time-consuming and results are strongly affected by the sample dimensions [27].

Seawater intrusion in coastal areas is threatening groundwater quality and farmland productivity worldwide [23]. This phenomenon naturally occurs in coastal areas [34] but is actually intensified by anthropogenic activities such as groundwater pumping or land-use change [9]. A significant land subsidence affected the farmland at the southern margin of the Venice Lagoon due to a larger natural geological subsidence mainly exacerbated by peat oxidation [16] and, secondarily, groundwater withdrawal and clay sediment salinization induced by salt-water intrusion [41]. The area is kept suitable for farming by a drainage system that collects the surface water and pumps the excess water into the lagoon [11]. Several sandy paleochannels crossing the farmland provide a hydraulic connection between freshwater aquifers and the lagoon and thus facilitate seawater intrusion and freshwater dispersion [24].

Integrated surface-subsurface hydrological models (ISSHMs) are useful for simulating the terrestrial water cycle and the spatiotemporal variability of its components in catchments with a detailed resolution of topography [8]. ISSHMs commonly feature a Richards equation-based description of variably saturated subsurface flow coupled with a de Saint Venant equation-based description of routing for overland and channel flow [7]. The CATHY model combines the three-dimensional (3-D) Richard's equation for subsurface flow in variably saturated porous media with a one-dimensional diffusion wave approximation of the de Saint Venant equations for surface water dynamics [5]. Catchment hydrology (CATHY) is considered as an effective tool for the estimation of soil dynamic behaviours comparing to field observations such as volumetric water content (VWC), soil water pressure head (ψ) and groundwater table (h).

1.2 PROBLEM STATEMENT

Characterizing the soil hydraulic properties of an agricultural plot in South of Venice Lagoon presents significant challenges due to the presence of heterogeneous soil properties, including paleochannels as well as the water table that remains constant due to an artificial drainage system connected to the Brenta and Po rivers. The simulation of soil-water dynamics are applied through CATHY model. In this simulation, it does not consider specific storage as its value remains constant over time and for each layer. Initially, the CATHY model utilizes the value of parameters estimated by the laboratory for the simulation. The ultimate goal is to understand the salinization affecting the study area and this analysis is a first and necessary step towards the subsequent modeling of salt transport, which needs a well calibrated model that takes into account the interactions between surface and subsurface.

However, manual calibration of the most individual model parameters often comes with limitations. Due to the relatively broad range of parameters value estimated by the lab, then it is advisable to narrow down its range. To achieve this, the soil type is determined using multipoint triangle method from U.S Department of Agriculture (USDA), incorporating lab data on soil percentages. Subsequently, hydraulic properties are estimated through Rosetta calculator purposed to have smaller value ranges. Then, reference for Van Genuchten parameters are sourced from Carsel and Parrish paper [10], facilitating the simulation is able to be finished in shorter time. As the final step, SCEUA optimization procedure is performed on paleochannel and sand horizontal conductivities, vertical anisotropy and porosity.

1.3 OBJECTIVES

The research aims to achieve the following objectives:

1. Develop an integrated approach that combines field data, laboratory data, Rosetta and USDA estimation, and numerical modeling.
2. Conduct preliminary manual model calibration.
3. Perform automatic parameter optimization calibration.
4. Conduct a prior analysis of water table dynamics of the case study area.
5. Conduct a prior analysis of water content dynamics of the case study area.
6. Conduct a prior analysis of water pressure head dynamics of the case study area.

Although an attempt has been made by Botto (2023) to numerically simulate the behaviour of water-soil dynamics, this attempt only involved simplifications focusing on hydraulic parameters, without taking into account Van Genuchten parameters. Additionally, their study suggested that surface dynamics had limited influence and did not significantly improve the overall model performance. Therefore, the primary aim of this study is to incorporate both hydraulic and Van Genuchten parameters in the simulation and to optimize each parameter to achieve the best model performance.

CHAPTER 2

2. CASE STUDY and METHODOLOGY

2.1 CASE STUDY

2.1.1 Site description

The research site area is a 21-ha agricultural field situated at Ca' Bianca, Chioggia, North-East of Italy positioned at coordinates (45°10′57″ N and 12°13′55″ E), along the southern edge of the Venice Lagoon (Figure 2). It is adjacent to the Morto channel, Bacchiglione, and Brenta rivers, which discharge into the Adriatic sea approximately 7 kilometres to the west. This area lies below the average sea level, ranging from -1.5 to -3.3 meters above mean sea level (msl) and the underwent reclamation for agricultural use between 1892 and 1967.

The region faces challenges from saltwater intrusion, extending around 20 meters below the surface. The first confined fresh-water aquifer lays at 45–50 m below msl [39]. Precisely, the region is marked by an intricate blend of natural and man-made hydrological features, highlighted by an elaborate network of ditches within the inland area of the domain (Figure 2). An integrated approach has been developed where laboratory activity, field activity and numerical modelling are merged. Hence, it is crucial to accurately estimate the dynamics of the water table, water content as well as the pressure head at the pilot site. These estimation are essential for replicating saltwater intrusion patterns effectively and evaluating the efficacy of mitigation measures aimed at managing freshwater resources, such as drainage systems.

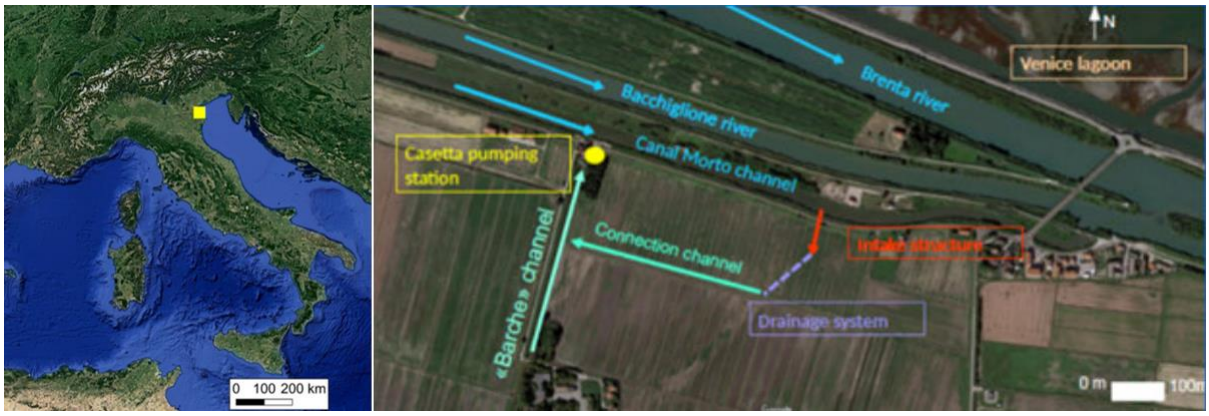

Figure 2. Map of the study area in Northern Italy depicting the site situation.

Historically, this area was characterized by swamps until it was reclaimed for agricultural activities during the aforementioned period. Due to its geographical position, the site experiences seawater encroachment and is situated below msl, with elevations varying between approximately -1 meter to -3.3 meters msl. To facilitate the farming practice the water table is maintained at a shallow depth through an extensive network of open ditches and a pumping station, which discharged excess water into the lagoon. The depth of the water table fluctuates between 0.5 to 1.8 meters below the soil surface (bss), with the minimal vertical variation, typically around 0.5 meters, throughout the year. Typically, the water table is intentionally kept shallow during the summer months to support sub-irrigation practices.

The soil is mainly silt-clay (Molli-Gleyic Cambisol) [32] with the presence of acidic peat [33] deposits formed from the reedbeds and swamps in place before the reclamation and sandy paleochannels crossing the field derived from past fluvial ridges and coastal strips. And the dataset used in the present test was collected during the year 2019.

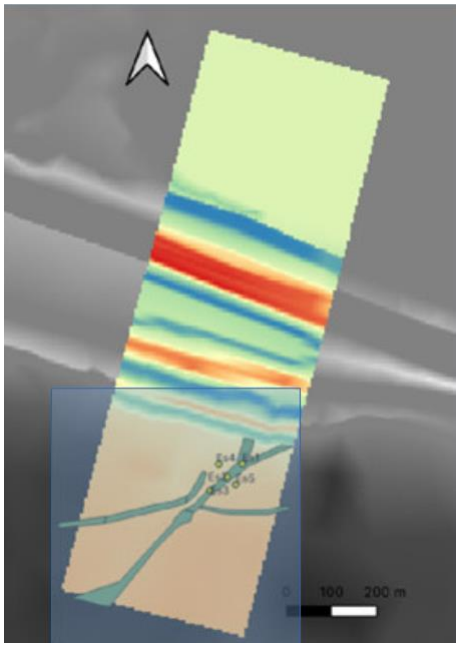

Figure 3. The dtm plot of the domain along with the boreholes position.

Figure 3 depicts the domain's digital terrain model (DTM), showcasing the sandy paleochannel's location along with the five borehole positions where measurements were taken prior to the installation of the piping drain. The first three boreholes were placed along the paleochannels, and the other two boreholes were located outside of the paleochannels. The study area, represented in blue, has been accurately modelled using CATHY software, with particular attention given to replicating the irrigation system's network of ditches. Boundary conditions are established based on data from Trezze and Casetta levels,

characterized by varying time resolutions (daily or hourly), which undergo preprocessing. The geological composition comprises three distinct units: backfill, sand, and highly permeable paleo-channels. The flow integrates data from five boreholes, with variable measurements taken daily across different depths. And the utilized software for modeling is CATHY.

2.1.2 DATA

The undisturbed soil samples were collected from four depth intervals (8-13 cm, 28-33 cm, 48-53 cm, and 68-73 cm) and analysed for bulk density and porosity. Table 1 presents the results for bulk density and porosity for each layer. Given that the modeling is centred on the conditions in 2019, bulk density values range from 0.20 to 1.56. Saturated porosity data range from 0.23 to 0.81.

Table 1. Laboratory result (2019, 2021) for bulk density and porosity.

Station	Soil depth cm	bulk density 2021 g/cm3	bulk density 2019 g/cm3
1	8-13	1.09	1.01
1	28-33	1.13	1.03
1	48-53	0.96	0.74
1	68-73	1.35	
2	8-13	1.30	1.17
2	28-33	1.23	1.19
2	48-53	1.53	1.54
2	68-73	1.50	
3	8-13	1.12	1.03
3	28-33	1.08	1.11
3	48-53	1.50	1.56
3	68-73	1.35	
4	8-13	1.17	0.90
4	28-33	1.18	1.12
4	48-53	0.36	0.25
4	68-73	1.05	
5	8-13	1.03	0.98
5	28-33	0.94	0.94
5	48-53	0.23	0.20
5	68-73	0.21	

Another laboratory activity involved estimating the Van Genuchten-Mualem (VGM) parameters including porosity, residual porosity, alpha (α), n, and the saturated hydraulic conductivity. Table 2 provides the result for these VGM parameters. Samples were also collected at four depths (0-20 cm, 20-40 cm, 40-60 cm, and 60-80 cm). Overall, the residual porosity θ_r value ranges from 0.0010 to 0.1629, the porosity θ_s ranges from 0.2376 to 0.7692, α ranges from 0.0019 to 0.0323, n ranges from 1.1001 to 2.1005 and saturated hydraulic conductivity ranges from 14 to 2605 cm/day.

Table 2. The laboratory result for Van Genuchten Mualem (VGM) parameters 2019.

point_ID	Reference Depth cm	θr	θs	α	n	Ks cm/day
S1	0-20	0.0010	0.4080	0.0206	1.1020	14
S1	20-40	0.0010	0.3949	0.0034	1.1517	15
S1	40-60	0.0010	0.4413	0.0023	1.3260	1684
S1	60-80					
S2	0-20	0.0010	0.3306	0.0115	1.1300	410
S2	20-40	0.0010	0.3307	0.0151	1.1268	22
S2	40-60	0.0010	0.2658	0.0088	1.1892	38
S2	60-80					
S3	0-20	0.0010	0.3491	0.0083	1.1318	601
S3	20-40	0.1629	0.3535	0.0022	1.5031	409
S3	40-60	0.0364	0.2376	0.0160	2.1005	55
S3	60-80					
S4	0-20	0.0010	0.3554	0.0072	1.1373	2605
S4	20-40	0.0010	0.3565	0.0081	1.1096	831
S4	40-60	0.0010	0.7295	0.0016	1.2242	142
S4	60-80					
S5	0-20	0.0010	0.4341	0.0323	1.1001	984
S5	20-40	0.0010	0.3864	0.0047	1.1233	97
S5	40-60	0.0010	0.7692	0.0019	1.1240	2591
S5	60-80					

Table 3. Laboratory result for soil texture 2019.

point_ID	Reference Depth cm	Sand > 50.000 µm	Silt 2-50 µm	Clay < 2.000 µm
S1	0-20	26.69	59.18	14.12
S1	20-40	30.83	53.05	16.12
S1	40-60	55.90	35.65	8.45
S1	60-80	52.52	35.64	11.84
S2	0-20	27.39	55.60	17.01
S2	20-40	34.81	49.93	15.26
S2	40-60	60.35	28.80	10.85
S2	60-80	79.51	13.51	6.98
S3	0-20	31.12	52.45	16.43
S3	20-40	35.20	49.43	15.37
S3	40-60	67.46	23.47	9.07
S3	60-80	86.92	7.99	5.09
S4	0-20	21.35	58.99	19.66
S4	20-40	21.16	59.99	18.84
S4	40-60	53.64	37.23	9.13
S4	60-80	49.71	37.63	12.66
S5	0-20	28.45	53.94	17.62
S5	20-40	31.09	52.56	16.35
S5	40-60	71.39	22.62	5.99
S5	60-80	72.79	20.97	6.25

2.2 METHODOLOGY

The subsection provides the methodology related to hydrological modeling of an agricultural plot South of Venice Lagoon affected by salinization.

2.2.1 Data validation

The data from laboratory results are undergo validation using two other methods: Rosetta model and the multipoint triangle method. These methods aid in defining the soil type and the estimation of parameter value for each layer. The Rosetta model and the multipoint triangle method are freely available tools provided by the U.S. Department of Agriculture. They utilize laboratory data of soil percentages (as shown in Table 3) as input to generate estimations of hydraulic parameters and the VGM parameters.

Rosetta provides five Pedotransfer functions for predicting hydraulic properties either limited or more comprehensive input datasets. This hierarchical approach is highly practical as it allows for the optimal utilization of available data. The models rely on various input parameters, including:

- Soil textural classes
- Sand, silt and clay percentages
- Sand, silt and clay percentages and bulk density
- Sand, silt and clay percentages, bulk density and a water retention point at 330 cm (33 kPa)
- Sand, silt and clay percentages, bulk density and water retention point at 330 and 15000 cm (33 and 1500 kPa)

The first model utilizes a lookup table containing class average hydraulic parameters corresponding to each USDA soil texture class (Table 4). The remaining four models employ neural network analysis, offering more accurate predictions when a broader range on input data variable is available. In addition, Rosetta model is also enabling the estimation of unsaturated hydraulic conductivity parameters from fitted Van Genuchten [21] retention parameters. Hydraulic functions used by Rosetta are elaborated in the Eq. 3 and Eq. 4.

Table 4. USDA soil texture class

Texture Class	N	θr cm3/cm3		θs cm3/cm3		log(α) log(1/cm)		log(n) log10		Ks log(cm/day)		Ko log(cm/day)		L	
Clay	84	0.098	(0.107)	0.459	(0.079)	-1.825	(0.68)	0.098	(0.07)	1.169	(0.92)	0.472	(0.26)	-1.561	(1.39)
C loam	140	0.079	(0.076)	0.442	(0.079)	-1.801	(0.69)	0.151	(0.12)	0.913	(1.09)	0.699	(0.23)	-0.763	(0.90)
Loam	242	0.061	(0.073)	0.399	(0.098)	-1.954	(0.73)	0.168	(0.13)	1.081	(0.92)	0.568	(0.21)	-0.371	(0.84)
L Sand	201	0.049	(0.042)	0.390	(0.070)	-1.459	(0.47)	0.242	(0.16)	2.022	(0.64)	1.386	(0.24)	-0.874	(0.59)
Sand	308	0.053	(0.029)	0.375	(0.055)	-1.453	(0.25)	0.502	(0.18)	2.808	(0.59)	1.389	(0.24)	-0.930	(0.49)
S Clay	11	0.117	(0.114)	0.385	(0.046)	-1.476	(0.57)	0.082	(0.06)	1.055	(0.89)	0.637	(0.34)	-3.665	(1.80)
S C L	87	0.063	(0.078)	0.384	(0.061)	-1.676	(0.71)	0.124	(0.12)	1.120	(0.85)	0.841	(0.24)	-1.280	(0.99)
S loam	476	0.039	(0.054)	0.387	(0.085)	-1.574	(0.56)	0.161	(0.11)	1.583	(0.66)	1.190	(0.21)	-0.861	(0.73)
Silt	6	0.050	(0.041)	0.489	(0.078)	-2.182	(0.30)	0.225	(0.13)	1.641	(0.27)	0.524	(0.32)	0.624	(1.57)
Si Clay	28	0.111	(0.119)	0.481	(0.080)	-1.790	(0.64)	0.121	(0.10)	0.983	(0.57)	0.501	(0.27)	-1.287	(1.23)
Si C L	172	0.090	(0.082)	0.482	(0.086)	-2.076	(0.59)	0.182	(0.13)	1.046	(0.76)	0.349	(0.26)	-0.156	(1.23)
Si Loam	330	0.065	(0.073)	0.439	(0.093)	-2.296	(0.57)	0.221	(0.14)	1.261	(0.74)	0.243	(0.26)	0.365	(1.42)

The table provides class-average of seven hydraulic parameters for the twelve USDA texture classes, representing the first model in the hierarchical sequence. For parameters, θ_r, θ_s, a, n, and K_s, the values are computed by averaging across each texture class. Regarding K_o, and L, the values are derived by incorporating the class average values of θ_r, θ_s, a, and n into Model C2. It is important to note that K_o and L are based on predicted parameters and may exhibit some degree of uncertainty. The values in parentheses indicate the one standard deviation uncertainties associated with the class average values.

Through validation with Rosetta model, the predicted parameters value can be determined for the lower and upper bounds used in the CATHY model. On the other hand, the Multipoint Triangle method provides soil type classification for each layer based on the laboratory data of soil percentages. It is an application to determine soil texture based on the proportion of sand, silt, and clay in soil sample. In this method the percentages of sand, silt, and clay are plotted on a triangular graph known as a texture triangle. Each corner of the triangle represents 100% of one of the three soil components, and the lines connecting the corners represent the proportions of the components.

To use the Multipoint Triangle method, the soil percentages are plotted on the texture triangle. The point where the three lines intersect corresponds to the soil texture classification. For example, if the point falls within the region representing a combination of sand and silt, the soil texture will be classified as sandy loam.

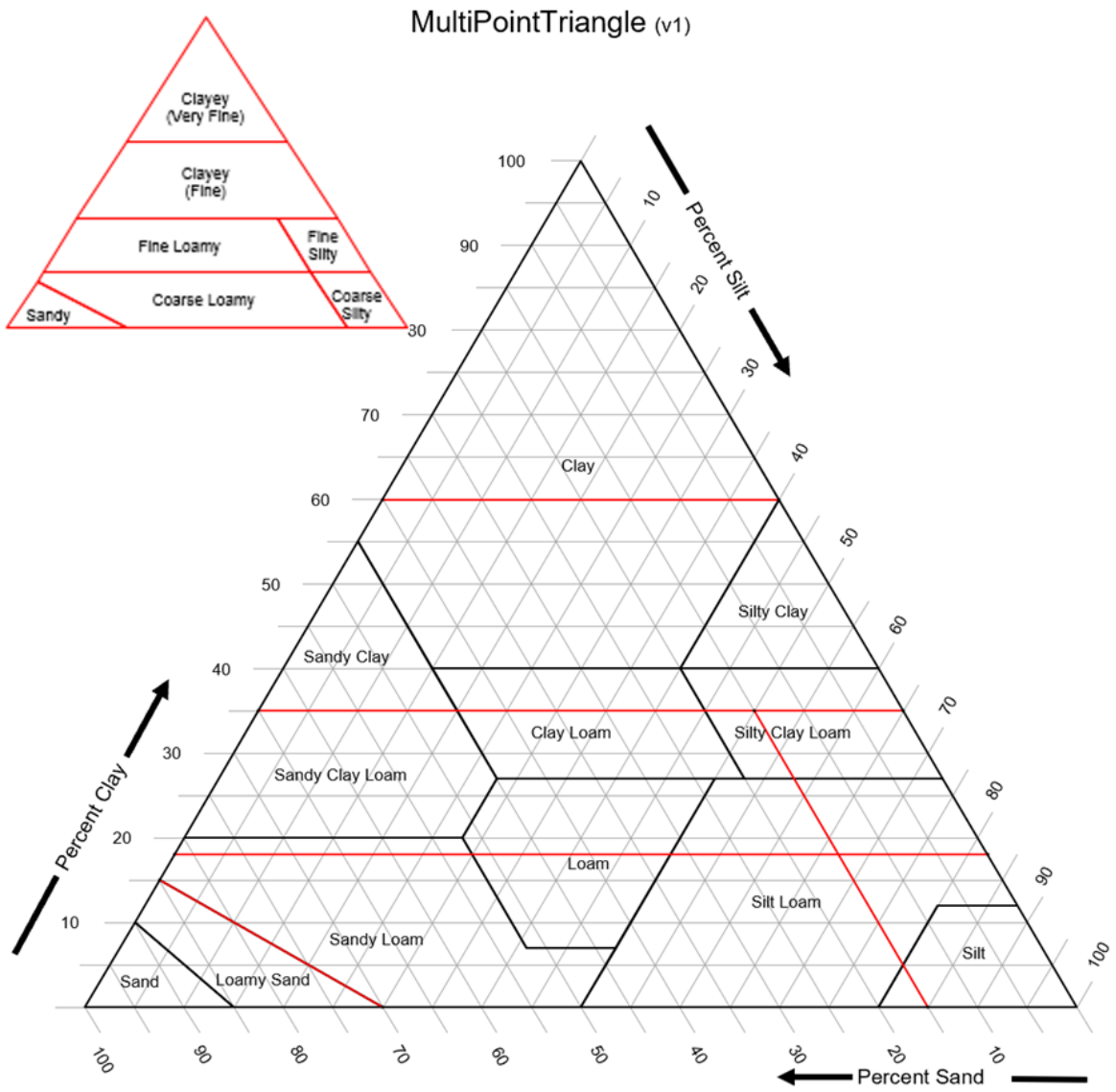

Figure 4. Multipoint triangle methods by U.S Department of Agriculture.

The preliminary simulation is started with the data input below (table 5). Given the heterogeneous nature of the site, each layer comprises two distinct types of materials. To facilitate the simulation process, a "zone.txt" file is employed, containing the setup of the material type assigned to each cell within the model domain. This approach ensures that the simulation accurately captures the spatial variability of soil composition and facilitates the representation of complex geological features present within the study area. By incorporating detailed information on material types for individual cells, the simulation accounts for the diverse soil characteristics encountered across different layers, enabling a comprehensive analysis of hydrological processes and groundwater dynamics.

Table 5. Data input for preliminary simulation

LAYER	MAT.TYPE	X-PERM	Y-PERM	Z-PERM	STORAGE	POROSITY	VGN	VGRMC	VGPSAT
1	1	4.71E-01	4.71E-01	1.57E-01	1.00E-03	3.80E-01	1.11E+00	1.00E-03	1.27E+00
1	2	1.02E-01	1.02E-01	3.40E-02	1.00E-03	3.60E-01	1.19E+00	2.79E-02	1.78E+00
2	1	4.71E-01	4.71E-01	1.57E-01	1.00E-03	3.80E-01	1.11E+00	1.00E-03	1.27E+00
2	2	1.02E-01	1.02E-01	3.40E-02	1.00E-03	3.60E-01	1.19E+00	2.79E-02	1.78E+00
3	1	4.71E-01	4.71E-01	1.57E-01	1.00E-03	3.80E-01	1.11E+00	1.00E-03	1.27E+00
3	2	1.02E-01	1.02E-01	3.40E-02	1.00E-03	3.60E-01	1.19E+00	2.79E-02	1.78E+00
4	1	5.69E-01	5.69E-01	1.90E-01	1.00E-03	7.40E-01	1.17E+00	1.00E-03	5.90E+00
4	2	2.47E-01	2.47E-01	8.22E-02	1.00E-03	3.10E-01	1.54E+00	1.28E-02	2.01E+00
5	1	5.69E-01	5.69E-01	1.90E-01	1.00E-03	7.40E-01	1.17E+00	1.00E-03	5.90E+00
5	2	1.74E+01	1.74E+01	2.64E+00	1.00E-03	4.04E-01	1.89E+00	6.70E-02	5.00E-01
6	1	4.43E-01	4.43E-01	1.93E-01	1.00E-03	5.31E-01	1.89E+00	6.70E-02	5.00E-01
6	2	1.74E+01	1.74E+01	2.64E+00	1.00E-03	4.04E-01	1.89E+00	6.70E-02	5.00E-01
7	1	4.43E-01	4.43E-01	1.93E-01	1.00E-03	5.31E-01	1.89E+00	6.70E-02	5.00E-01
7	2	1.74E+01	1.74E+01	2.64E+00	1.00E-03	4.04E-01	1.89E+00	6.70E-02	5.00E-01
8	1	4.43E-01	4.43E-01	1.93E-01	1.00E-03	5.31E-01	1.89E+00	6.70E-02	5.00E-01
8	2	1.74E+01	1.74E+01	2.64E+00	1.00E-03	4.04E-01	1.89E+00	6.70E-02	5.00E-01
9	1	4.43E-01	4.43E-01	1.93E-01	1.00E-03	5.31E-01	1.89E+00	6.70E-02	5.00E-01
9	2	4.43E-01	4.43E-01	1.93E-01	1.00E-03	5.31E-01	1.89E+00	6.70E-02	5.00E-01
10	1	4.43E-01	4.43E-01	1.93E-01	1.00E-03	5.31E-01	1.89E+00	6.70E-02	5.00E-01
10	2	4.43E-01	4.43E-01	1.93E-01	1.00E-03	5.31E-01	1.89E+00	6.70E-02	5.00E-01

2.2.2 Main equations

CATHY is an integrated process-based spatially-distributed model for surface-subsurface flow simulations [5]. This model couples a finite element solver for the Richards equation describing flow in variably saturated porous media [29], [17] and a finite difference solver for the diffusion wave equation describing surface flow propagation throughout a hillslope and stream channel network identified using terrain topography and the hydraulic geometry concept [18,19]. The model solves the three-dimensional Richards equation for flow in variably saturated porous media coupled to a one-dimensional diffusion wave approximation of the de Saint-Venant equation simulating the overland and channel routing [6]. The mathematical model is expressed by a system of two partial differential equations as

$$S_w S_s \frac{\partial \psi}{\partial t} + \theta_s \frac{\partial S_w}{\partial t} = \nabla \cdot [K_s K_{rw}(S_w)(\nabla \psi + \eta_z)] + q_{ss}(h, \psi), \quad (1)$$

$$\frac{\partial Q}{\partial t} + c_k \frac{\partial Q}{\partial s^2} = D_h \frac{\partial^2 Q}{\partial s^2} + c_k q_s(h, \psi). \quad (2)$$

Where the variables in Eq. (1) have the following meaning: $S_w = \theta/\theta_s$ is water saturation, θ and θ_s being volumetric water content and porosity (or saturated moisture content) [m^3 m^{-3}], respectively, S_s means the aquifer specific storage coefficient [m^{-1}], ψ is pressure head [m], t is time [s], ∇ is the gradient operator [m^{-1}], K_s is the saturated hydraulic conductivity tensor [m^{-1}], $K_{rw}(S_w)$ is the function of relative hydraulic conductivity, η_z is the unit vector $(0,0,1)^T$, z being the vertical coordinate directed upward, and q_{ss} as the source or sink term represents the water flux contribution from the surface to the subsurface, depending on the pressure head and the surface ponding head h [m].

In the surface flow equation (1b) a 1-D coordinate system s [L] is used to describe each element of the channel network. In this equation, Q is the discharge along the rivulet or stream channel [L^3/T], c_k is the kinematic celerity [L/T], D_h being the hydraulic diffusivity [L^2/T], and q_s is the inflow (positive) or outflow (negative) rate from the subsurface to the surface L^3/T].

The unsaturated hydraulic properties are taken into account by means of the van Genuchten functions $S_w(\psi)$ and $K_r(\psi)$ [38]:

$$S_w = S_{wr} + \frac{1-S_{wr}}{[1+(\alpha|\psi|)^n]^m}; h < 0, h \geq 0 \quad (3)$$

$$K_r = \left(\frac{S_w - S_{wr}}{1-S_{wr}}\right)^{0.5} \left\{1 - [1 - \left(\frac{S_w - S_{wr}}{1-S_{wr}}\right)^{\frac{1}{m}}]^m\right\}^2 \quad (4)$$

Where $S_{wr} = \theta_r/\phi$ is the residual water saturation, with θ_r the residual water content, α is an empirical constant [L^{-1}] related to the inverse of the entry suction, while the dimensionless shape parameters n and m are linked by the expression $m = 1 - 1/n$. These parameters are often referred to as the van Genuchten Mualem (VGM) parameters.

The sink term (q_{ss}) within the Richard's equation accounts for root water uptake, which varies with depth. Potential evapotranspiration (ET_0) is ditributed across the root depth based on a root distribution function. Actual evapotranspiration relies on soil water content and, consequently, the soil matric potential within the root zone. When soil is dry, vegetation may undergo water stress, leading to reduced transpiration to mitigate water loss. Conversely, in nearly saturated conditions, low oxygen availability to roots can also decrease transpiration rates. We modeled the effect of low and high soil moisture on root water uptake by multiplying the potential root water uptake by a reduction function, α_{rw} [15]. The reduction function, often referred as the Feddes function, becomes zero at pressure heads higher or equal to $\psi 1$, indicative of saturation when oxygen stress inhibits root water uptake. As ψ decreases, the parameter α_{rw} is assumed to linearly increase up to 1 at the anaerobiosis point $\psi 2$. Below $\psi 3$, associated with incipient water stress, transpiration is assumed to linearly decrease, reaching zero at the wilting point $\psi 4$. Between $\psi 2$ and $\psi 3$, the soil experiences well-watered conditions, allowing roots to uptake water at their potential rate (i.e., $\alpha_{rw} = 1$).

2.2.3 SCE-UA Optimization

The SCE-UA (Shuffled Complex Evolution-University of Arizona) method is a derivative-free, stochastic optimization algorithm that is widely used for solving complex optimization problems. This method is specifically designed to deal with the peculiarities encountered in conceptual watershed model calibration.

It was developed by Duan [12] at the University of Arizona. This method embodies desirable following properties: (1) global convergence in the presence of multiple regions of attraction; (2) ability to avoid being trapped by small pits and bumps on the objective function surface; (3) robustness in the presence of differing parameter sensitiveness and parameter interdependence; (4) non-reliance on the availability of an explicit expression for the objective function or the derivatives; (5) capability of handling high-parameter dimensionality.

The method is based on the synthesis of four concepts:

(1) combination of the deterministic and probabilistic approaches;

(2) systematic evolution of a 'complex' of points spanning the parameter space, in the direction of global improvement;

(3) competitive evolution;

(4) complex shuffling.

The first three concepts are drawn from existing approaches that have been proven successful in the past [26], [30], [32], [22], [40], and the last concept was recently introduced [12],[13], [35]. The elements synthesis makes the SCE-UA method effective and robust, and also flexible and efficient. Below the general description of the steps of the SCE-UA method (a more detailed presentation of the theory underlying the SCE-UA algorithm has been given by Duan et. al. [12], [13]:

1. Generate sample: sample *s* points randomly in the feasible parameter space and compute the criterion value at each point. In the absence of prior information on the approximate location of the global optimum, use a uniform probability distribution to generate a sample.

2. Rank points: sort the *s* points in order of increasing criterion value so that the first point represents the smallest criterion value and the last point represents the largest criterion value (assuming that the goal is to minimize the criterion value).

3. Partition into complexes: partition the s points into p complexes, each containing m points. The complexes are partitioned such that the first compiles contains every $p(k - 1) + 1$ ranked point, the second complex contains every $p(k - 1) + 2$ ranked point, and so on, where $k = 1,2,\ldots..,\ m$.

4. Evolve each complex: evolve each complex according to the competitive complex evolution (CEE) algorithm.

5. Shuffle complexes: combine the points in the evolved complexes into a single sample population; sort the sample population in order of increasing criterion value; shuffle (i.e. re-partition) the sample population into p complexes according to the procedure specified in step 3.

6. Check convergence: if any of the pre-specified convergence criteria are satisfied, stop; otherwise, continue.

7. Check the reduction in the number of complexes: if the minimum number of complexes required in the population, $p_{\min}$, is less than p, remove the complex with the lowest ranked points; set $p = p - 1$ and $s = pm$; return to step 4. If $p_{\min} = p$, return to step 4.

The initial random sampling of the parameter space provides the potential for locating the global optimum without being biased by pre-specified starting points. The partition of the population into several communities facilitates a freer and more extensive exploration of the feasible space in different directions, thereby allowing for the possibility that the problem has more than one region of attraction. The shuffling of communities enhances the survivability by a sharing of the information (about the search space) gained independently by each community.

As already mentioned in the step 4, the CCE algorithm is one key component of the SCE-UA. Based on the Nelder and Mead [25] Simplex downhill search scheme, this algorithm is presented simply as follow:

1. Construct a subcomplex by randomly selecting q points from the complex (community) according to a trapezoidal probability distribution. The probability distribution is specified such that the best point (i.e. the point with the best function value) has the highest chance of being chosen to form the subcomplex, and the worst point has the least chance.

2. Identity the worst point of the subcomplex and compute the centroid of the subcomplex without including the worst point.

3. Attempt a reflection step by reflecting the worst point through the centroid. If the newly generated point is within the feasible space, go to step 4, otherwise, randomly generate a point within the feasible space and go to step 6.

4. If the newly generated point is better than the worst point, replace the worst point by the new point. Go to step 7. Otherwise, go to step 5.

5. Attempt a contraction step by computing a point halfway between the centroid and the worst point. If the contraction point is better than the worst point, replace the worst point by the contraction point and go to step 7. Otherwise, go to step 6.

6. Randomly generate a point within the feasible space. Replace the worst point by the randomly generated point.

7. Repeat step 2- 6 α times, where $\alpha \geq 1$ is the number of consecutive offspring generated by the same subcomplex.

8. Repeat step 1- 7 β times, where $\beta \geq 1$ is the number of evolution steps taken by each complex before complexes are shuffled.

The CCE algorithm adopts a framework reminiscent of genetic optimization methods, where each point within a complex is akin to a potential 'parent' capable of contributing to the production of offspring. Unlike typical genetic algorithms, CCE allows subcomplexes with more than two members, enabling a broader exploration of the parameter space. It prioritizes stronger points to create healthier offspring, speeding up the search for promising regions. The algorithm predominantly relies on the Nelder-Mead Simplex downhill search scheme for generating offspring, known for its resilience to non-smooth response surfaces. Occasionally, random offspring are introduced to maintain robustness, akin to mutations in biological evolution. Every member of the population is given an opportunity to contribute before potentially being replaced. This approach ensures that no valuable information contained within the sample population is overlooked, ensuring comprehensive exploration and exploitation of the search space.

2.2.4 Model performance evaluation

The calibration of hydrological models should be approached as a multi-objective problem [28]. Within a multiple-criteria framework, the MSE and NSE criteria continue to be commonly used, because they can be computed separately for (1) different types of observations (e.g. runoff and snow observations; [2]), (2) different locations (e.g. runoff at multiple gauges; [21]), or (3) different subsets of the same observation (e.g. rising and falling limb of the hydrograph; [3]).

The Kling-Gupta Efficiency (KGE) serves as a robust statistical tool for evaluating effectiveness of hydrological models, particularly in replicating streamflow or other hydrological variables. Gupta [20] said that a peculiar feature of the Nash Sutcliffe Efficiency criterion is the problematic interplay between α (the quantity) and r (linear correlation coefficient), which is likely to result in an underestimation of the variability in the flows. KGE provides a comprehensive assessment by considering three key aspects: correlation, bias, and variability. By using the ration of the means of the simulated and observed flows (β), it makes sense to enable a better hydrological interpretation of the bias component for the further analysis – as opposed to using β_n, hence all three of the components now have their ideal values at unity. The KGE is computed with the formula as follow:

$$KGE = 1 - \sqrt{(r-1)^2 + (\alpha-1)^2 + (\beta-1)^2} \quad (5)$$

Where:

- r is the Pearson correlation coefficient between observed and simulated values,
- α is a term representing the predictions errors variability; the ratio of the standard deviation of simulated observed values,
- β is a bias term; the ration of the mean simulated to mean observed values.

The terms α and β are explained as follows:

$$\beta = \frac{\mu_s}{\mu_o} \quad (6)$$

where:

- μ_s is the mean of the simulated time series,
- μ_o is the mean of the observed time series.

and

$$\alpha = \frac{\sigma_s}{\sigma_o} \quad (7)$$

where:

- σ_s is the standard deviation of simulated data,
- σ_o is the standard deviation of observed time series.

The KGE combines three components into a single index, providing a comprehensive measure of model performance. It ranges from negative infinity to 1, with a perfect agreement yielding score of 1. Values closer to 0 or below indicate less accurate model performance.

2.2.5 Model setup

The modeling process begins by defining the Digital Elevation model (DEM) parameters with a resolution of 2 meters by 2 meters. Along the x-direction, the model consists of 81 cells, while along the y-direction, it comprises 82 cells, resulting in a total of 6724 cells within the catchment area. Based on bore logs collected in the field, the soil depth is uniformly assigned a values of 10 meters, leading to a total of 10 vertical discretization layers. These layers start from the surface with the thinnest mesh stratum of 0.005 meters, crucial for accurately resolving the strong non linearities, especially during the transitions from rainfall to evaporation. As the layers progress deeper, they gradually increase in thickness, reaching a maximum of 2.25 meters. Consequently, the model encompasses 73964 nodes in total and 393660 of Tetrahedra in 3-D mesh.

The model simulation spans from 21 July 2019 to 20 January 2020. Meteorological data were recorded from a weather station located 3 km from the study area by the Regional Agency for Environmental Protection, Veneto Region. The data comprises information on potential evapotranspiration, actual evapotranspiration, and precipitation. To maintain consistency, no-flow conditions are applied to both the bottom of the grid and all the lateral boundaries. Initially, the model is run using only as the subsurface model. Calibration of the model is conducted based on three field measurements: water table, pressure head and water content.

CHAPTER 3

3. RESULTS

3.1 Data Validation

The laboratory-derived results underwent rigorous validation through two complementary methodologies: the Rosetta model and the Multipoint Triangle method. These approaches were instrumental in characterizing soil types and estimating predicted parameter values for individual layers with a high degree of precision. Leveraging the Rosetta model, Pedotransfer functions were employed to predict hydraulic properties across diverse input of datasets. Through a hierarchical analysis, this model optimized the utilization of available data, considering such as soil texture classes, percentages of sand, silt, and clay, as well as bulk density and water retention points. In this simulation, the model is run by utilizing the laboratory results providing the soil percentages and the bulk density. The outcomes, meticulously presented in Table 5 as shown below:

Table 6. The comparison data validation from Rosetta model and Laboratory result 2019

point_ID	Reference Depth cm	Soil type	Ks (cm/day)	Ks (m/h)	Ks cm/day (lab)
S1 0-0.2	0-20	Silt loam	115.97	0.04832	14
S1 0.2-0.4	20-40	Silt loam	97.36	0.04057	15
S1 0.4-0.6	40-60	Sandy loam	38.00	0.01583	1684
S1 0.6-0.8	60-80	Sandy clay	26.49	0.01104	
S2 0-0.2	0-20	Silt loam	36.20	0.01508	410
S2 0.2-0.4	20-40	Loam	32.80	0.01367	22
S2 0.4-0.6	40-60	Sandy loam	26.99	0.01125	38
S2 0.6-0.8	60-80	Loamy sand	85.73	0.03572	
S3 0-0.2	0-20	Silt loam	96.17	0.04007	601
S3 0.2-0.4	20-40	Loam	70.29	0.02929	409
S3 0.4-0.6	40-60	Sandy loam	36.84	0.01535	55
S3 0.6-0.8	60-80	Loamy sand	208.46	0.08686	
S4 0-0.2	0-20	Silt loam	15.84	0.00660	2605
S4 0.2-0.4	20-40	Silt loam	16.53	0.00689	831
S4 0.4-0.6	40-60	Sandy loam	34.20	0.01425	142
S4 0.6-0.8	60-80	Loam	23.13	0.00964	
S5 0-0.2	0-20	Silt loam	17.77	0.00740	984
S5 0.2-0.4	20-40	Silt loam	19.42	0.00809	97
S5 0.4-0.6	40-60	Sandy loam	62.14	0.02589	2591
S5 0.6-0.8	60-80	Sandy loam	64.21	0.02675	

The Rosetta model was simulated by having the input from Table 1 for bulk density and Table 3 for the soil percentages. Table 5 emphasizes the value from the Rosetta model most likely having much smaller ranges than the value from laboratory result. The value saturated hydraulic conductivity value is 15.84 cm/day with the soil type of silt loam, while the highest value is only at 208.46 cm/day for loamy sand soil type. On the other hand, the laboratory data presents the lowest hydraulic conductivity value is 14 cm/day and the highest value is 2605 cm/day. Across the first three borehole, silt loam consistently exhibited higher value than sandy loam. Inversely, the fourth and the fifth borehole indicated that sandy loam has higher permeability than silt loam. For enhanced clarity, the comparison between the Rosetta analysis and laboratory analysis is presented in Figure 5.

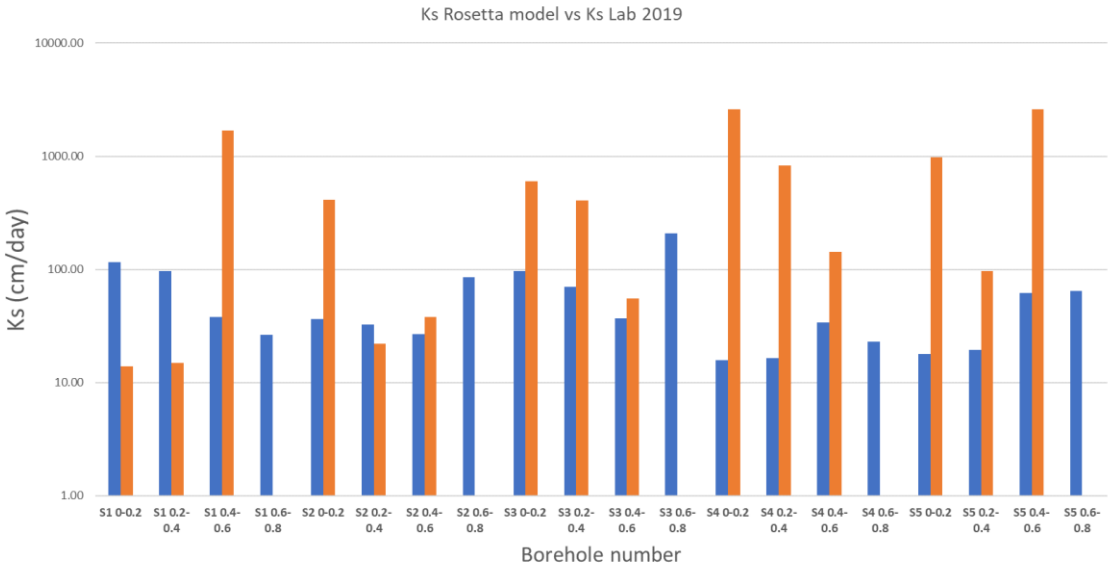

Figure 5. The plotted comparison data validation from Rosetta model and Laboratory result 2019

Table 7. Van Genuchten parameters comparison between Rosetta results and Laboratory 2019

point_ID	Reference Depth cm	Rosetta model				Laboratory 2019			
		θr	θs	n	α	θr	θs	α	n
S1 0-0.2	0-20	0.082	0.489	1.558	0.003	0.0010	0.4080	0.0206	1.1020
S1 0.2-0.4	20-40	0.085	0.485	1.523	0.004	0.0010	0.3949	0.0034	1.1517
S1 0.4-0.6	40-60	0.061	0.391	1.455	0.011	0.0010	0.4413	0.0023	1.3260
S1 0.6-0.8	60-80	0.068	0.392	1.435	0.010				
S2 0-0.2	0-20	0.105	0.482	1.393	0.007	0.0010	0.3306	0.0115	1.1300
S2 0.2-0.4	20-40	0.105	0.477	1.391	0.007	0.0010	0.3307	0.0151	1.1268
S2 0.4-0.6	40-60	0.065	0.364	1.444	0.014	0.0010	0.2658	0.0088	1.1892
S2 0.6-0.8	60-80	0.058	0.375	1.620	0.024				
S3 0-0.2	0-20	0.086	0.486	1.519	0.004	0.0010	0.3491	0.0083	1.1318
S3 0.2-0.4	20-40	0.082	0.462	1.508	0.005	0.1629	0.3535	0.0022	1.5031
S3 0.4-0.6	40-60	0.062	0.360	1.488	0.017	0.0364	0.2376	0.0160	2.1005
S3 0.6-0.8	60-80	0.055	0.370	2.007	0.028				
S4 0-0.2	0-20	0.089	0.428	1.499	0.004	0.0010	0.3554	0.0072	1.1373
S4 0.2-0.4	20-40	0.088	0.429	1.509	0.004	0.0010	0.3565	0.0081	1.1096
S4 0.4-0.6	40-60	0.062	0.392	1.456	0.010	0.0010	0.7295	0.0016	1.2242
S4 0.6-0.8	60-80	0.071	0.394	1.438	0.009				
S5 0-0.2	0-20	0.084	0.419	1.500	0.004	0.0010	0.4341	0.0323	1.1001
S5 0.2-0.4	20-40	0.081	0.416	1.503	0.004	0.0010	0.3864	0.0047	1.1233
S5 0.4-0.6	40-60	0.056	0.381	1.507	0.020	0.0010	0.7692	0.0019	1.1240
S5 0.6-0.8	60-80	0.056	0.380	1.518	0.021				

The result comparison for Van Genuchten parameters are presented on Table 6. According to the Rosetta analysis, the highest predicted porosity is 0.489, while the lowest stands at 0.36. Based on the laboratory result, it conversely presents a broader range, with the highest porosity at 0.7295 and the lowest saturated porosity at 0.2376. Figure 6 illustrates the consistency of Rosetta analysis, showcasing relatively minimal variability in saturated porosity values. In contrast, the laboratory result presents a significant gap between the lowest and the highest analysed value.

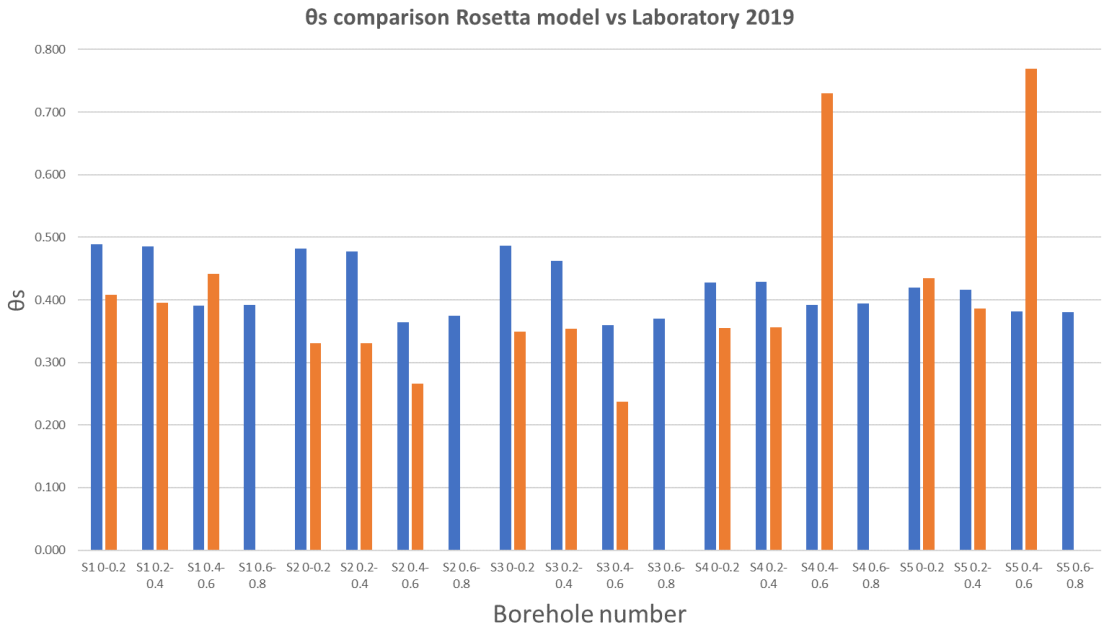

Figure 6. Saturated porosity comparison between Rosetta model and Laboratory result.

The Multipoint triangle method analysed the soil type based on input data of bulk density and the soil percentages input. As depicted in Table 5, the majority of the first two layers indicated silt loam type for across all boreholes. These results confirmed as the site is purposely for agricultural production. However, the lower two layers exhibited a diverse range of soil types, including sandy loam, loamy sand, sandy clay, and loam soil. This variability suggests the influence of underlying geological formations and hydrological processes on soil development and composition. The presence of distinct soil types in the deeper layers highlights the complex interplay factors shaping the soil profile, including variations in drainage conditions and historical land use practices as the first three boreholes are located in the previous paleochannels.

3.2 Preliminary simulation

The result of preliminary simulation is presented in the following section focusing on three key variables: water content, pressure head, and water table dynamics. Each of these parameters provides valuable insights into the hydrological behavior and groundwater dynamics within the study area. By examining variations in water content, pressure head distribution, and fluctuations in water table level, a comprehensive understanding of the hydrological processes can be attained. The results below is started with the water content in the first borehole.

3.2.1 Water content

S1 (The first boreholes)

The initial water content in the first borehole is computed by multiplying the water saturation value from the CATHY result by the porosity, taking into account the analysis for four distinct layers. Within each layer, two porosity values are considered. For the first layer, located at the depth of 0.1 m, the porosity is assigned a value of 0.36. However, it is noted that the simulation does not precisely match the observed shape of the graph depicted in Figure 7.

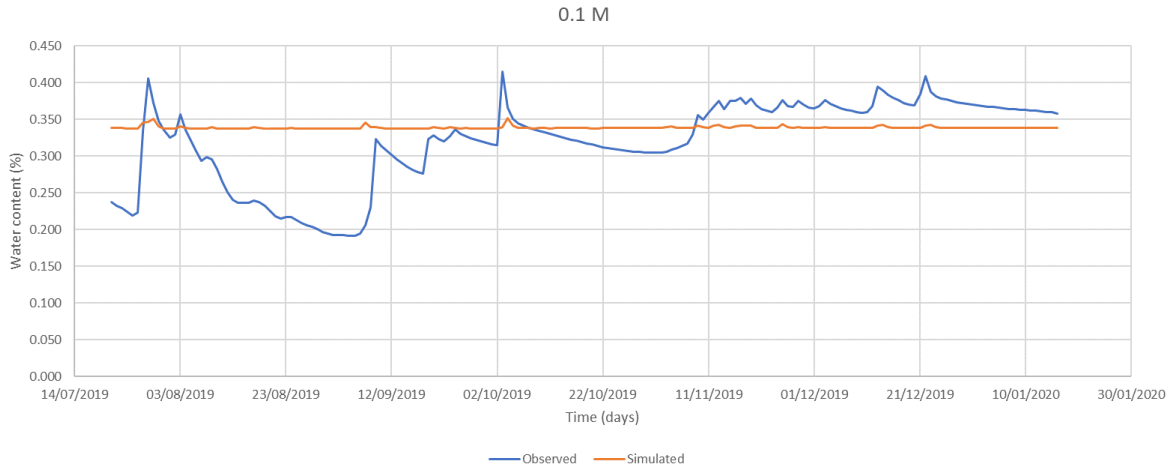

Figure 7. Water content dynamics of the first borehole

However, at the depth of 0.3 m, the simulation result indicates an underestimated value, suggesting that the actual porosity may be higher than the assigned 0.38. Conversely, the layers at depths of 0.5 m and 0.7 m demonstrate improved simulation results compared to the first layer, with porosity values of 0.36 and 0.31, respectively. Notably, the is a significant disparity

between observed data and simulated results, it is only well-matched especially at depth of 0.3 m (see Figure 7).

S2 (The second borehole)

The analysis of water content in the second borehole revealed values that closely align with the porosity for each layer. Consequently, the outcomes for all layers mirror those observed in the first borehole.

At depths of 0.1 m and 0.3 m, the graphs exhibit a similar pattern, albeit with a narrower gap observed at 0.3 m compared to 0.1 m. This suggests a higher precision in the results for the 0.3 m depth. The same trend is noted at 0.7 m with a slight difference. However, the observed data deviate in pattern at the depth of 0.5 m (see Figure 8). Consequently, the porosity values need adjustment, indicating they should be higher as the results are underestimate.

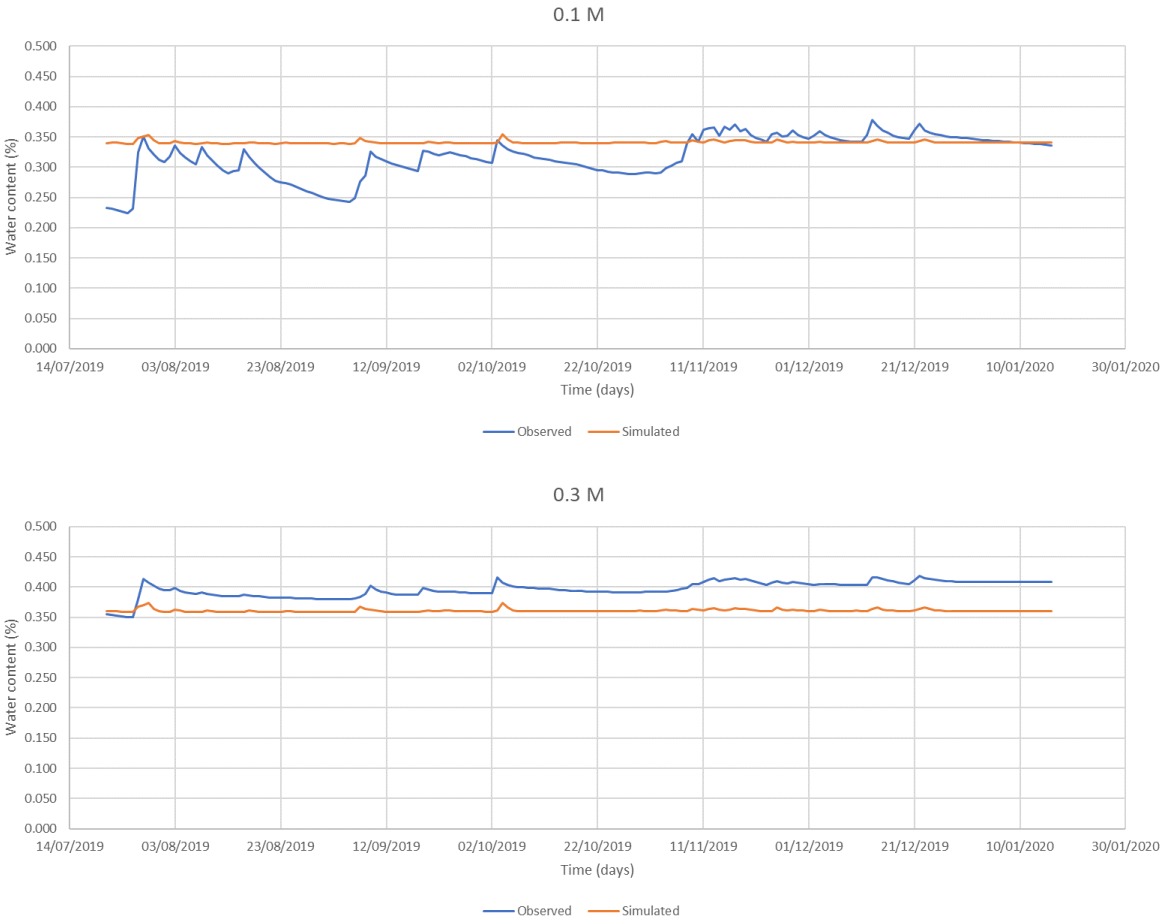

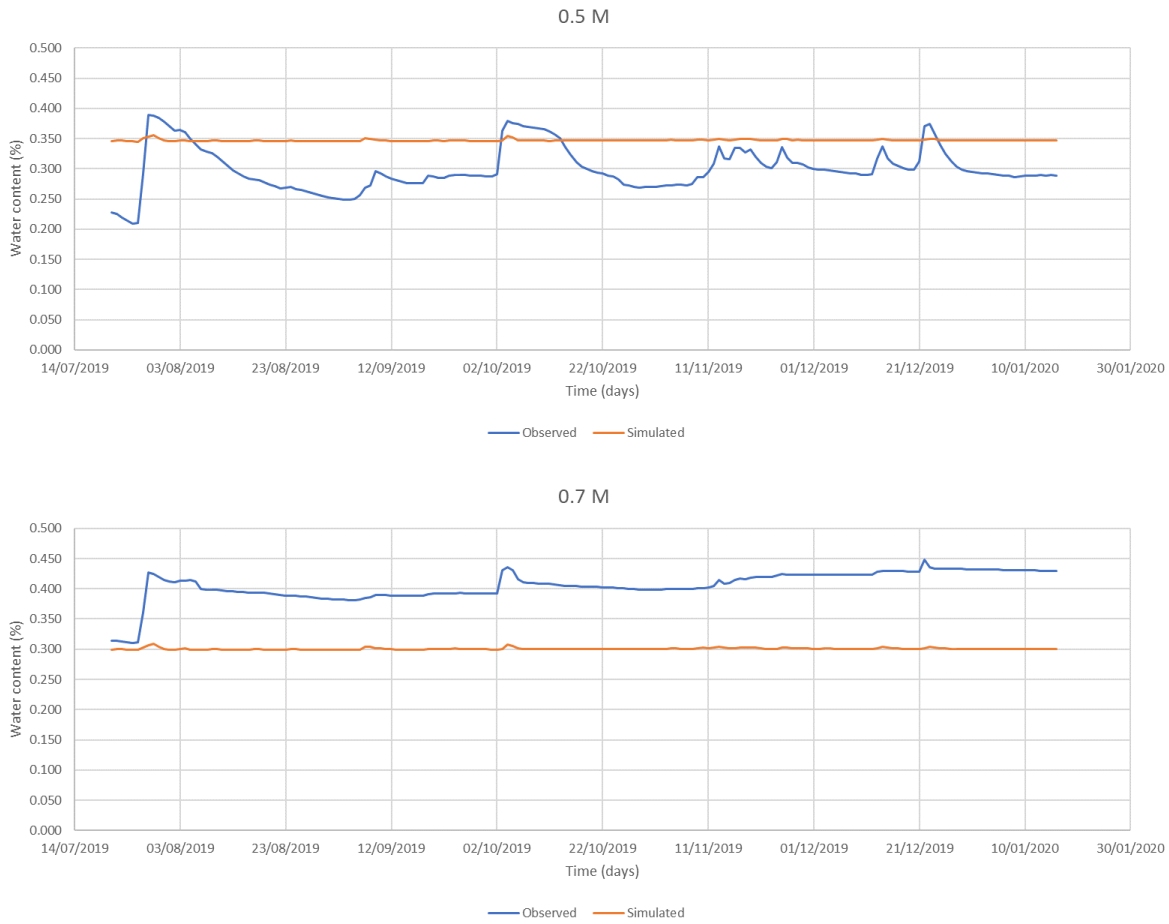

Figure 8. Water content behaviour of the second borehole

S3 (The third borehole)

The water content analysis for the third borehole falls short of accurately representing the observed data. Specifically, at depths of 0.1 m and 0.3 m, only a few segments of the graph align with the observed data. Conversely, there is a complete lack of correspondence between the simulated results and observed data at depths of 0.5 m and 0.7 m (Figure 9). Additionally, a notable observation is that all the results are overestimated, except for the depth of 0.7 m. In terms of porosity values, a distinction is noted in the second layer. Optimal accuracy is achieved with a porosity of 0.36, which is lower than that of the first and second boreholes.

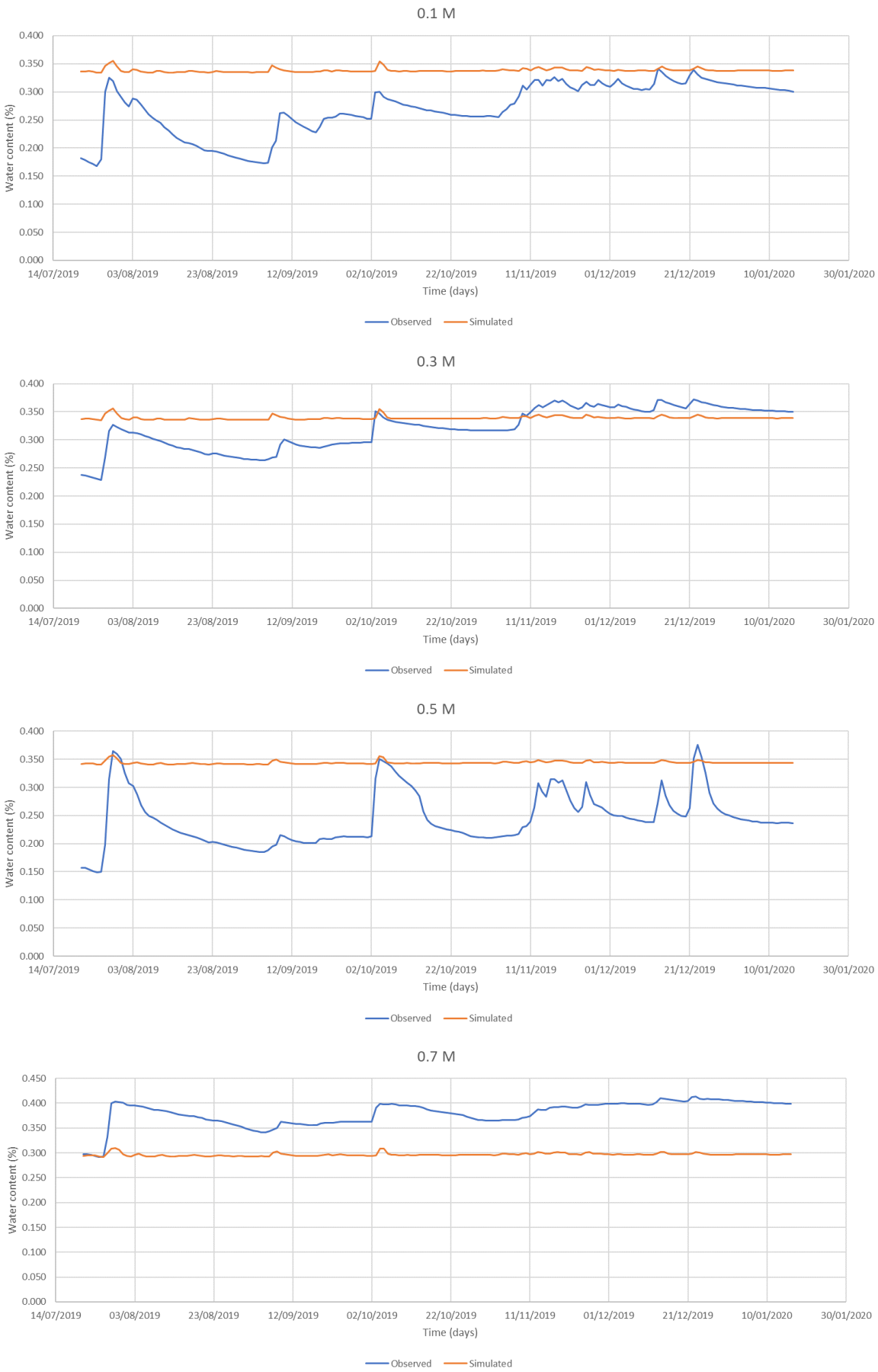

Figure 9. Water content dynamics of the third borehole

S4 (The fourth borehole)

The porosity values for each layer in the fourth borehole mirror those of the third borehole, with values of 0.36, 0.36, 0.36, and 0.31 for depths of 0.1 m, 0.3 m, 0.5 m, and 0.7 m, respectively. In Figure 10, it is evident that the results at all depths of 0.1 m; 0.3; and 0.5 m fail to accurately align with the observed data, particularly evident during the initial stages of the simulation. Although both sets of results exhibit a similar pattern at a depth of 0.5 m, there is a noticeable gap between the observed and simulated data. In contrast, the graphs for the 0.7 m depth display a better behaviour, with only minor discrepancies. Hence, the simulation could not replicate the similar water content dynamic observed the field measurements.

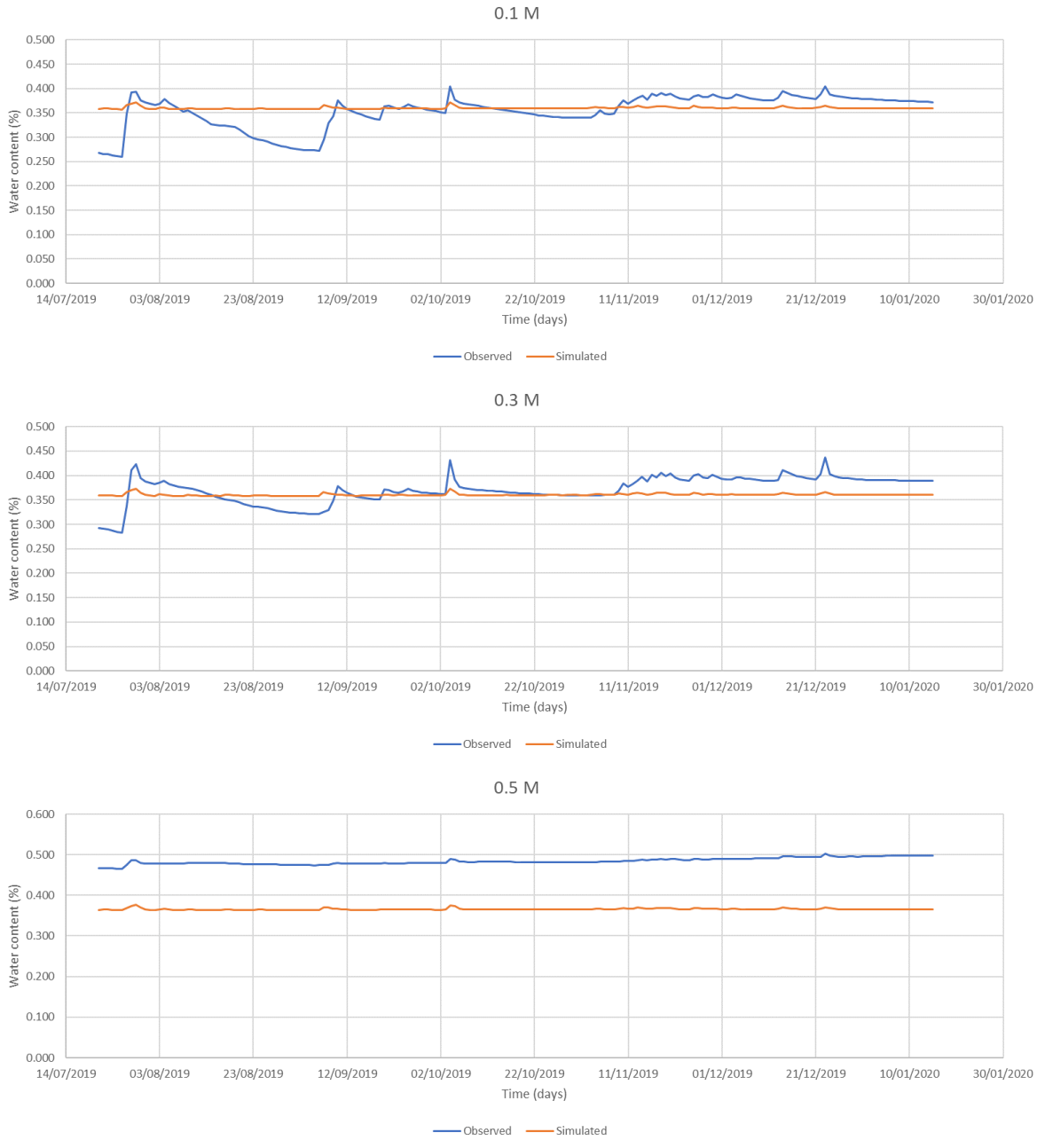

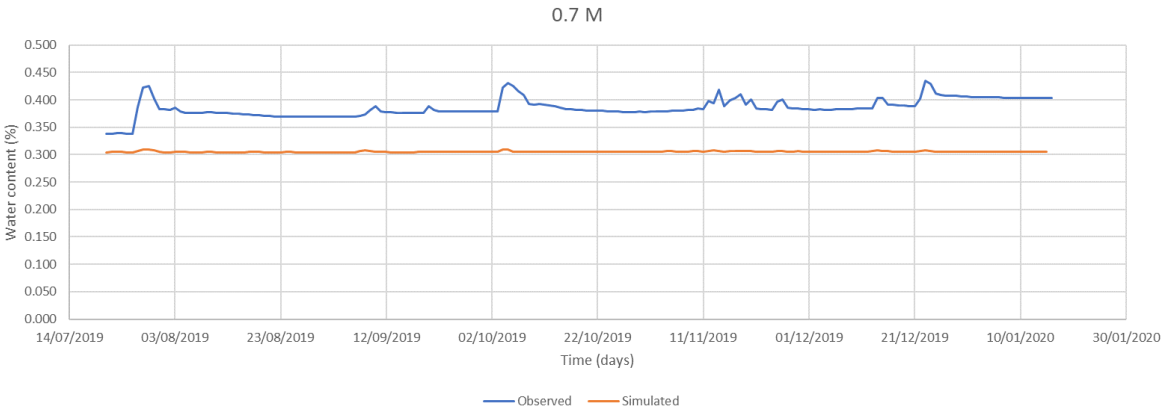

Figure 10. Water content dynamics in the fourth borehole

S5 (the fifth borehole)

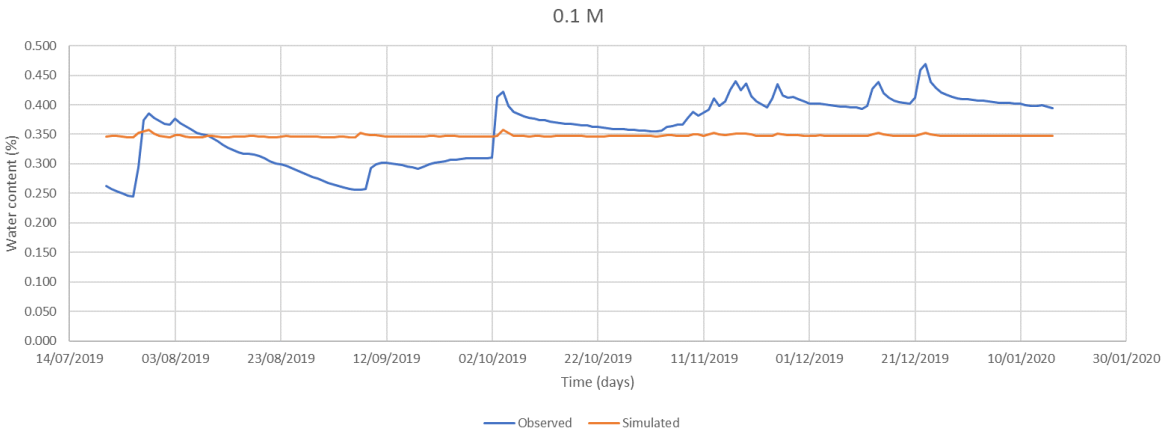

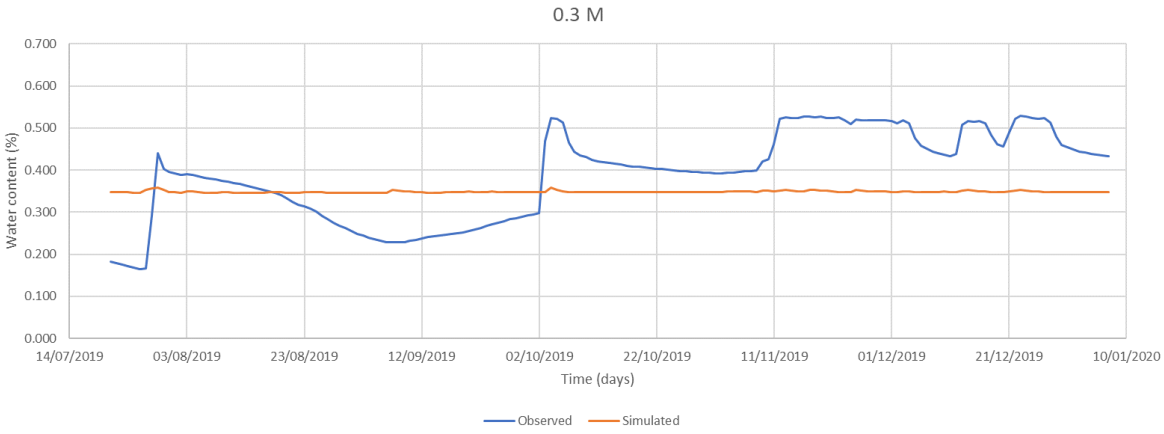

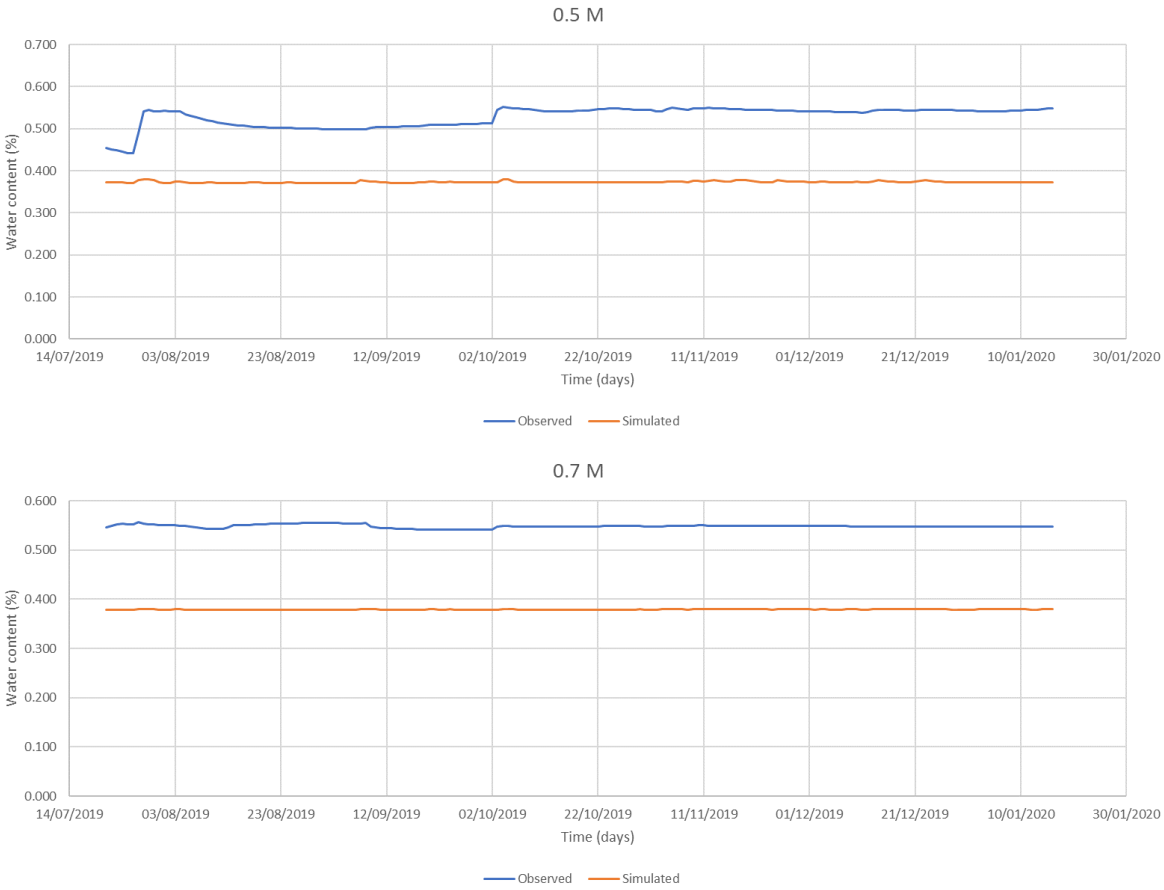

Figure 11. Water content behaviour comparison in the fifth borehole

The analysis for the fifth borehole fails to replicate similar results to the observed values, particularly at depths of 0.1 m and 0.3 m. The simulation falls short in capturing the fluctuation of water content evident in the observed data (refer to Figure 11). Conversely, the results for depths of 0.5 m and 0.7 m manage to portray a relatively similar pattern to the observed data. Despite this, there is an underestimation in the simulation for the depth of 0.5 m and 0.7 m.

3.2.2 Pressure Head

S1 (First Borehole)

The simulation for the first borehole yielded results that deviate from the observed data, specifically at depths of 0.3 m and 0.5 m (see Figure 12). A notable observation is the presence of a data absence spanning from November 27th to December 29th, 2019. During this period, the simulated results fail to match with the observed, indicating a lack of accuracy in representing the actual pressure head dynamics. It is evident that only certain sections of the graphs exhibit a close resemblance around November 21st, 2019. Additionally, the absence of data for the depth of 0.7 m, rendering a meaningful comparison between the simulated results and observed data impossible.

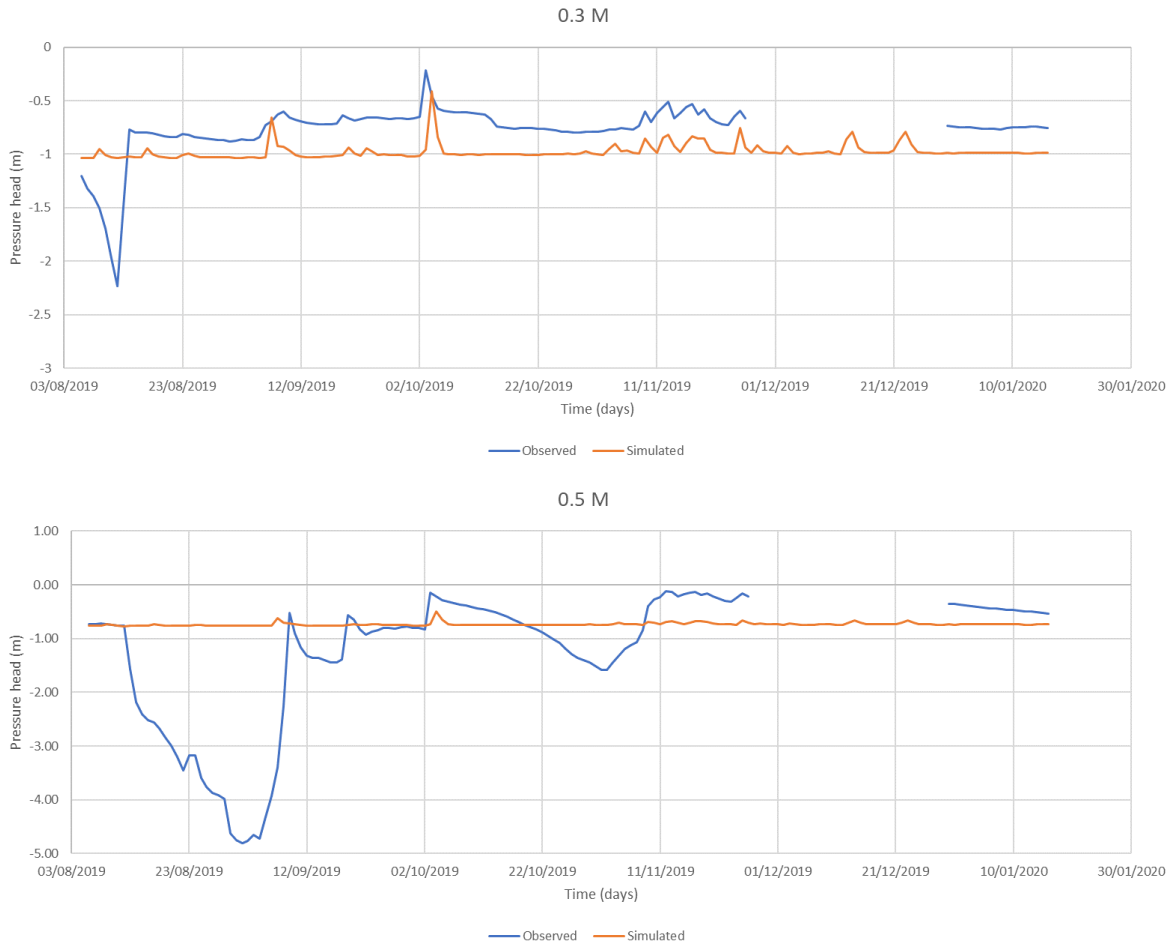

Figure 12. Pressure head dynamics in the first borehole

S2 (Second Borehole)

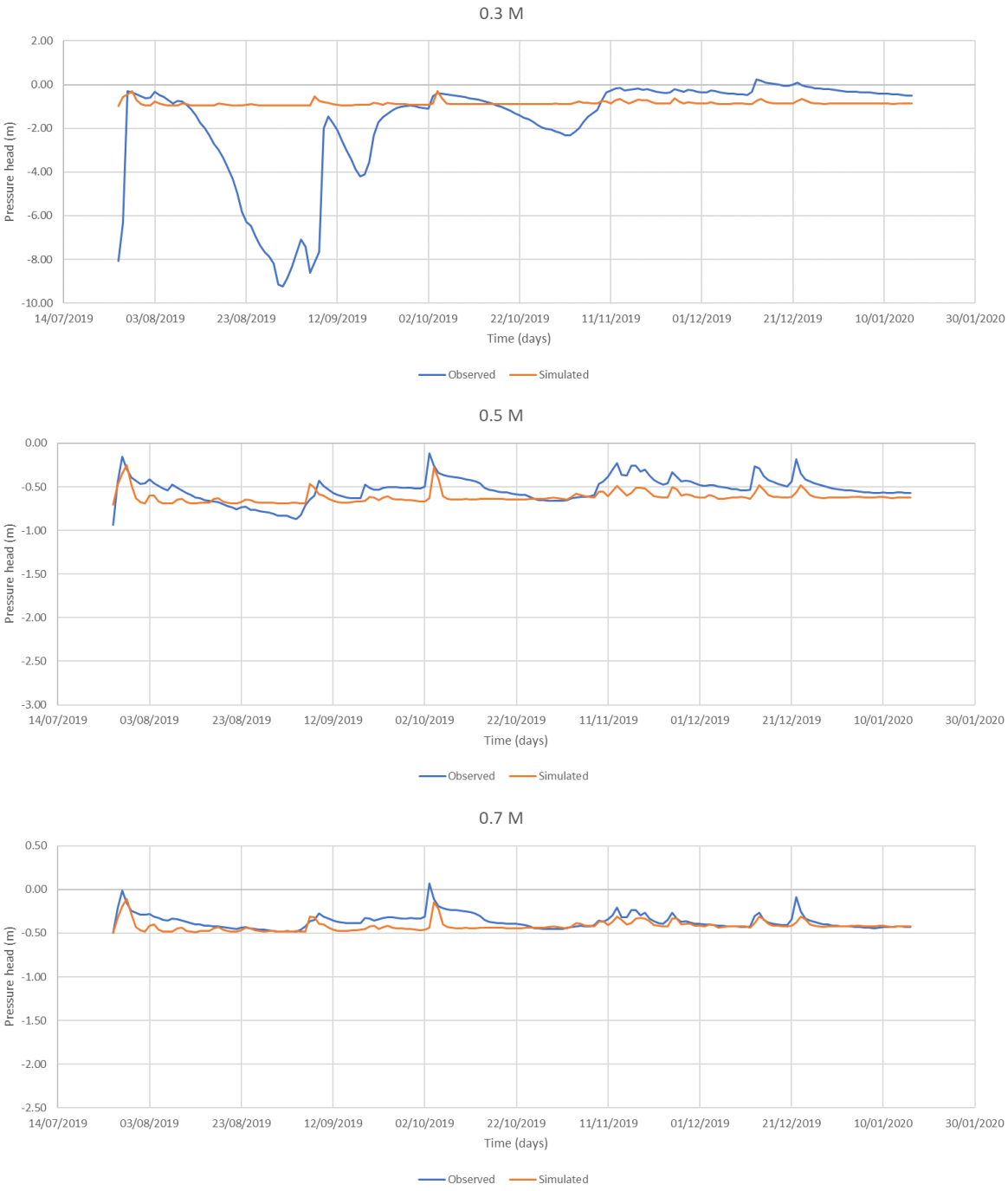

Figure 13. Pressure head dynamics comparison in the second borehole

The comparison between observed and simulated data at a depth of 0.3 m in the second borehole revealed challenges due to substantial data gaps spanning from July 26th to October 5th, 2019 (see Figure 13). These gaps in datasets significantly hindered the assessment of the simulation's performance during this period. Hence, the simulated result at a depth of 0.3 m fails representing the pressure head dynamic. Conversely, a more favourable outcome was

observed at the depths of 0.5 and 0.7 m, where the simulated results exhibited almost well-matched alignment with the observed data.

S3 (Third Borehole)

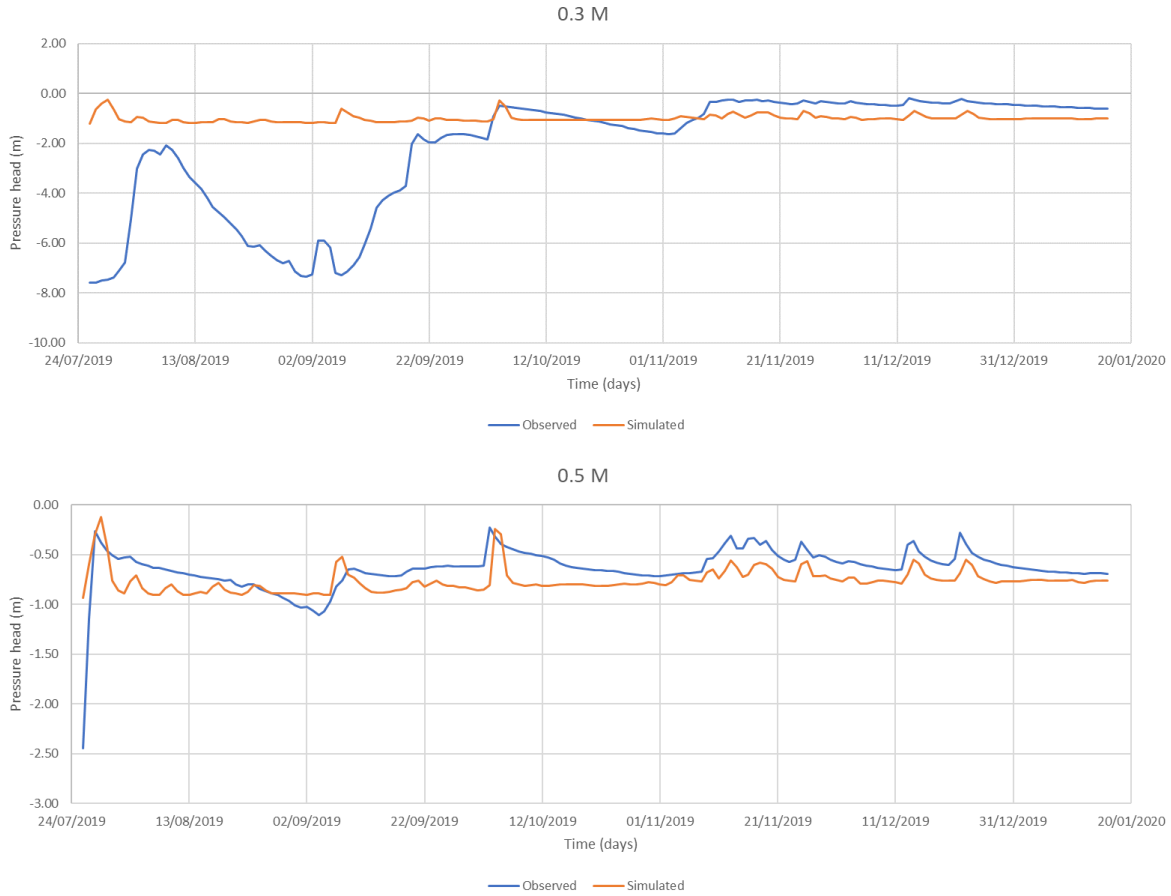

Figure 14. Water pressure head dynamic in the third borehole

The comparison between observed and simulated data at a depth of 0.3 m in the third borehole still occur challenges due to substantial data gaps persist from July 26th to October 5th, 2019 (see Figure 14). These prolonged gaps in the datasets create obstacles in assessing the accuracy of simulation during this period, as they obscure vital information regarding the dynamics of pressure head. Consequently, the graphs depicting the simulated results fail to capture the nuanced variations in pressure head. At the depth of 0.5 m, the comparison reveals narrower gap between the simulated and the observed data, indicating a relatively better alignment between the two datasets. Although some discrepancies persist, particularly during certain periods, it shows more favourable comparison than at 0.3 m depth. However, despite the reduced data gaps, the simulation still faces difficulties in fully replicating the observed trends in pressure head.

S4 (Fourth Borehole)

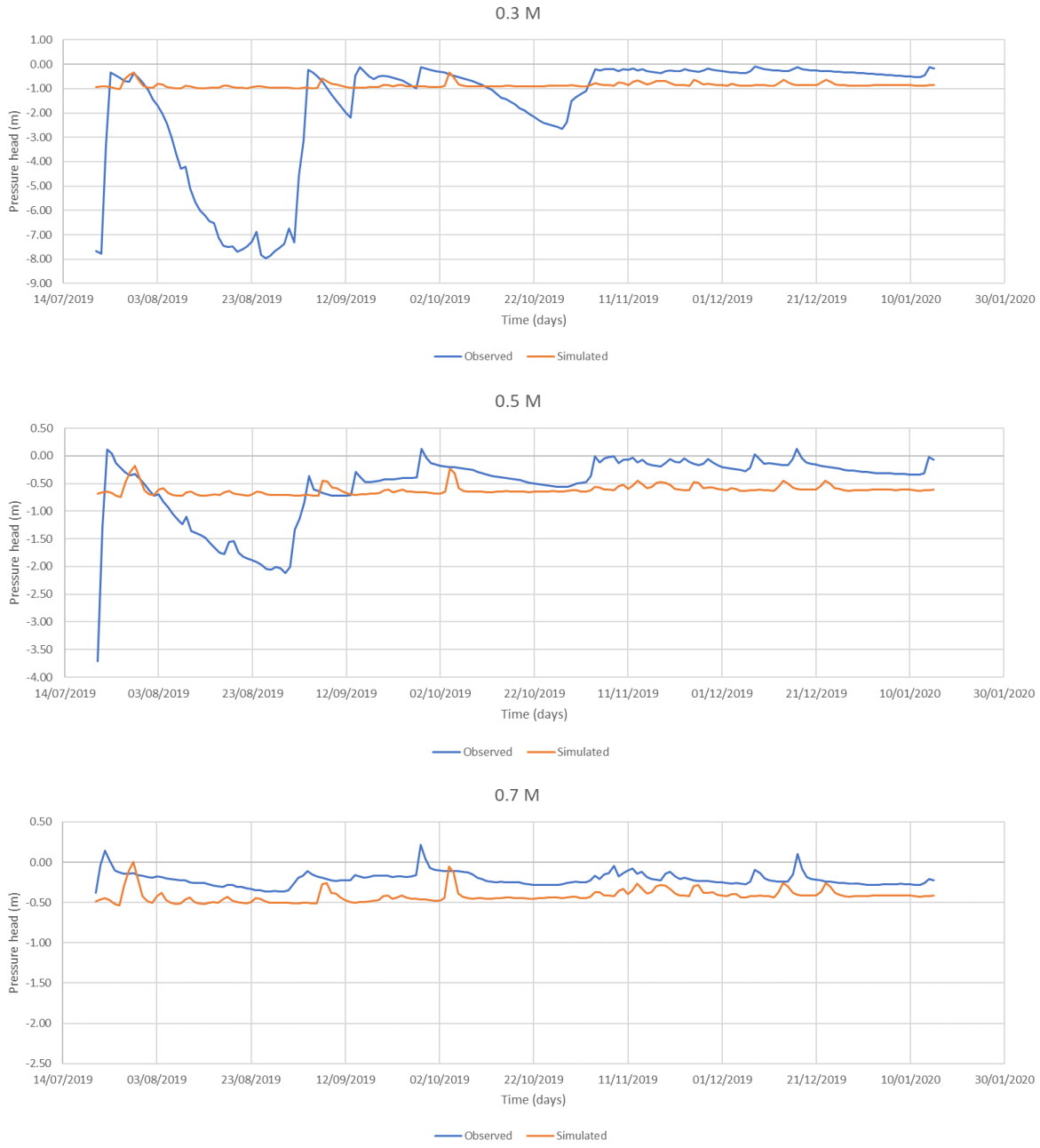

Figure 15. The pressure head dynamics in the fourth borehole

The comparison between observed and simulated data at the depths of 0.3 m and 0.5 m in the fourth borehole continues to pose challenges, primarily due to significant data gaps persist from July 26th to October 2th, 2019 (see Figure 15). These extended gaps in the datasets hinder the assessment of simulation accuracy during this period, as they obscure crucial information regarding the dynamics of pressure head. Consequently, the graphs representing the simulated results fail to capture the nuanced variations in pressure head. At the depth of 0.7 m, the comparison indicates narrower gap between the simulated and the observed data, suggesting a

relatively better alignment between the two datasets. Although some discrepancies persist, particularly during certain periods, it shows more favourable comparison than at 0.3 m and 0.5 depth.

S5 (Fifth Borehole)

The assessment of observed versus simulated data at a depth of 0.3 m in the fifth borehole encountered difficulties attributed to significant data gaps spanning from July 27th to October 4th, 2019. In contrast, a more positive portrayal emerged at the depth of 0.5 m, where the simulation closely mirrored the observed data as depicted in Figure 16. The simulation demonstrated commendable accuracy in capturing the fluctuations in pressure head. Nevertheless, it is essential to acknowledge that certain discrepancies still exist between the simulated and the observed data. However, the comparison of pressure head at the depth of 0.7 m cannot be presented due to the unavailability of observed data.

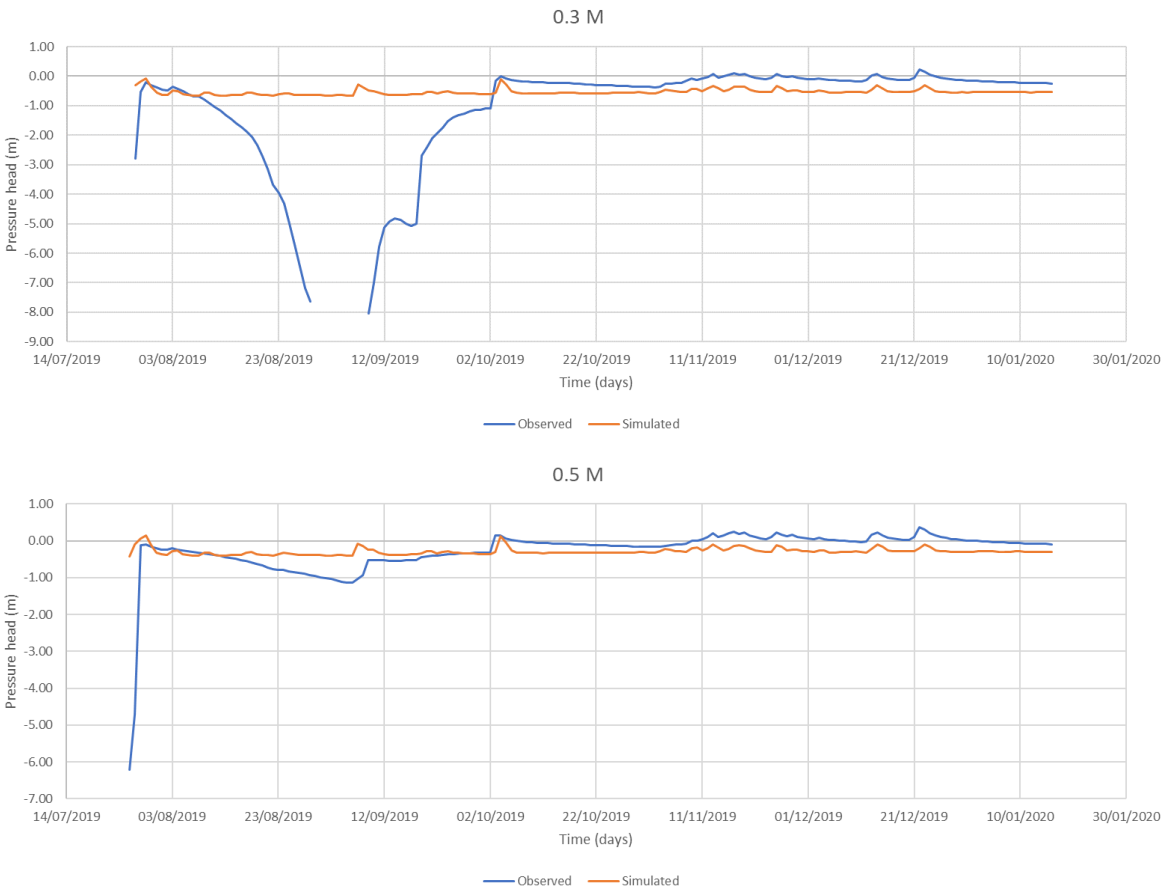

Figure 16. The pressure head dynamics in the fifth borehole

3.2.3 Water table

S1 (First Borehole)

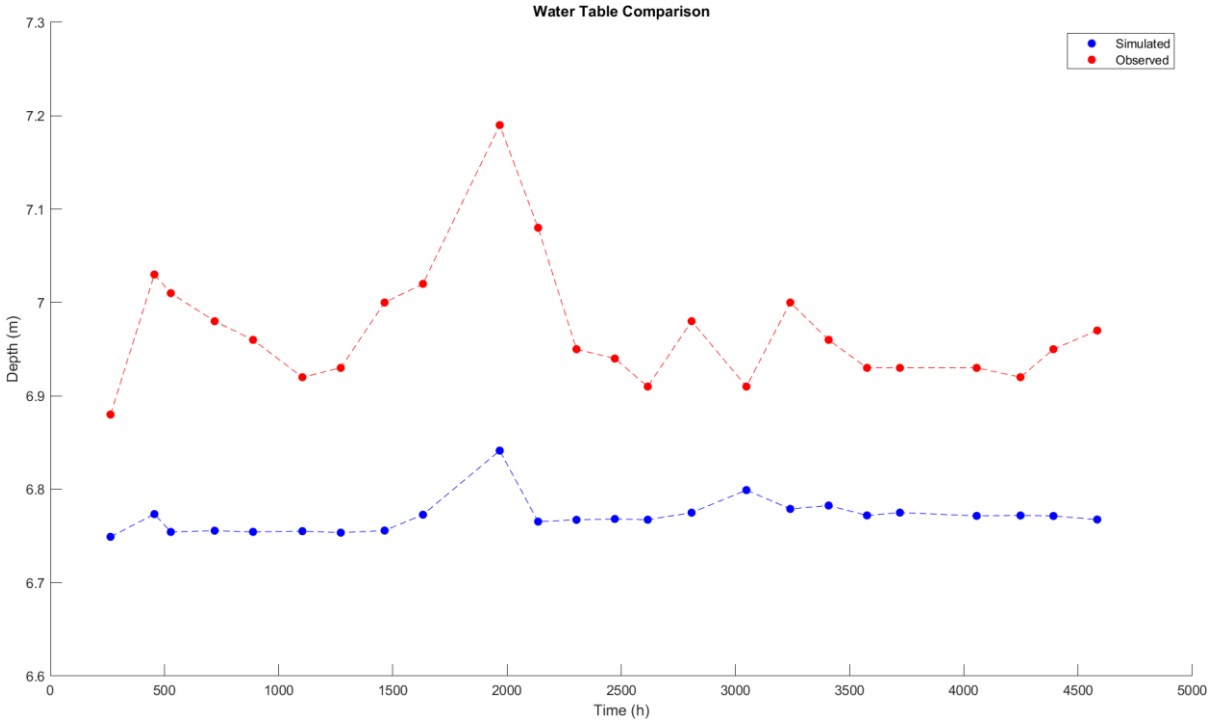

Figure 17. Water table comparison in the first borehole

S2 (Second Borehole)

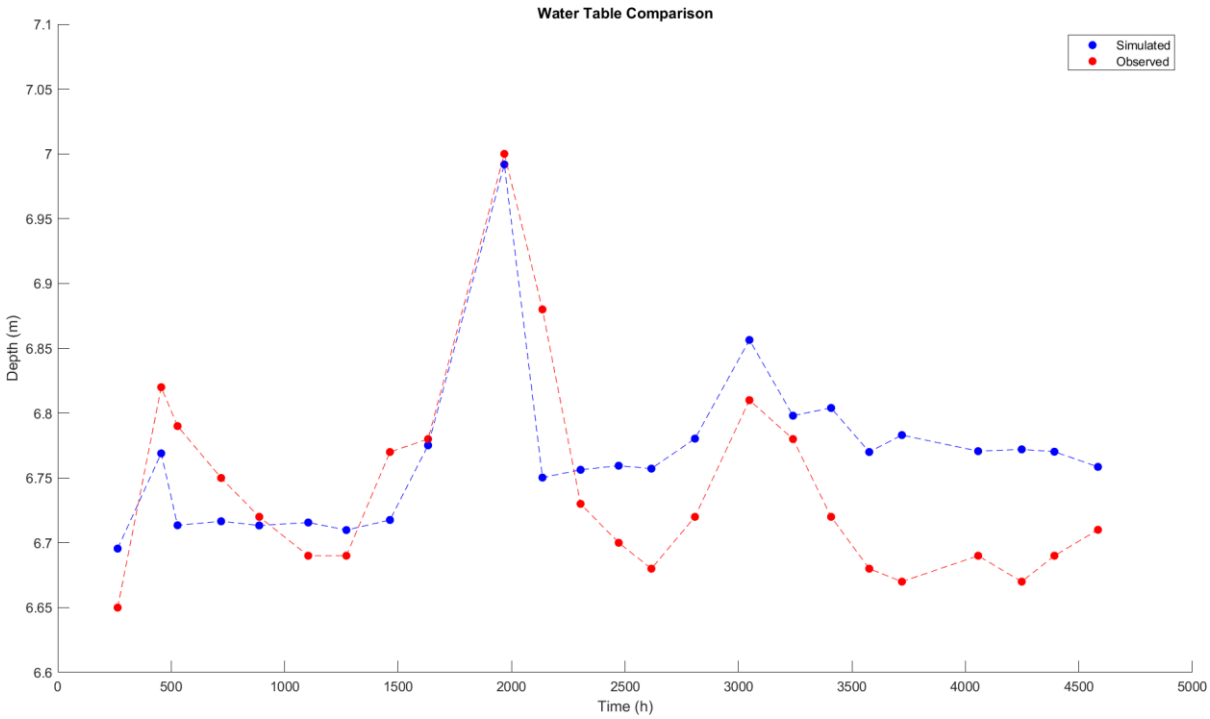

Figure 18. Water table comparison in the second borehole

S3 (Third Borehole)

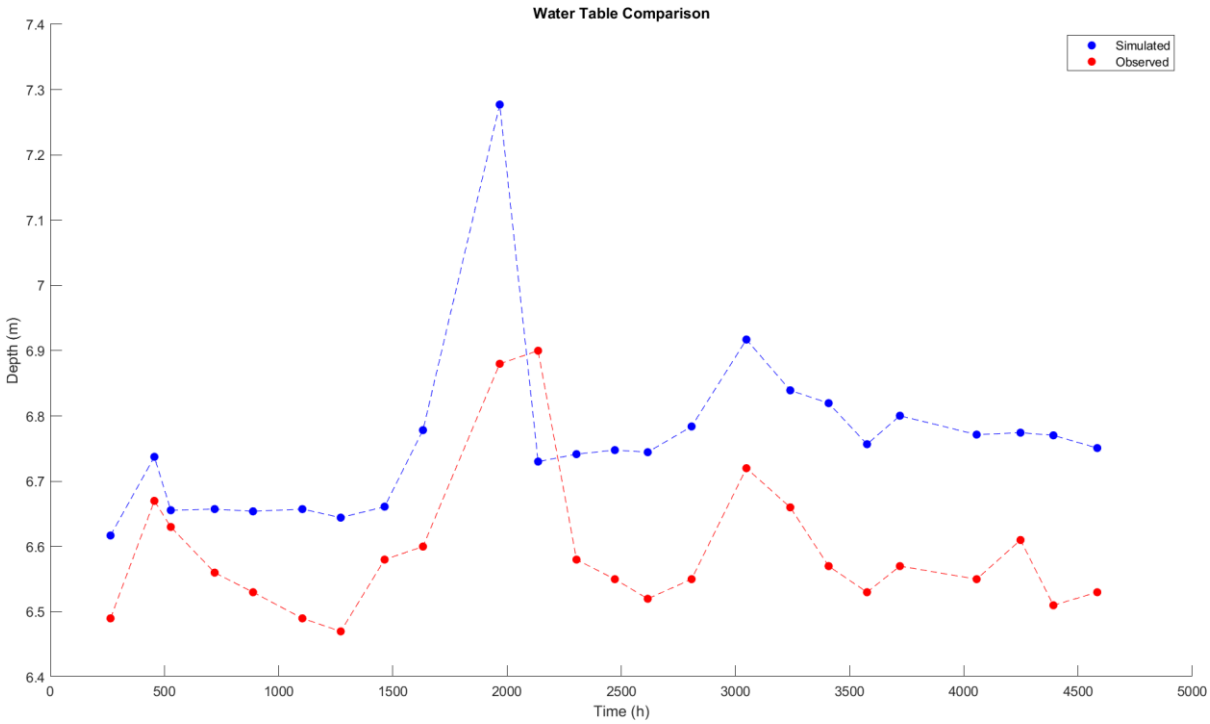

Figure 19. Water table comparison in the third borehole

S4 (Fourth Borehole)

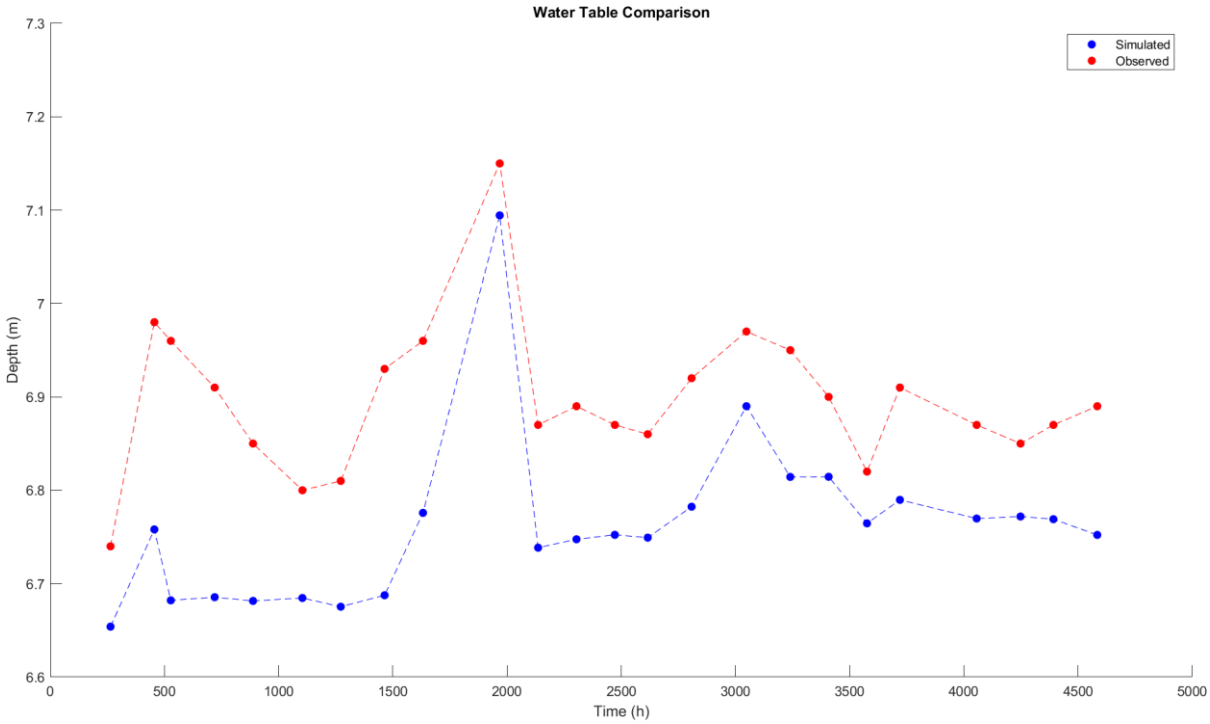

Figure 20. Water table comparison in the fourth borehole

S5 (Fifth Borehole)

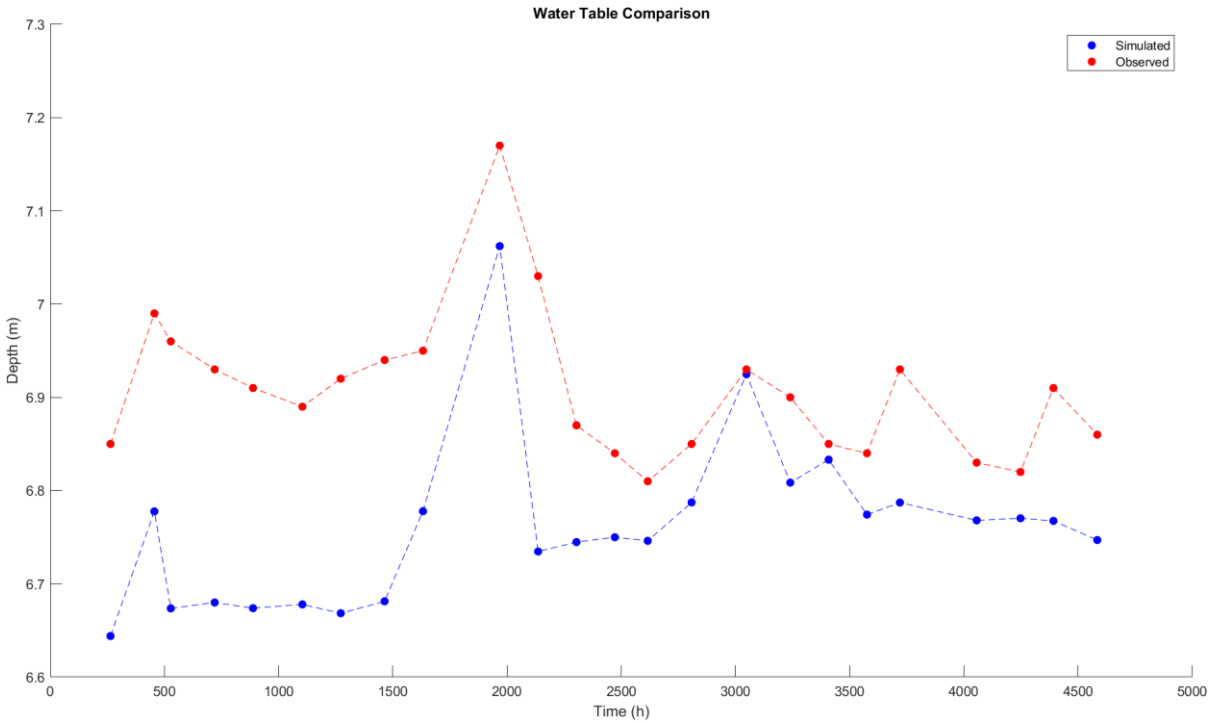

Figure 21. Water table comparison in the fifth borehole

Figure 16 to 20 present a detailed the comparison of water table levels between the simulated result and the observed data. In Figure 16, a consistent underestimation trend of water table is observed, with all simulated values falling below the corresponding observed data points. However, in the subsequent figures, the disparity between the simulated and observed values appears to decrease, indicating a closer alignment between two datasets. The exception is presented in the second borehole. It presents a bit better water table dynamic with the observed data. Hence, the most optimum graph is displayed from the second borehole, with simulated values closely matching the observed data.

3.3 Calibrated simulation

The result of calibrated simulation is presented in the following section focusing on three key variables: water content, pressure head, and water table dynamics. On the aforementioned section regarding SCE-UA method, the model is calibrated taking into account those three key variables. Calibration utilized statistical approach of Kling-Gupta Efficiency (KGE). As a result, the model produces calibrated hydraulic and VGM parameters. The values are hydraulic conductivity (Ks) of silt loam of 22.4 cm/day, porosity (θ_s) of 0.367, n of 1.28, residual porosity (θ_r) of 0.0912, and inverse α of 0.229. The results below is started with the water content in the first borehole.

3.3.1 Water content

S1 (The first boreholes)

The initial water content in the first borehole is computed by multiplying the water saturation value from the CATHY result by the calibrated porosity, taking into account the analysis for four distinct layers. For the first layer, located at the depth of 0.1 m, the calibrated simulation mirrors a closely trend that of the observed data (Figure 22).

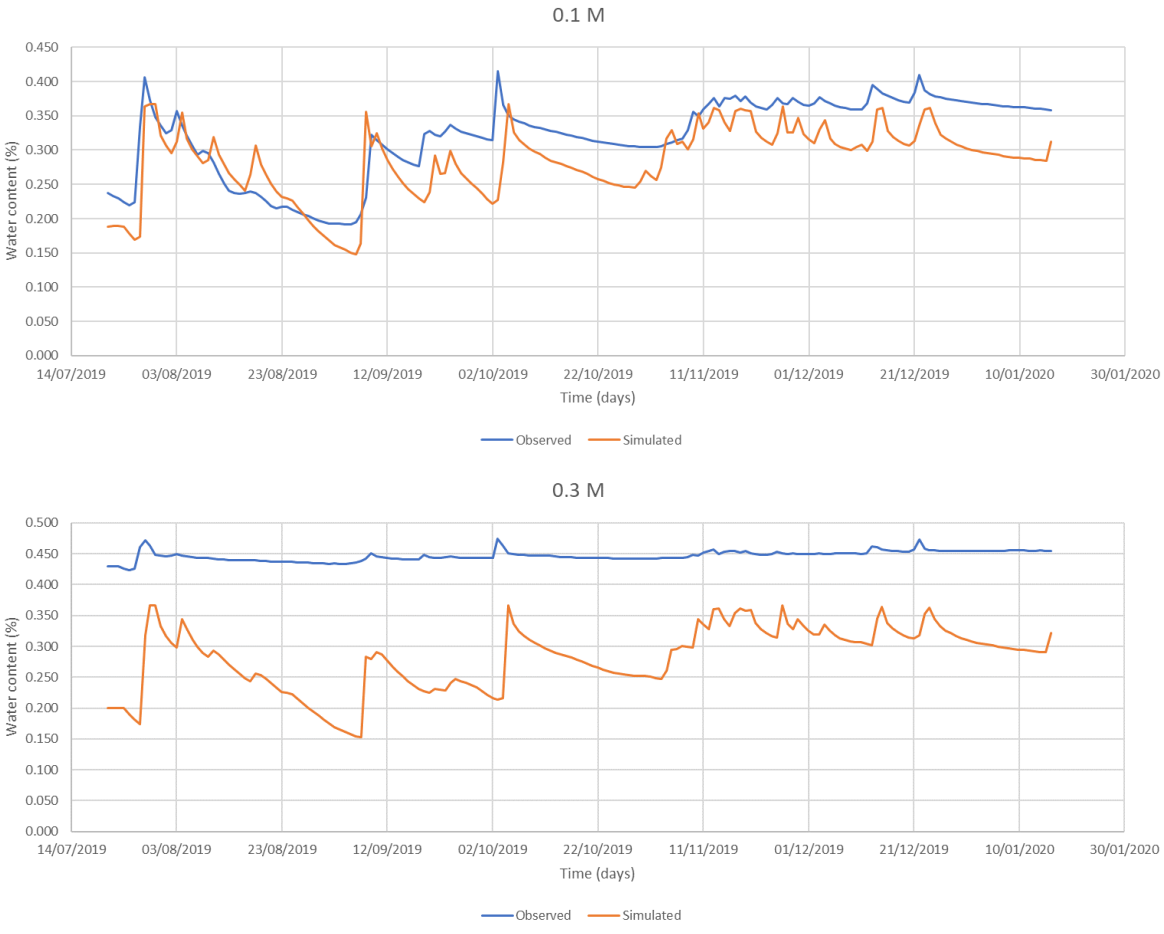

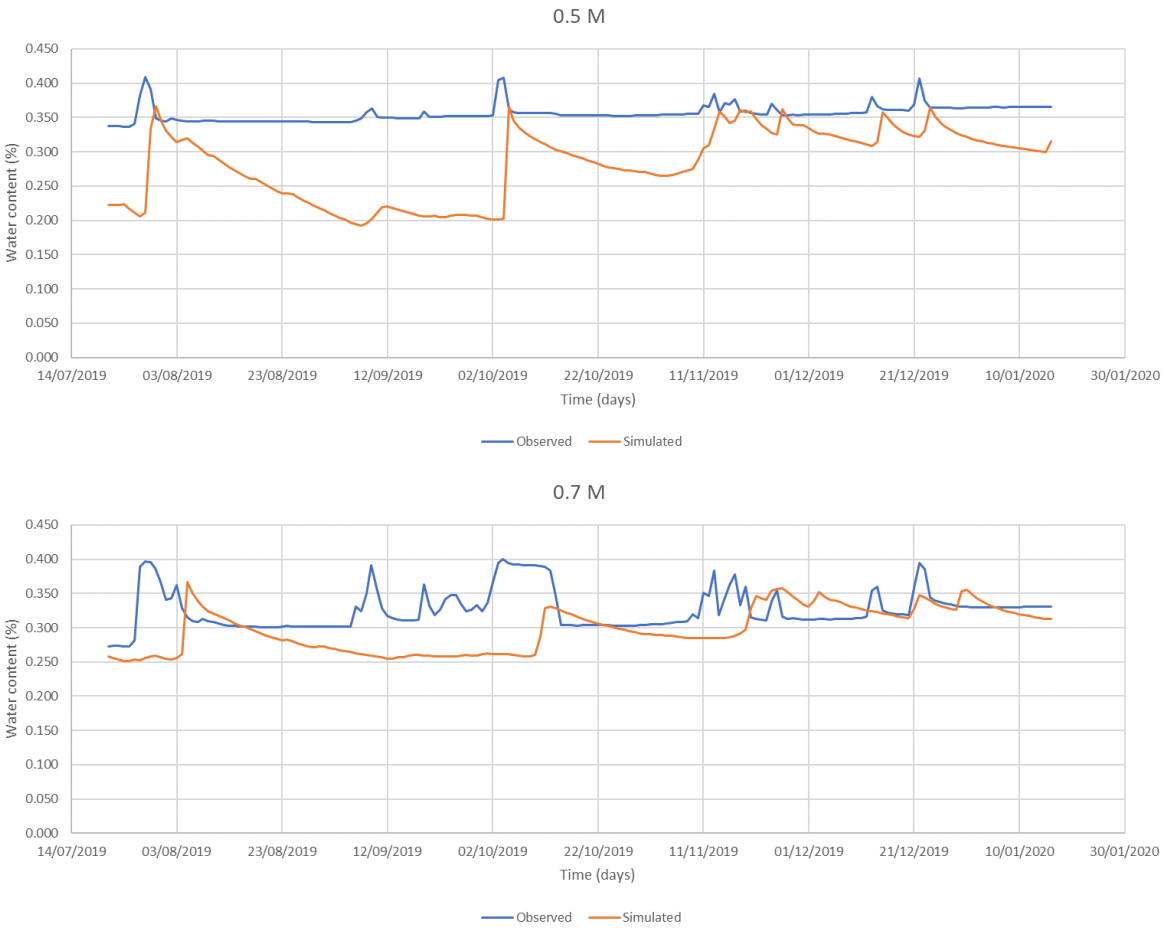

Figure 22. Water content dynamics of the first borehole after calibration

However, at the depth of 0.3 m and 0.5 m, the simulation result indicates an underestimation, leading to a significant disparity between observed data and simulated values. Conversely, the layer at depth 0.7 m demonstrates a trend with a narrow gap between the simulated and observed values (see Figure 22).

S2 (The second borehole)

The calibrated analysis of water content in the second borehole revealed values closely align with the porosity at depths of 0.1 m and 0.5 m. The graphs exhibit a similar pattern with the observed data, albeit with a narrower gap observed at 0.1 and 0.5 m compared to 0.3 and 0.7 m. This suggests a higher precision in the results for the 0.1 m depth after calibration. However, a noticeable underestimation is noted at 0.3 m and 0.7 m presented in the plots. Hence, the observed data deviate in pattern at the both depths (see Figure 23).

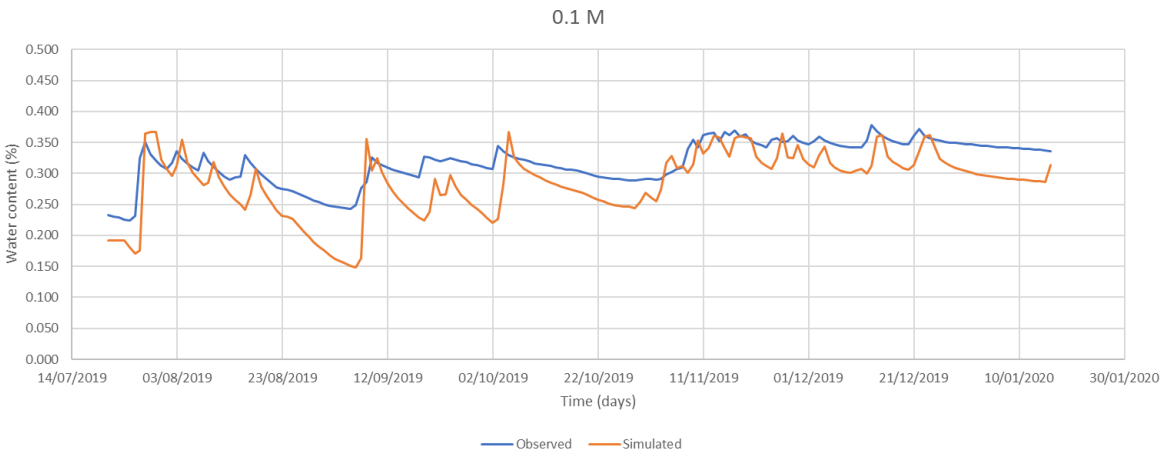
0.1 M
Water content (%)
0.500
0.450
0.400
0.350
0.300
0.250
0.200
0.150
0.100
0.050
0.000
14/07/2019
03/08/2019
23/08/2019
12/09/2019
02/10/2019
22/10/2019
11/11/2019
01/12/2019
21/12/2019
10/01/2020
30/01/2020
Time (days)
Observed
Simulated

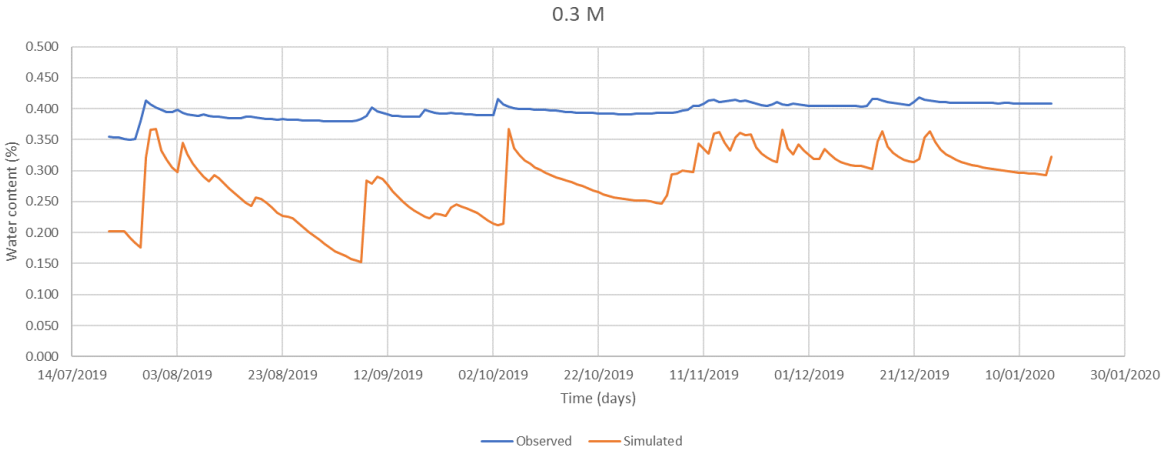
0.3 M
Water content (%)
0.500
0.450
0.400
0.350
0.300
0.250
0.200
0.150
0.100
0.050
0.000
14/07/2019
03/08/2019
23/08/2019
12/09/2019
02/10/2019
22/10/2019
11/11/2019
01/12/2019
21/12/2019
10/01/2020
30/01/2020
Time (days)
Observed
Simulated

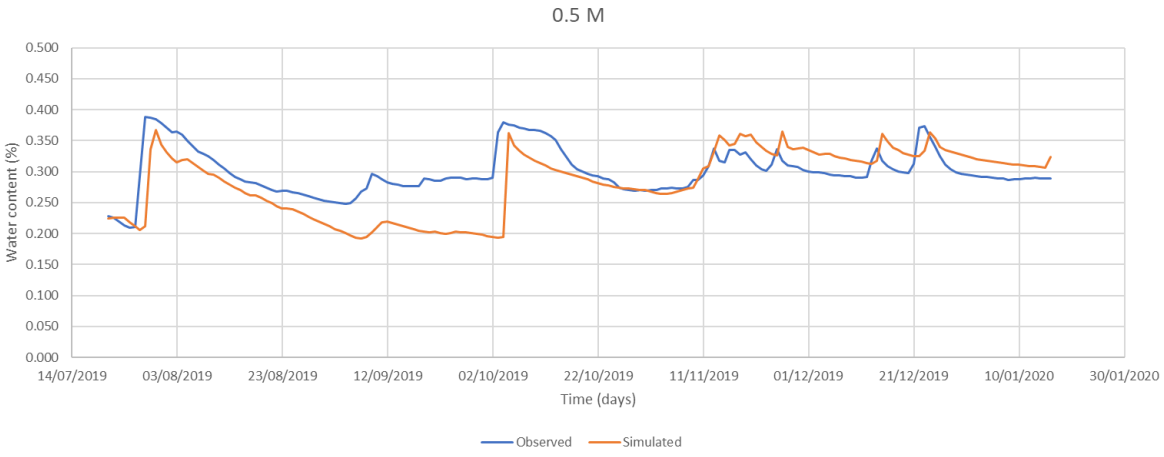
0.5 M
Water content (%)
0.500
0.450
0.400
0.350
0.300
0.250
0.200
0.150
0.100
0.050
0.000
14/07/2019
03/08/2019
23/08/2019
12/09/2019
02/10/2019
22/10/2019
11/11/2019
01/12/2019
21/12/2019
10/01/2020
30/01/2020
Time (days)
Observed
Simulated

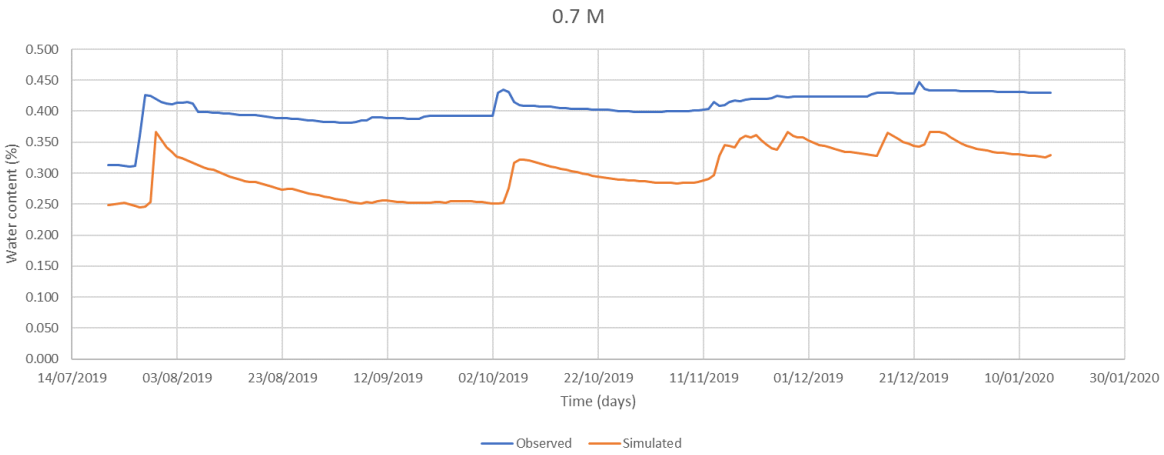

Figure 23. Water content behaviour of the second borehole after calibration

S3 (The third borehole)

The calibrated water content analysis for the third borehole presents shortcomings in accurately representing the observed data. Notably, at depths of 0.1 m, 0.3 m and 0.5 m, most segments of the graph align with the observed data. Conversely, there is a complete lack of correspondence between the simulated result and observed data at depth of 0.7 m (Figure 24). Intriguingly, a notable observation is that all the result is only underestimated for the depth of 0.7 m, indicating a significant disparity between the simulated results and actual measurements. This discrepancy underscores the need for further refinement and calibration to achieve a more accurate representation of water content dynamics at greater depths within the borehole.

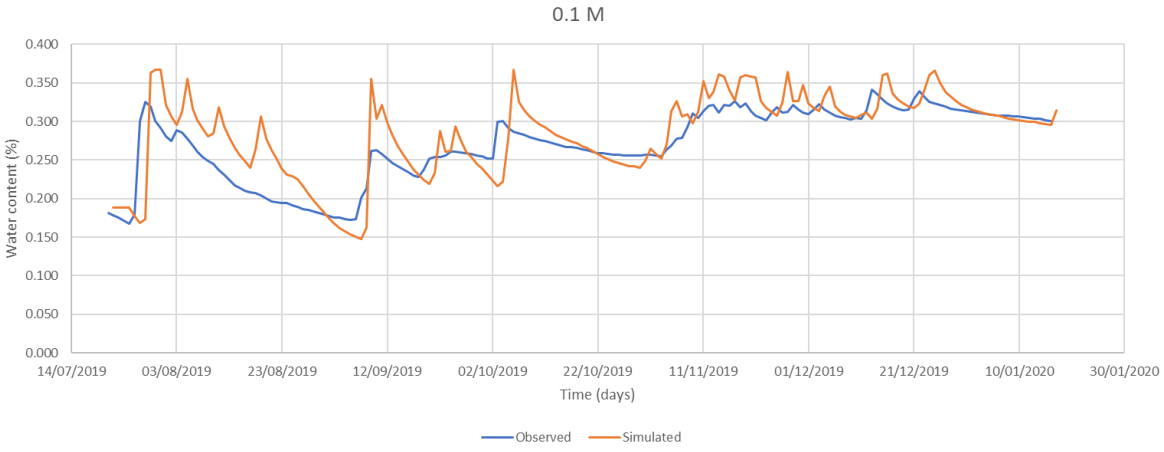

Figure 24. Water content dynamics of the third borehole after calibration

S4 (The fourth borehole)

The assessment of calibrated water content dynamic in the fourth borehole reveals a consistent discrepancy, characterized by an underestimation across all depth. As illustrated in Figure 25, it is evident that the results at all depths fail to accurately align with the observed data, particularly evident during the initial stages of the simulation. The smallest gap shows at

the depth of 0.1 m where despite exhibiting a minorly similar trend to the observed pattern, the simulated data still fails to align closely. Conversely, at the depth of 0.3 m, the gaps widens between the data. This divergence is further exacerbated at the 0.5 m depth, where the simulated results deviate significantly from the trend of field measurement. Hence, the calibrated simulation fails to capture the nuanced variations observed in the field measurements, highlighting limitations in the model's ability to accurately regenerate the observed water content dynamics.

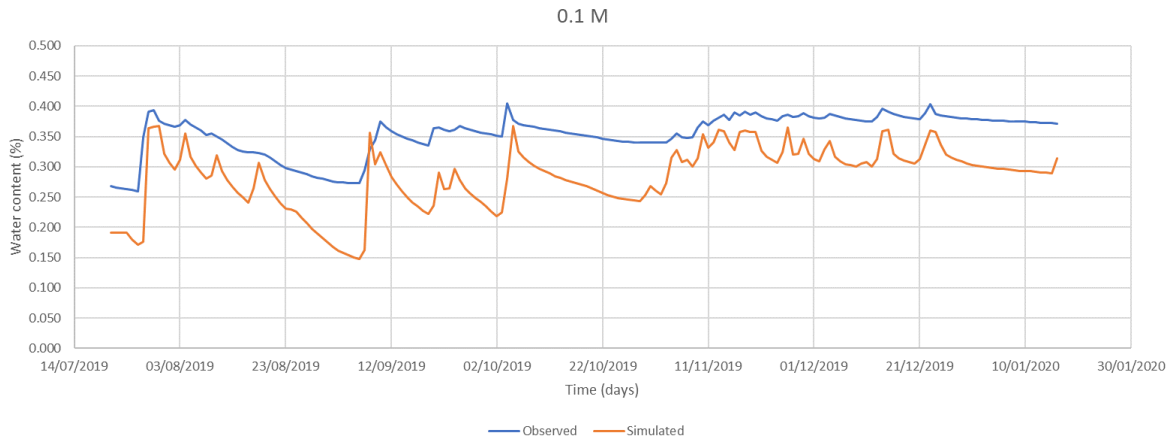

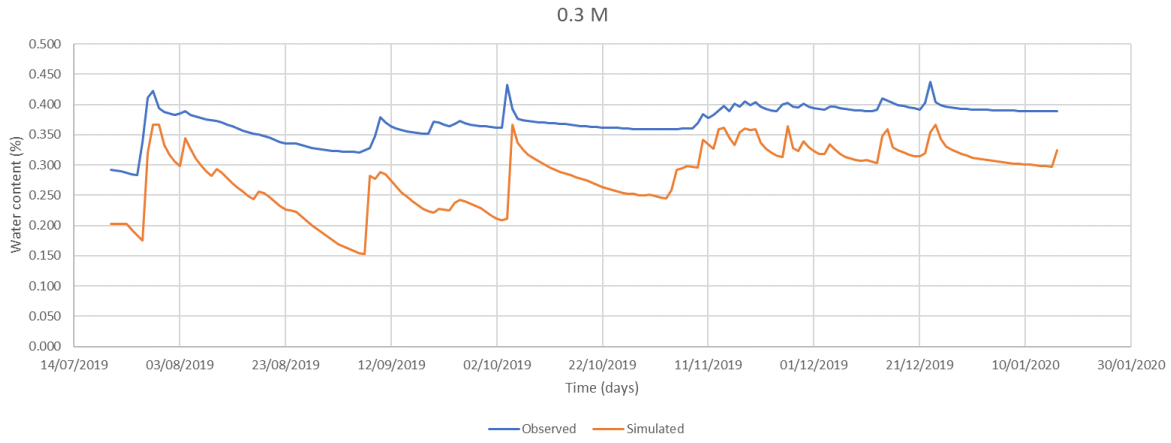

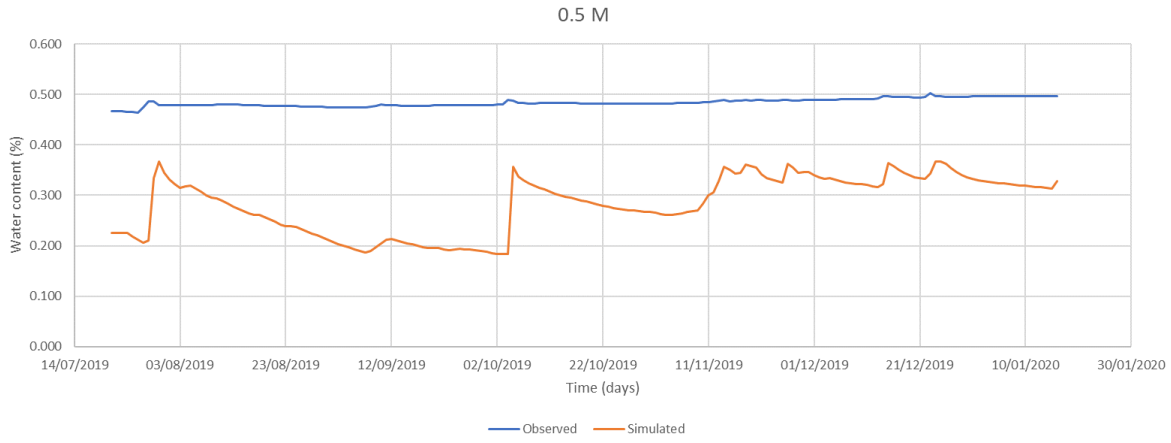

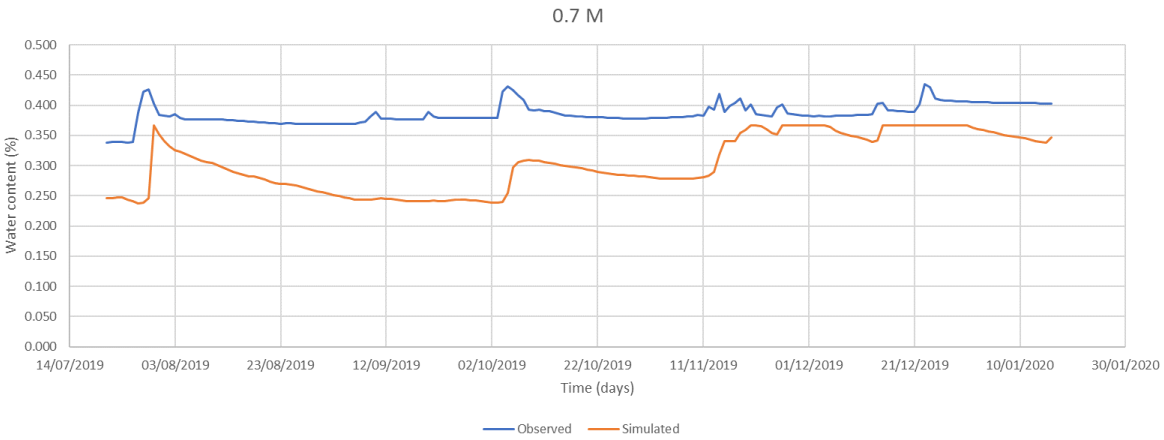

Figure 25. Water content dynamics in the fourth borehole

S5 (the fifth borehole)

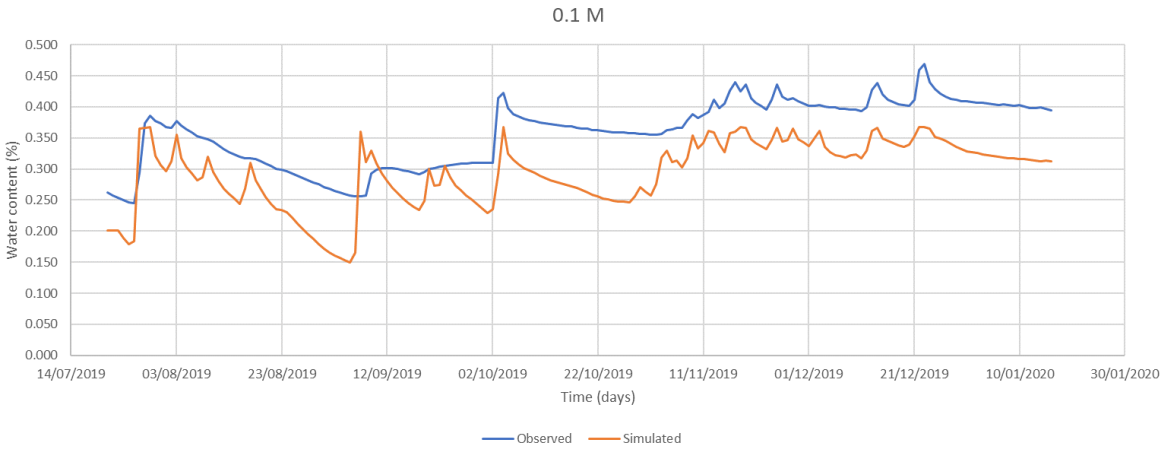

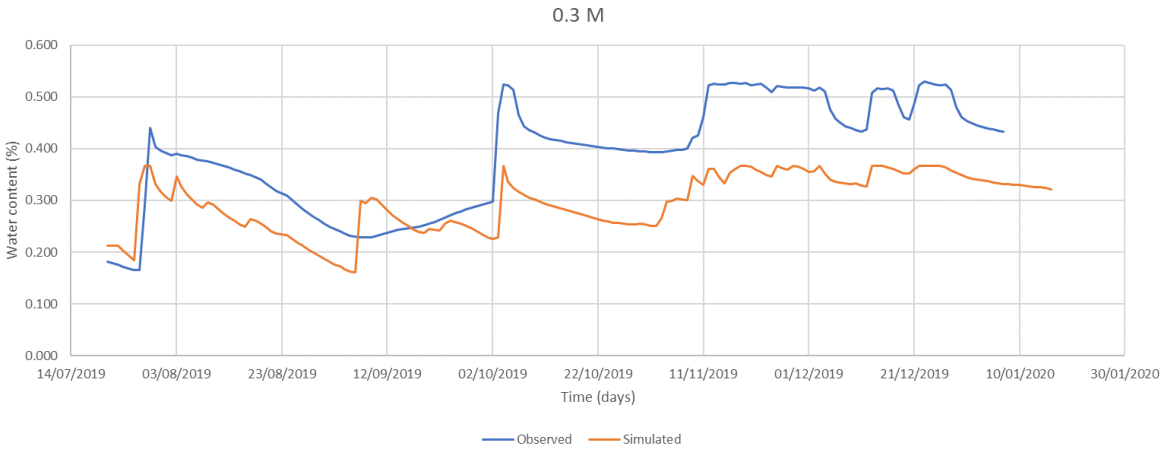

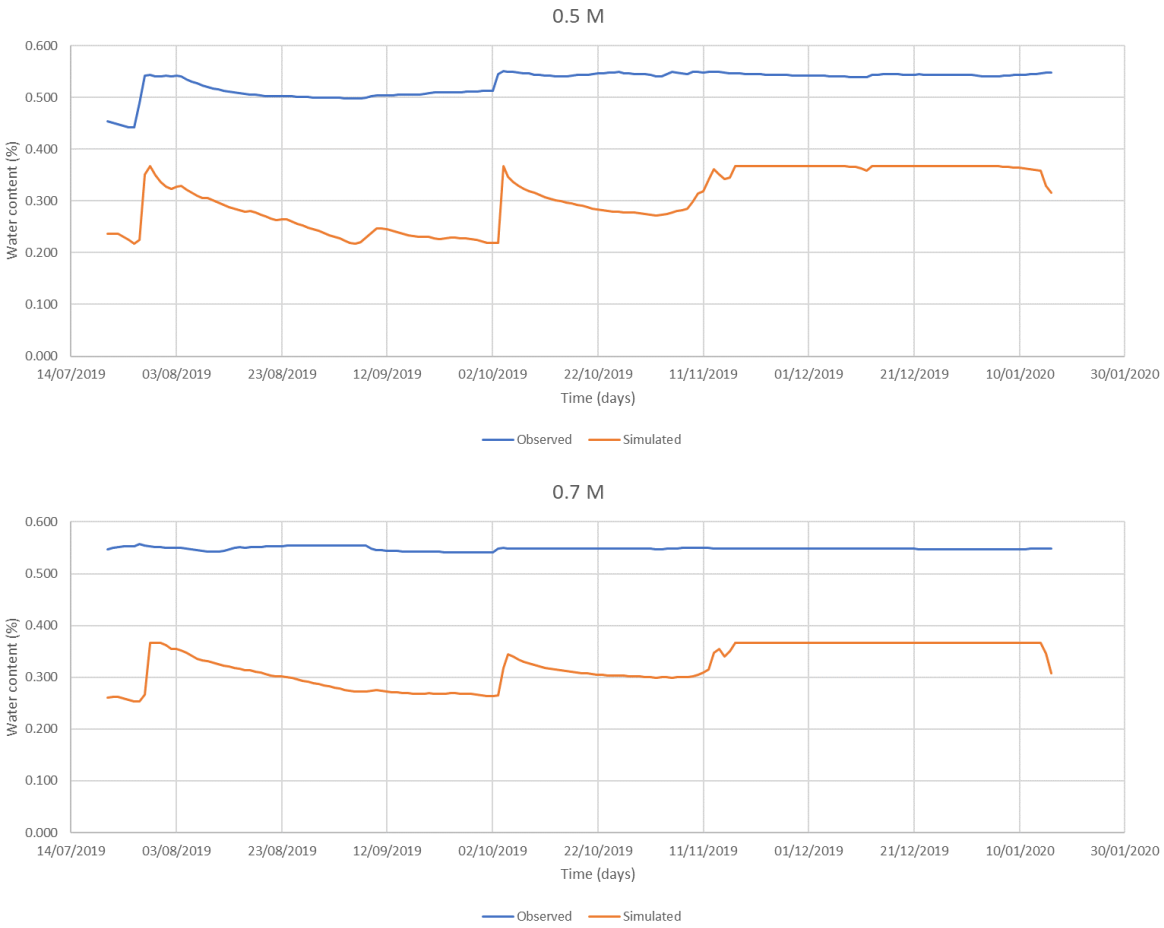

Figure 26. Water content behaviour comparison in the fifth borehole after calibration

The analysis for the fifth borehole fails to replicate similar results to the observed values, particularly at depths of 0.5 m and 0.7 m. The simulation falls short in capturing the fluctuation of water content evident in the observed data (refer to Figure 26). On the other hand, the results for depths of 0.1 m and 0.3 m manage to portray a relatively similar pattern to the observed data. Despite this, there is an underestimation in the simulation across all the depth.

3.3.2 Pressure Head

S1 (First Borehole)

The calibrated simulation for the first borehole presents deviations from the observed data, at both depths of 0.3 m and 0.5 m (see Figure 27). A notable observation is the presence of a data absence spanning from November 27th to December 29th, 2019 of the observed data, poses a challenge for accurate comparison. During this period, the simulated results fail to align with the observed data, indicating a lack of accuracy in representing the actual pressure head dynamics as well as highlighting a potential limitation in the model's ability to capture nuanced temporal variations. Hence, an improved measurement is needed to gain an accurate analysis of the model since the model is calibrated based on the field measurement data availability for rigorous model calibration and validation. Moreover, the absence of data for the depth of 0.7 m further complicates the comparison between simulated and observed results.

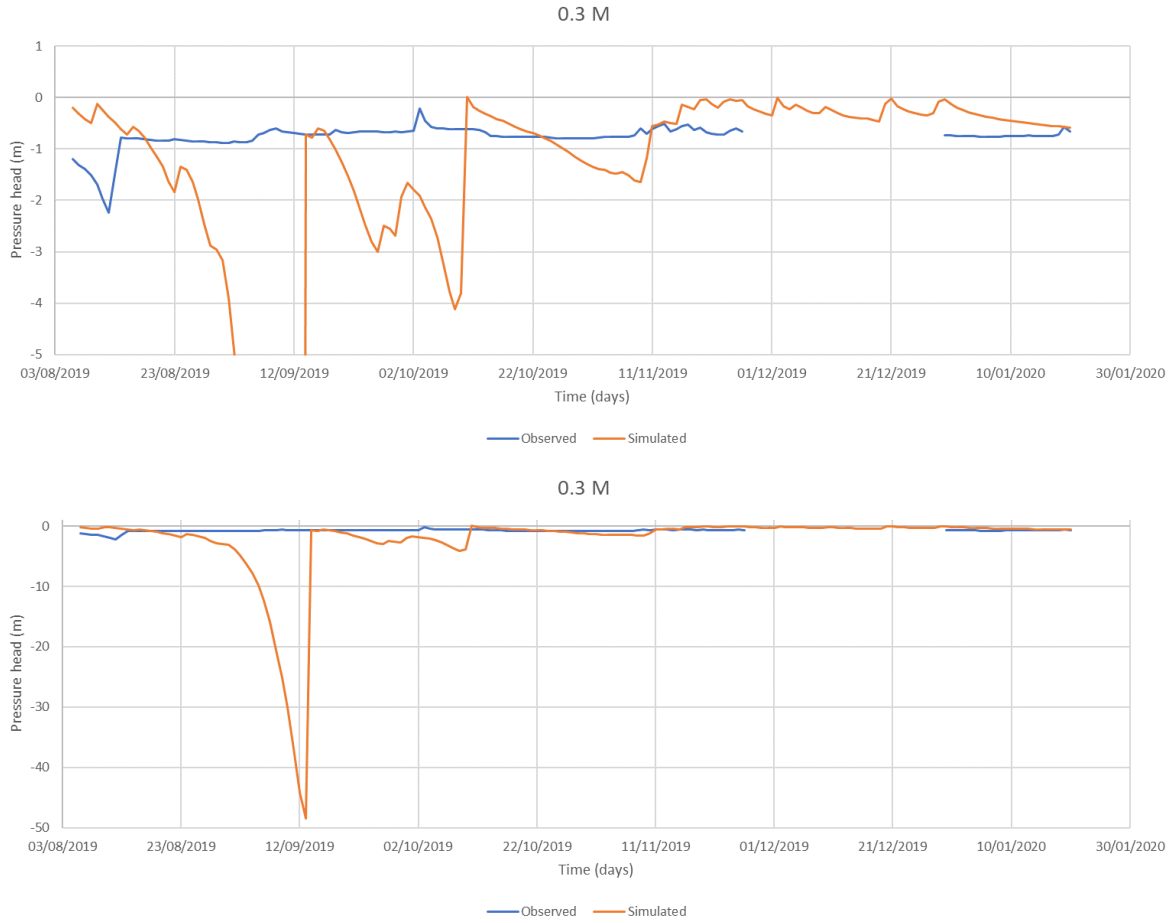

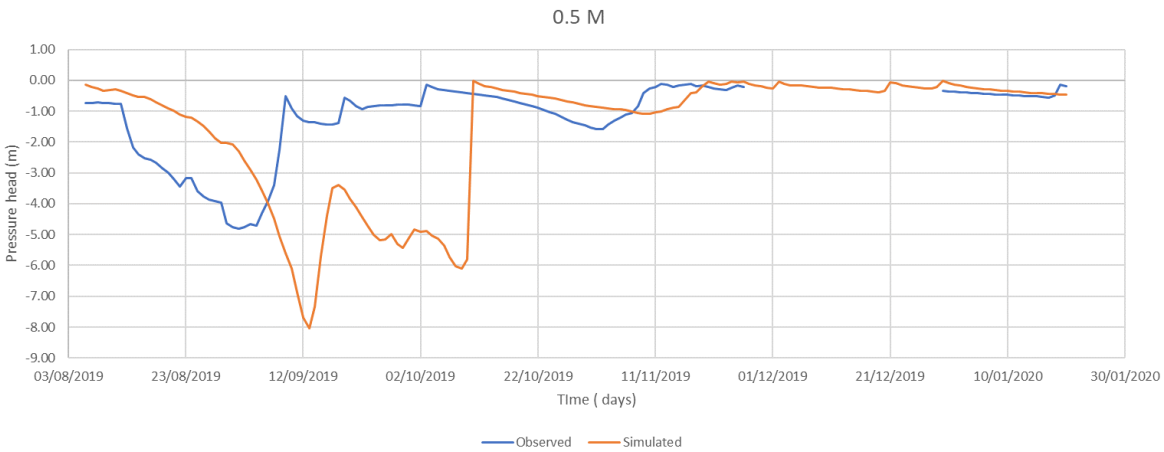

Figure 27. Pressure head dynamics in the first borehole after calibration

S2 (Second Borehole)

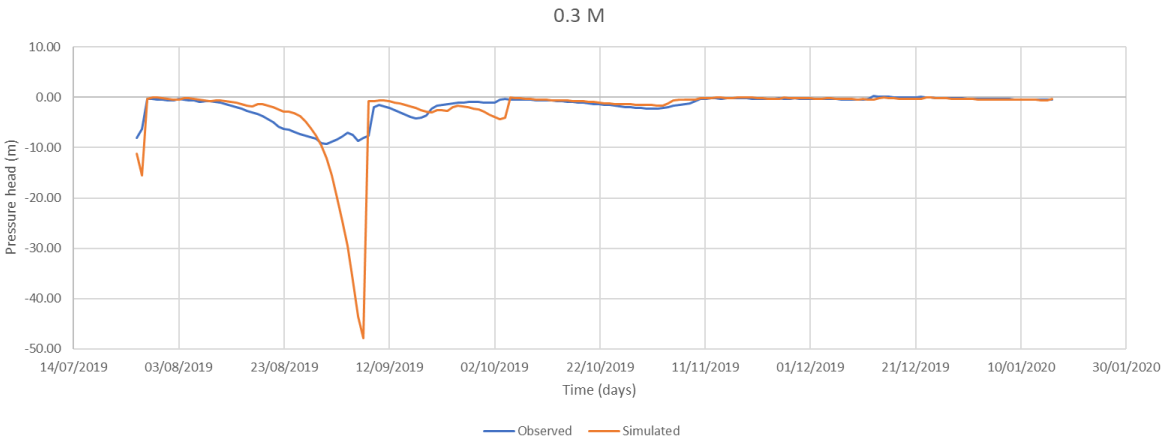

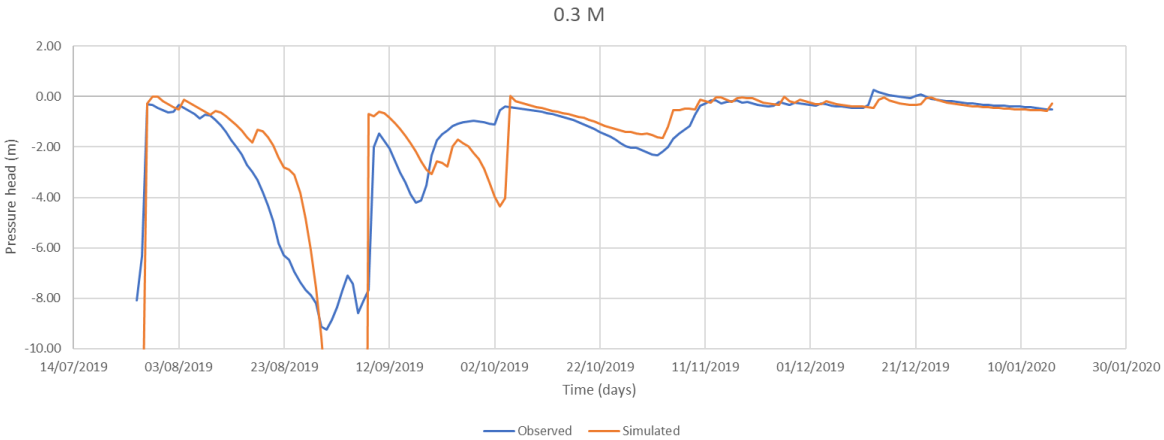

Figure 28. Pressure head dynamics comparison in the second borehole after calibration

The comparison between observed and calibrated simulation data in the second borehole revealed challenges almost for the all depths. At some point, the calibrated simulation was able to perform similar trend with the observed trend. But this result influences to the subsequent layer. Consequently, the patterns at the depth of 0.5 and 0.7 m failed to accurately generate the similar trend like the observed pattern. And both results have the similar pattern only from October 5th, 2019. Hence, the calibrated simulation only achieves a closer match at the depth of 0.3 m.

S3 (Third Borehole)

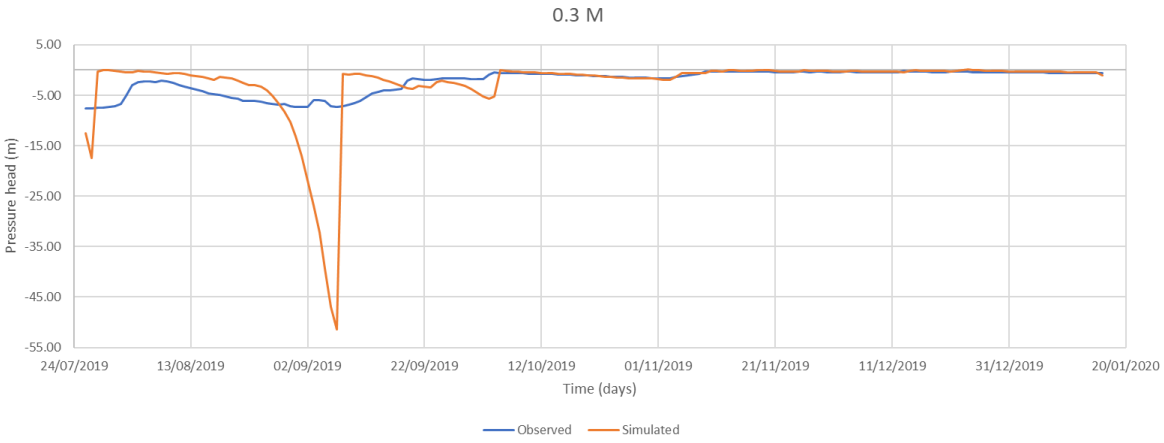

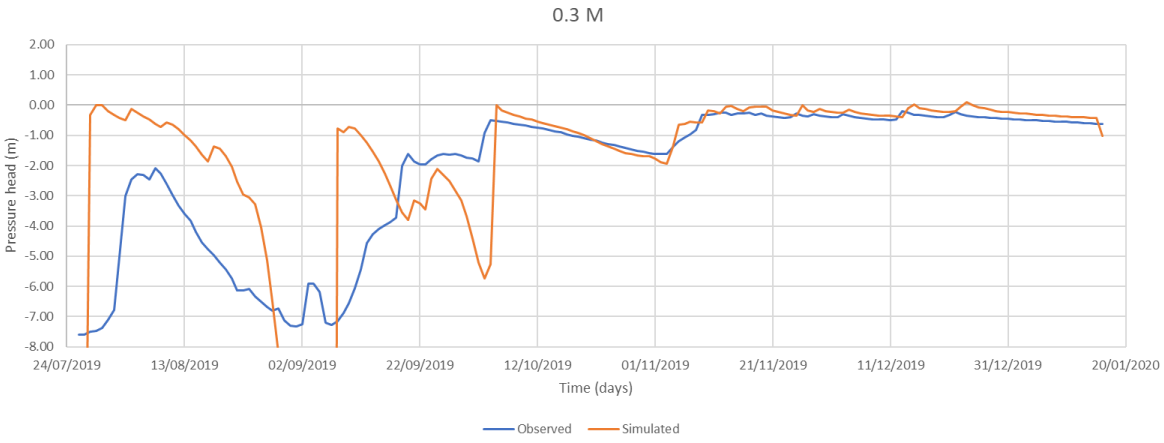

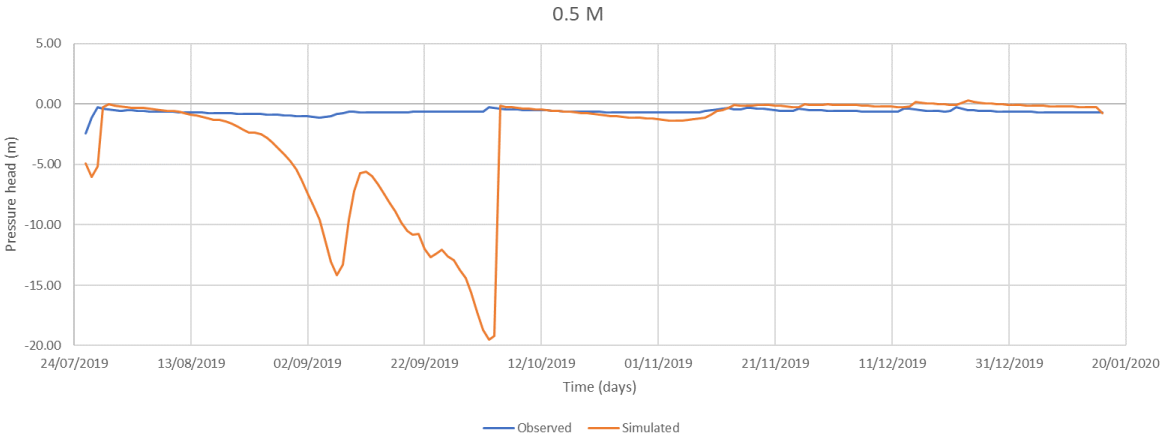

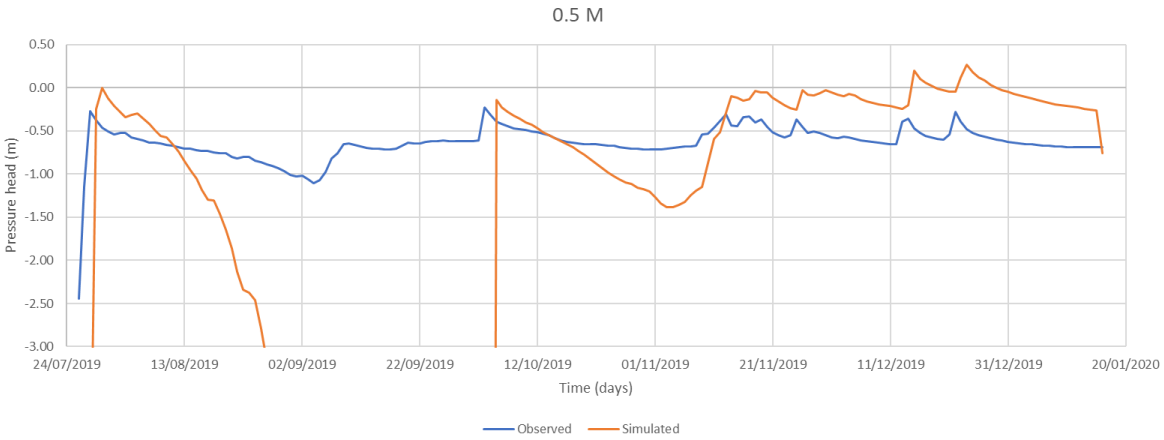

Figure 29. Water pressure head dynamic in the third borehole after calibration

The comparison between observed and simulated data at a depth of 0.3 m in the third borehole still poses challenges, primarily due to substantial data gaps persisting from July 26th to October 5th, 2019 (see Figure 29). These prolonged gaps in the datasets create obstacles in assessing the accuracy of simulation during this period, as they obscure vital information regarding the dynamics of pressure head. Consequently, the graphs depicting the simulated results fail to capture the nuanced variations in pressure head. At the depth of 0.5 m, the comparison is affected by the upper layer gaps, indicating a data gap occurred at depth of 0.3 m. Hence, it generates similar behaviour of pressure head dynamic. However, the simulation still faces difficulties in fully replicate observed trends. These challenges emphasize the need for comprehensive data to enhance simulation accuracy.

S4 (Fourth Borehole)

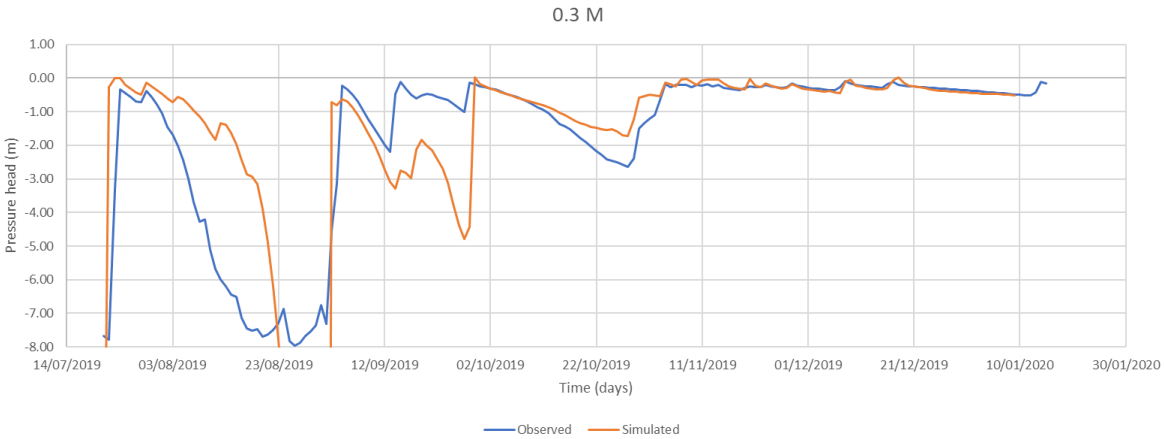

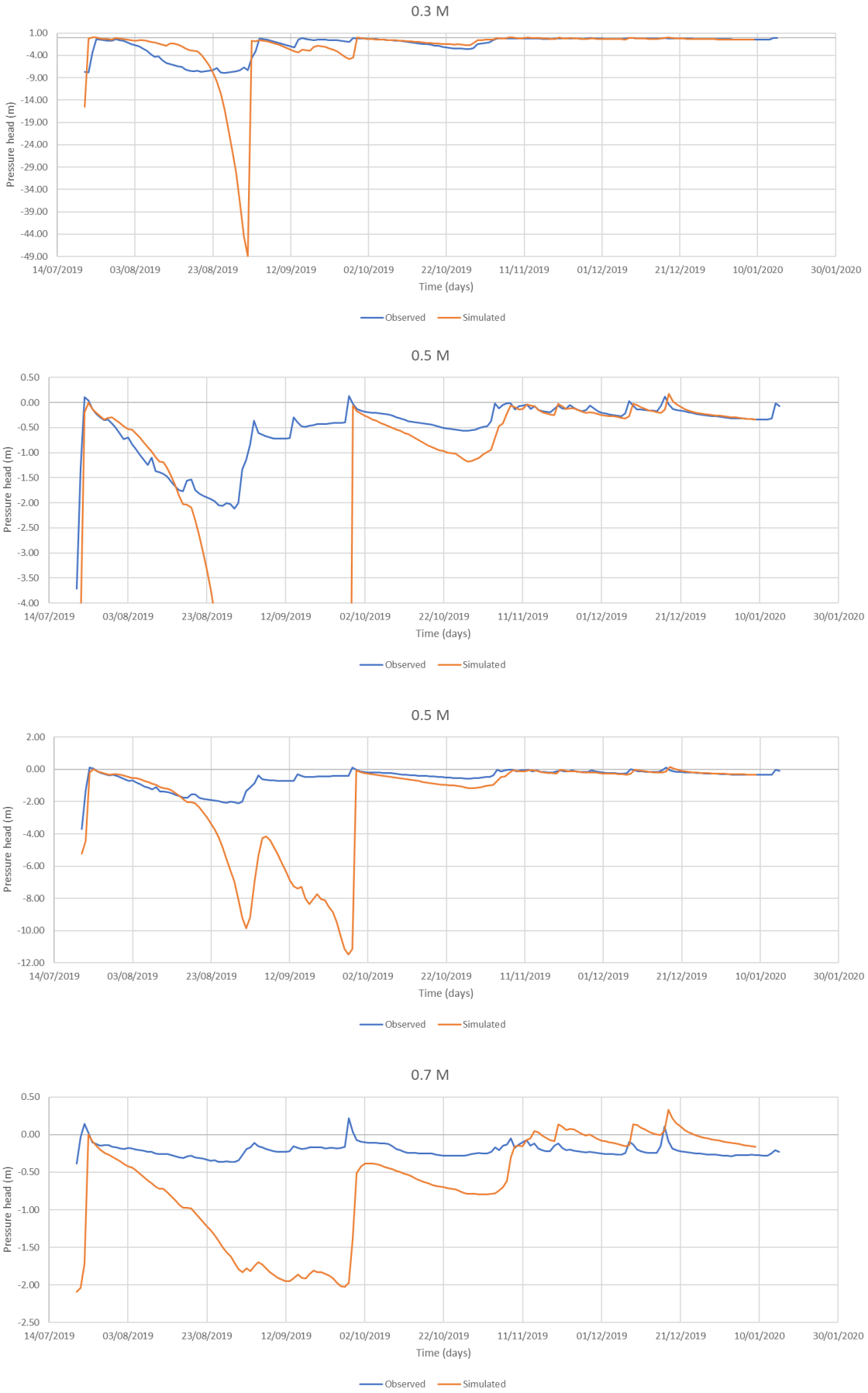

Figure 30. The pressure head dynamics in the fourth borehole after calibration

The comparison between observed and simulated data at the depths of 0.3 m and 0.5 m in the fourth borehole presents ongoing challenges, primarily due to significant data gaps persist from July 26th to September 5th, 2019 (see Figure 30). These gaps obstruct accurate assessment of simulation accuracy during this period, as they obscure crucial information regarding the dynamics of pressure head. Consequently, the graphs representing the calibrated simulation results fail to capture the nuanced variations in pressure head. It only shows a closer alignment starting from October 2nd, 2024. At the depth of 0.7 m, the comparison indicates wider gap between the simulated and the observed data, affected by the upper layer pressure head dynamics.

S5 (Fifth Borehole)

The assessment of observed versus simulated data at a depth of 0.3 m in the fifth borehole encountered difficulties due to significant data absence spanning from August 31st, to September 9th, 2019. Consequently, the evident influenced to the subsequent layer at the depth of 0.5 m, where the simulation fails to mirror the observed data as depicted in Figure 31. Despite the simulation demonstrating commendable accuracy in capturing the pressure head fluctuations in pressure head, certain discrepancies still exist between the simulated and the observed data. However, it is worth noting that the comparison of pressure head at the depth of 0.7 m is not feasible due to the unavailability of observed data.

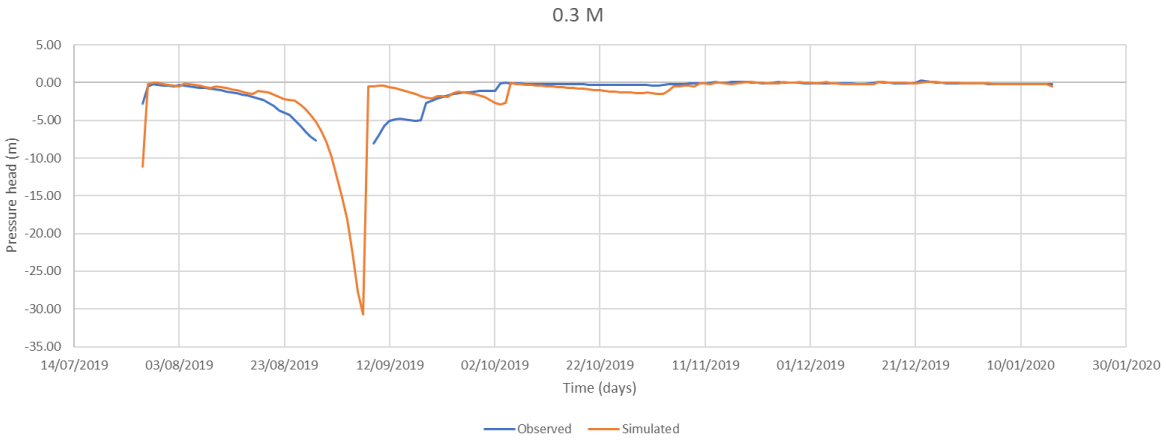

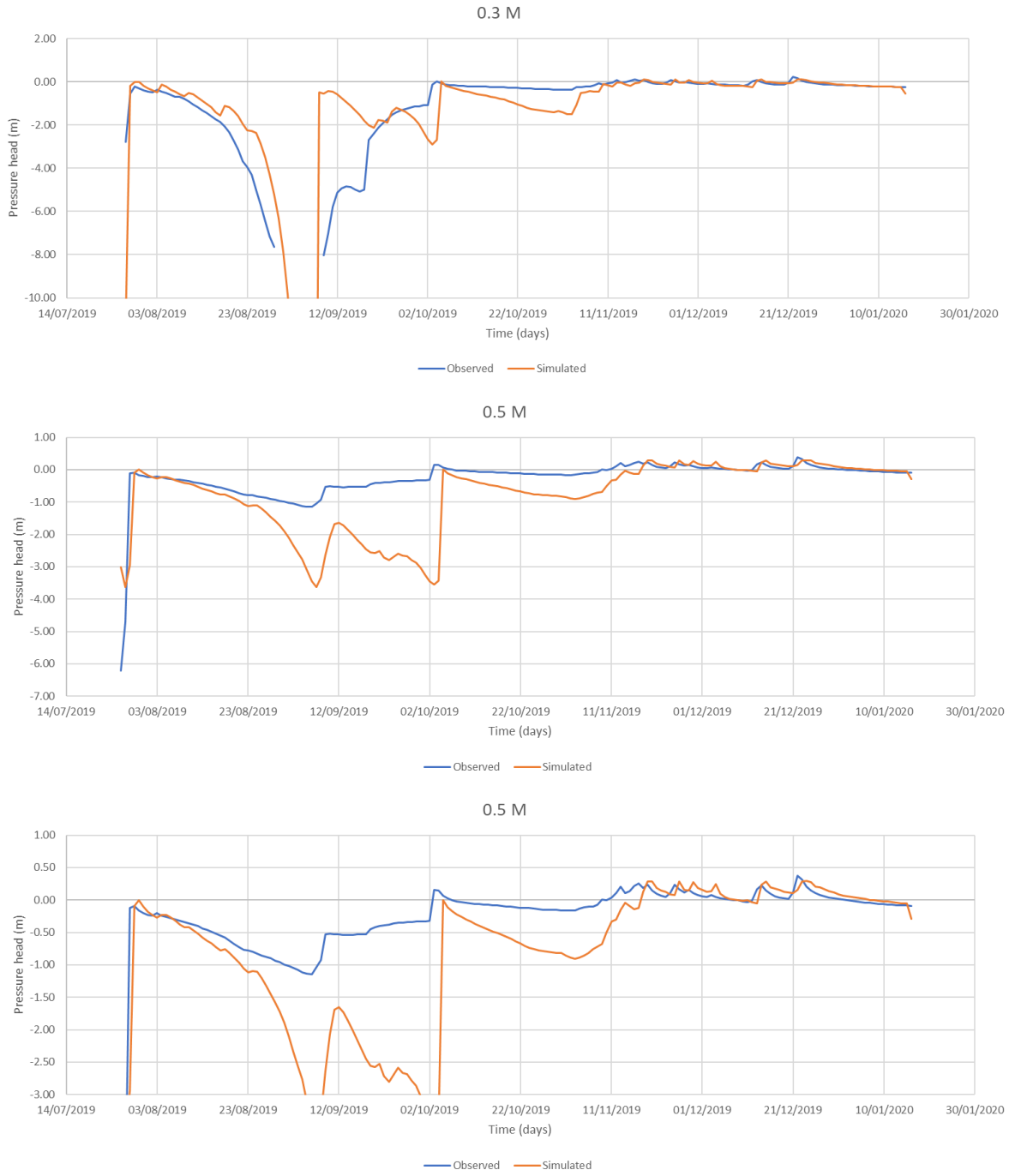

Figure 31. The pressure head dynamics in the fifth borehole after calibration

3.3.3 Groundwater table

S1 (First Borehole)

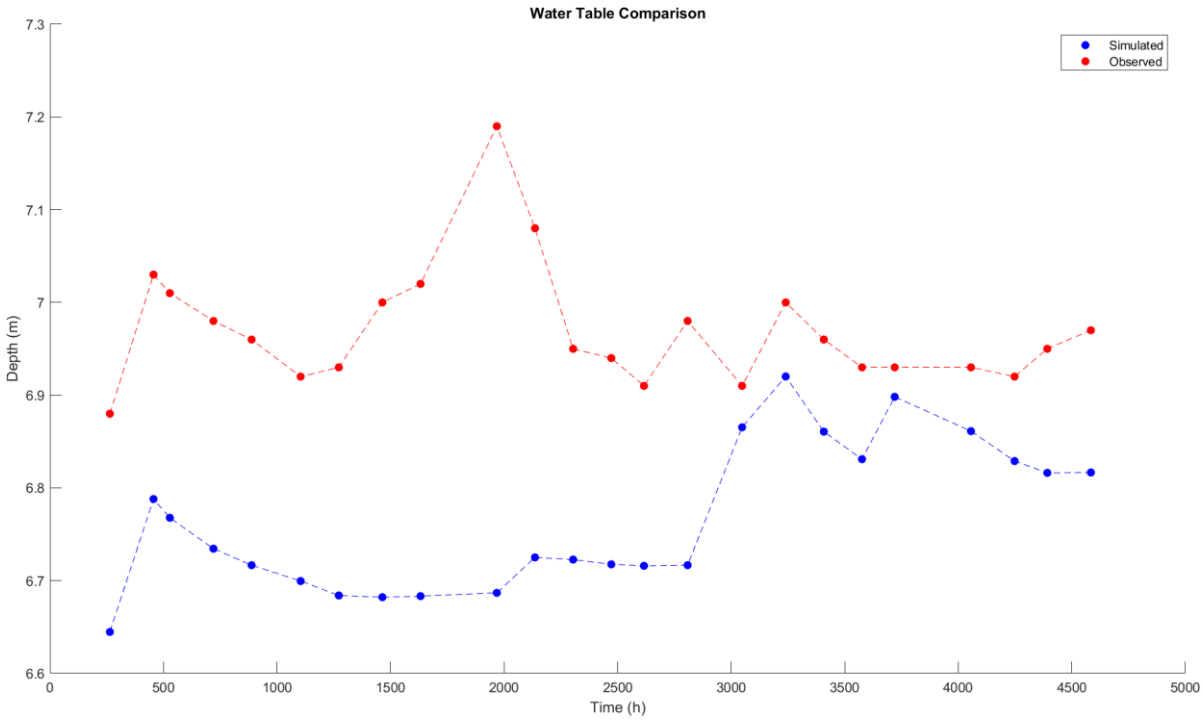

Figure 32. Water table comparison in the first borehole

S2 (Second Borehole)

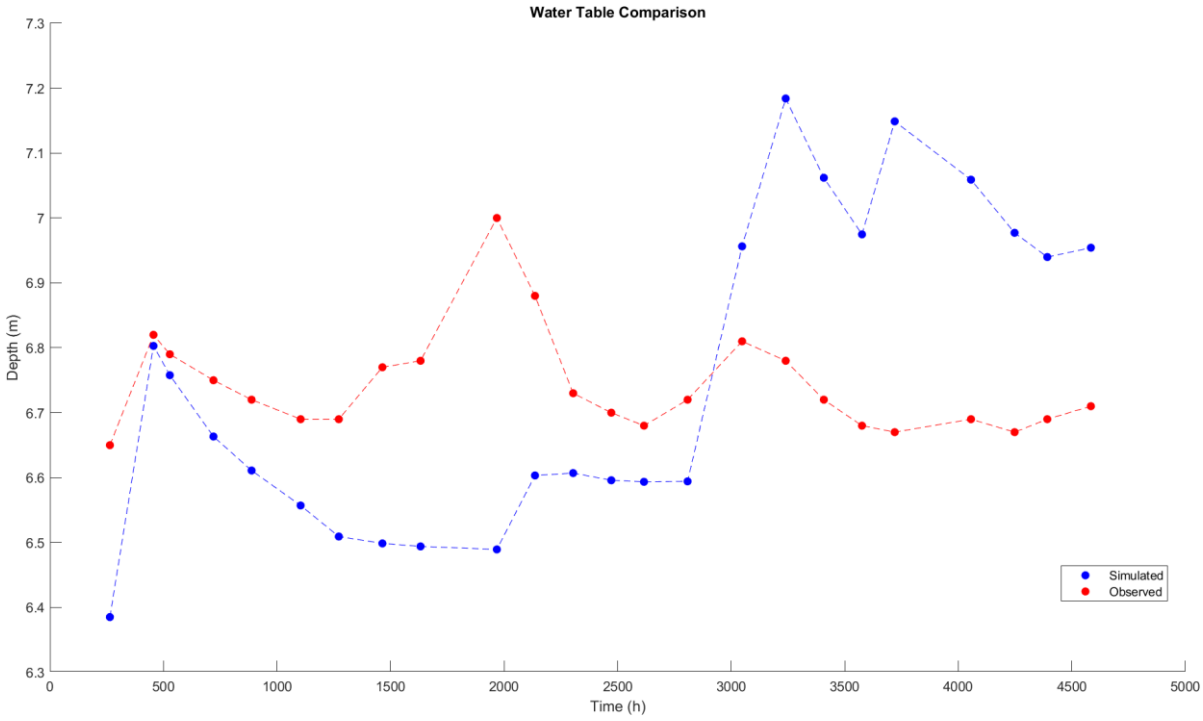

Figure 33. Water table comparison in the second borehole

S3 (Third Borehole)

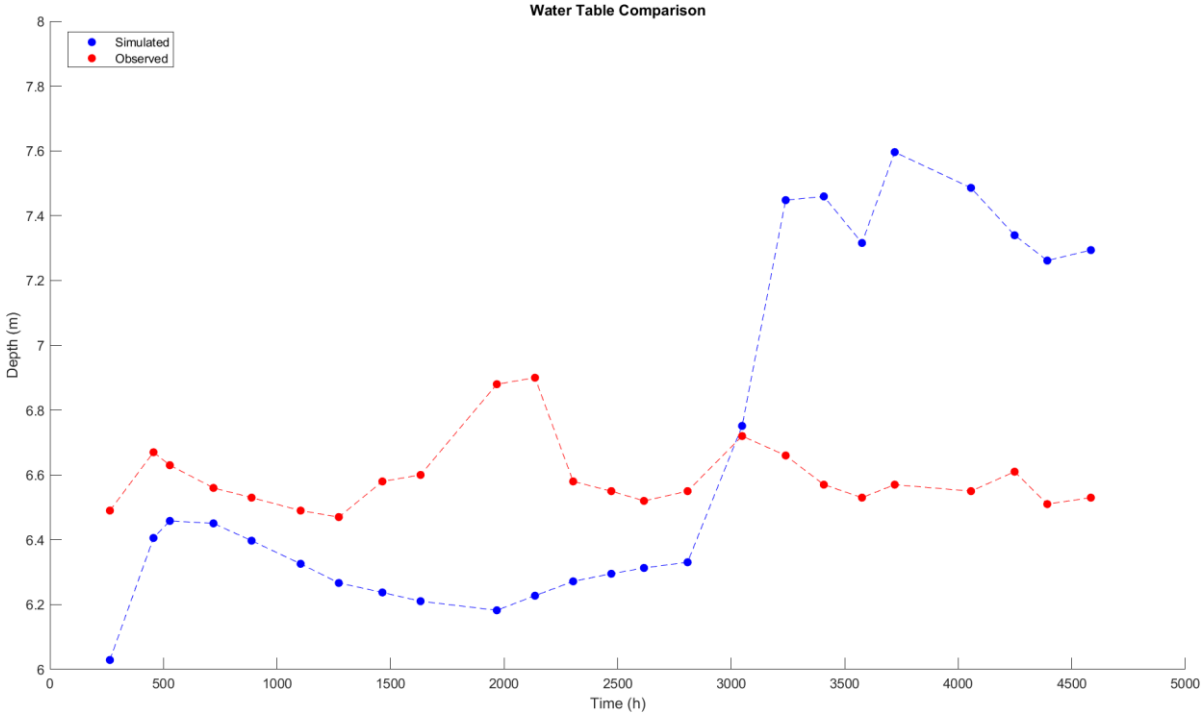

Figure 34. Water table comparison in the third borehole

S4 (Fourth Borehole)

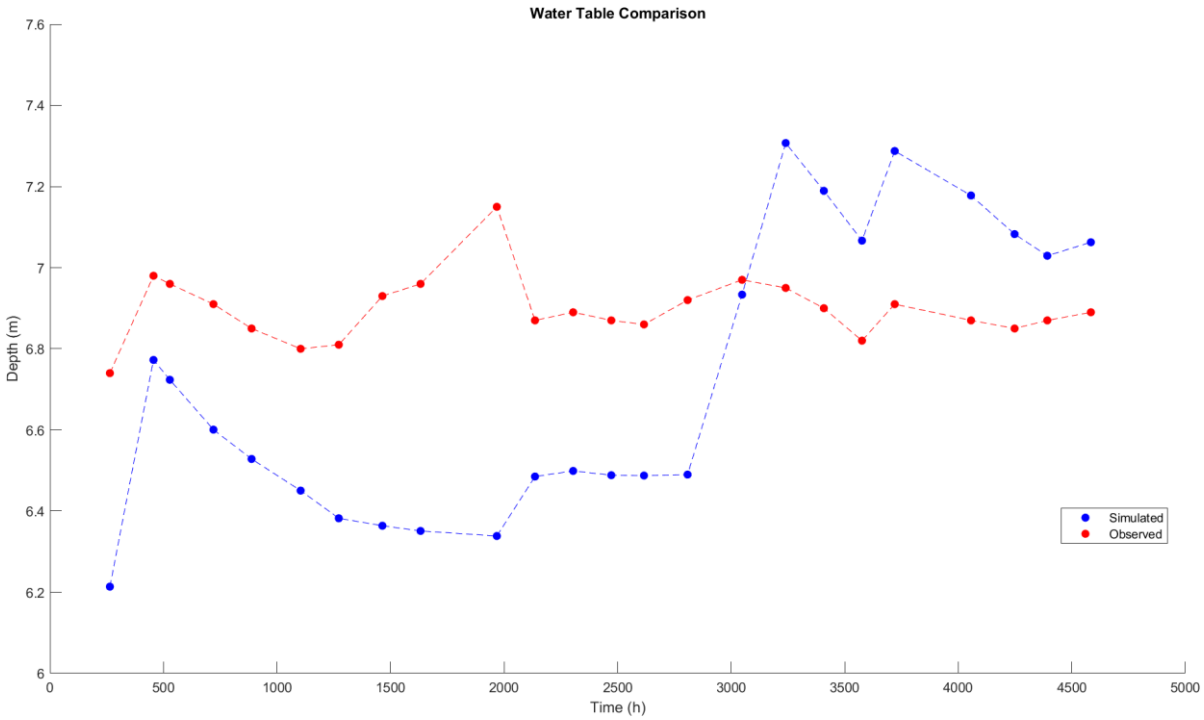

Figure 35. Water table comparison in the fourth borehole

S5 (Fifth Borehole)

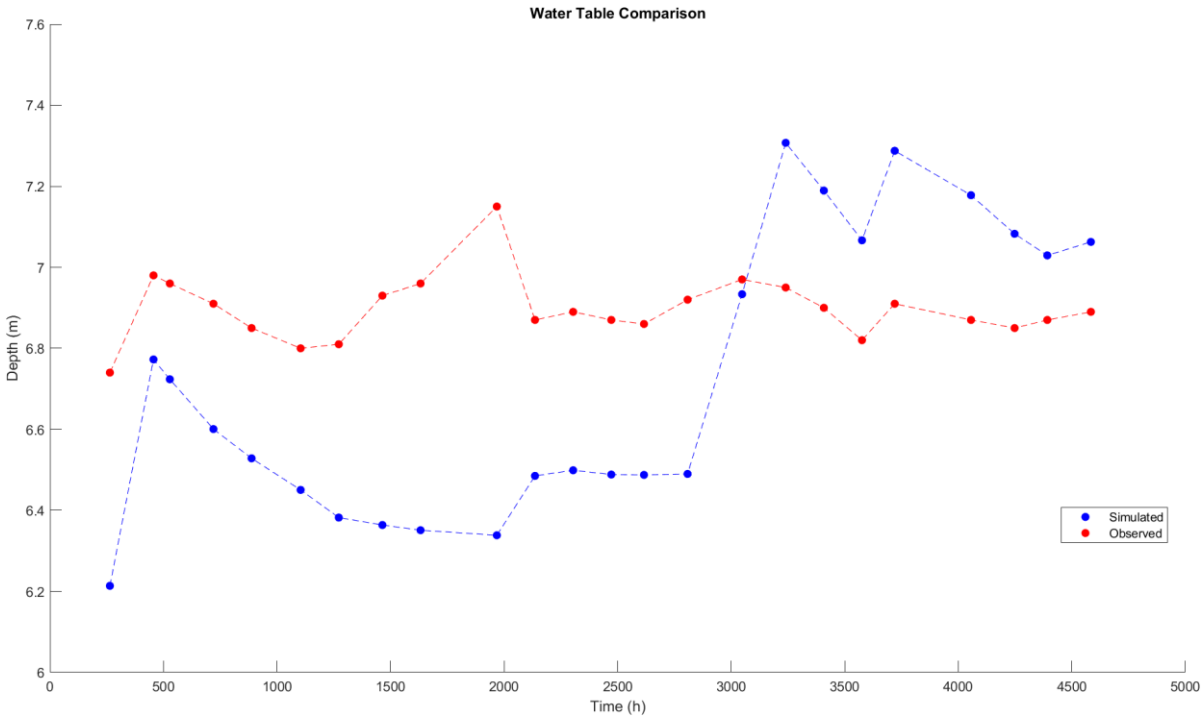

Figure 36. Water table comparison in the fifth borehole

Figure 32 to 36 provided a detailed the comparison of water table levels between the calibrated simulation and the observed data. Notably, in Figure 32, a consistent trend of underestimation in water table levels is observed, with all simulated values falling below the corresponding observed data points in the first borehole. However, in the subsequent figures, there is a discernible decrease in disparity between the simulated and observed values. This shift suggests a transition from underestimation to overestimation occurred in the simulated data, occurring approximately after 3000 hours (exist in the second until the fifth borehole).

CHAPTER 4

4. DISCUSSION and CONCLUSIONS

The comparison between the Rosetta model and laboratory analysis reveals variations in soil properties and their impacts on hydrological processes. Differences in hydraulic conductivity values indicate varying permeability levels influenced by soil texture and composition. Silt loam consistently shows higher conductivity in upper layers, while sandy loam prevails in deeper layers.

Examining Van Genuchten parameters, Rosetta analysis predicts relatively consistent porosity values compared to the wider range observed in laboratory result. The Multipoint triangle method identifies predominant soil types, with silt loam dominating upper layers due to agricultural practices, while deeper layers exhibit diverse compositions influenced by geological factors. Finally, through SCE-UA method, the model generates calibrated hydraulic and VGM parameters, including a hydraulic conductivity (K_s) of 22.4 cm/day for silt loam, saturated porosity (θ_s) of 0.367, n of 1.28, residual porosity (θ_r) of 0.0912, and inverse α of 0.229.

The preliminary simulation starts with the water content. The first borehole's water content computation multiplies CATHY's water saturation values by the assigned porosity for its four layers. However, simulations do not perfectly matched the observed data, especially at 0.3 m depth where they underestimate. Improvement is seen at 0.5 m and 0.7 m depths, but some disparity remains. For the second borehole, water content closely aligns with assigned porosity, mirroring the trends observed in the first borehole. However, some deviations occur, notably at 0.5 m depth, indicating adjustments needed in porosity values to address underestimation.

In the third borehole, simulations presents notable challenges, with significant overestimations across most depths, except at 0.7 m depth. This discrepancy highlights inconsistencies in the assigned porosity values. Similar water content patterns are observed in the fourth borehole, with the water content dynamic patterns mirroring those of the third borehole. Despite this, simulations struggle to accurately replicate observed trends and the discrepancies also persist in the fifth borehole, notably at shallower depths of 0.1 m and 0.3 m,

where simulations consistently underestimate water content. While relatively closer matches are observed at depths of 0.5 m and 0.7 m, simulations still exhibit an underestimation trend.

According to the result of calibrated simulation, the assessment of water content dynamics reveals notable discrepancies. While the simulation closely matches observed trends at certain depths in some boreholes, it underestimates water content at others. For instance, in the first boreholes, good alignment is seen at 0.1 m depth, but there is significant underestimations at 0.3 m and 0.5 m. Similarly, the second borehole shows close alignment at some depths but underestimates at others. In the third borehole, there are consistent underestimations, especially at 0.7 m depth. Then, the fourth borehole also exhibits underestimations across all depths, indicating modeling limitations. Likewise, the fifth borehole simulations struggles to replicate observed trends, particularly at deeper depths.

The comparison of pressure head dynamics between observed and simulated data from multiple boreholes reveals challenges in hydrological modeling. Discrepancies, especially during specific time periods, emphasize the need for continuous and comprehensive data collection for accurate model calibration and validation in the first borehole. Additionally, the absence of data for certain depths complicates comparisons, indicating limitations in capturing temporal variations. Similarly, the second borehole exhibits challenges in replicating observed trends. In the third and fourth boreholes, substantial data gaps hinder accurate assessment of simulation accuracy, particularly during specific time intervals. Lastly, in the fifth borehole, significant data absence occurred leading to challenges in replicating trends of observed data, particularly at depths of 0.3 m and 0.5 m. Despite commendable accuracy in capturing pressure head fluctuations, discrepancies persist between simulated and observed data.

From the calibrated simulation, the first borehole has a notable trend deviations between the simulated and the observed data, especially at depths of 0.3 m and 0.5 m. The absence of observed data at certain period also complicates accurate comparison. Similar challenges are seen in the second borehole, where the simulated results are not able to generate the observed trends, particularly at deeper depths. Data gaps in the third and fourth boreholes hinder accurate assessment of simulation accuracy. Despite efforts, challenges persist in the fifth borehole due to data absence. Overall, continued refinement of model is still needed and necessary to improve accuracy in replicating the pressure head dynamics of field measurements.

The comparison of water table levels between simulated and observed data reveals some interesting patterns from the preliminary result (figure 16 to Figure 20). Initially, the simulated

values consistently underestimate the observed water levels, especially noticeable in the first borehole. However, as we move to later figures, this gap between simulated and observed values narrows, showing better alignment.

Similarly, Figures 32 to 36 illustrate the comparison between calibrated simulation and observed data. Notably, in Figure 32, there's a persistent underestimation trend in the first borehole, gradually improving in later figures. Interestingly, a transition from underestimation to overestimation occurs in the calibrated data. Overall, the preliminary results present a batter water table dynamic behaviour than the calibrated results. These findings highlight the need for further model refinement to accurately capture water content dynamics across borehole depths.

A statistical analysis is also conducted to evaluate the hydrological model performance. Table 8 presents the KGE index of water content, revealing varying performance improvements at some layer for certain borehole. The highest value observed on the third borehole at the 0.1 m depth with the value of 0.785. However, some decrease are also observed with the lowest index recorded at -5.218. In Table 9, the KGE index is pointed for pressure head. Notably, the performance indexes decreased after calibration for the whole layers, except at the 0.5 depth in the first borehole with the index of 0.133. The lowest index is -25.709 at 0.1 m depth in the first borehole. Regarding water table analysis, the model performance shows a consistent decrease of KGE index in every boreholes, except in the first borehole increasing from -2.25 to -0.224.

Table 8. Kling-Gupta Efficiency Index for water content

Water Content	0.1 M		0.3 M		0.5 M		0.7 M	
	Preliminary	Calibrated	Preliminary	Calibrated	Preliminary	Calibrated	Preliminary	Calibrated
S1	-0.172	0.733	0.068	-4.257	0.013	-2.348	-0.078	-0.133
S2	-0.099	0.479	-0.001	-1.932	-0.095	0.363	-0.135	0.315
S3	-0.078	0.785	-0.082	0.451	-0.104	0.462	-0.082	-0.253
S4	-0.193	-0.863	-0.036	0.085	0.015	-5.218	-0.026	-0.873
S5	-0.096	0.749	-0.139	0.451	-0.120	-0.388	-0.330	-9.757

Table 9. Kling-Gupta Efficiency Index for pressure head

Pressure Head	0.3 M		0.5 M		0.7 M	
	Preliminary	Calibrated	Preliminary	Calibrated	Preliminary	Calibrated
S1	-0.009	-25.709	-0.251	0.133		
S2	-0.307	-0.866	0.338	-14.162	0.436	-4.121
S3	-0.371	-1.076	0.316	-20.399		
S4	-0.231	-0.903	-0.053	-3.803	-0.287	-6.378
S5	-0.251	-0.251	0.017	-2.544		

Table 10. Kling-Gupta Efficiency Index for water table

Water Table	0.3 M	
	Preliminary	Calibrated
S1	-2.250	-0.224
S2	0.424	-0.435
S3	0.394	-0.599
S4	0.494	-0.508
S5	0.446	-0.509

Hence, analysis of water content dynamics shows discrepancies between simulated and observed data across boreholes. Some alignment is seen, but underestimations persist, highlighting modeling limitations. Challenges also arise in replicating pressure head dynamics due to data gaps. Water table comparisons initially show underestimations, improving over time but still showing discrepancies. Statistical analysis confirms varies model performance, emphasizing the need for continuous data collection and model refinement for accurate predictions. Ongoing efforts are essential to improve the model's accuracy in capturing water dynamics.

In summary, the calibrated model did not perform as well as it was expected. This can be due to several reasons. First, the fact that the preliminary simulation was calibrated against water table measurements only. That is why the preliminary model performs better than the calibrated model for water table. As a consequence, also pressure head is captured relatively well by the preliminary model, as it is strongly correlated with the water table dynamics. However, despite the KGE for pressure head in the calibrated model being worse than the preliminary model, the dynamics is sometimes better captured by the former, which is able to simulate larger pressure head fluctuations that appear also in the measurements. This indicates that KGE might not be the best objective function in this kind of calibration exercise. In future developments, maybe other metrics (e.g., RMSE) can be tried. Finally the water content, which was not considered in the preliminary model calibration, improves significantly in the newly calibrated model that takes it into account. All these aspects highlight challenges that multi objective calibration (trying to match water table, pressure head, and water content simultaneously) poses in integrated surface-subsurface hydrological modelling. Also, different SCE-UA parametrizations and a better characterization of initial conditions could have helped improve the model performance, but due to lack of time this has been left for future developments.

REFERENCES

[1] Bakker, Mark & Schaars, Frans. (2019). Solving Groundwater Flow Problems with Time Series Analysis: You May Not Even Need Another Model. Groundwater. 57. 10.1111/gwat.12927

[2] Bergström, Sten & Lindström, Göran & Pettersson, Anna. (2002). Multi-Variable Parameter Estimation to Increase Confidence in Hydrological Modeling. Hydrological Processes. 16. 413 - 421. 10.1002/hyp.332.

[3] Boyle DP. 2001. Multicriteria calibration of hydrologic models. PhD dissertation, Department of Hydrology and Water Resources, University of Arizona, Tucson, AZ.

[4] Budyko, M. I. (1961). The heat balance of the earth's surface. Soviet Geography, 2(4), 3-13.

[5] Camporese, M., Paniconi, C., Putti, M., & Orlandini, M. (2010). Surface-subsurface flow modeling with path-based runoff routing, boundary condition-based coupling, and assimilation of multisource observation data. Water Resources Research, 46, 1 - 22. https://doi.org/10.1029/2008WR007536

[6] Camporese, .M., Daly, .E., Dresel, P.E., Webb, John.A (2014), Simplified modeling of catchment-scale evapotranspiration via boundary condition switching, Advances in Water Resources, Volume 69, Pages 95-105, ISSN 0309-1708. https://doi.org/10.1016/j.advwatres.2014.04.008.

[7] Camporese, M., E. Daly, and C. Paniconi (2015), Catchment-scale Richards equation-based modeling of evapotranspiration via boundary condition switching and root water uptake schemes, Water Resour. Res., 51, 5756–5771, doi:10.1002/ 2015WR017139.

[8] Carbognin, L.; Tosi, L. Il Progetto ISES per L'analisi dei Processi di Intrusione Salina e Subsidenza nei Territori Meridionali delle Province di Padova e Venezia; Istituto per lo Studio della Dinamica delle Grandi Masse, Consiglio Nazionale di Ricerca: Venice, Italy, 2003; pp. 16–88.

[9] Carbognin, L.; Teatini, P.; Tosi, L. Land subsidence in the Venetian area: Known and recent aspects. G. Geol. Appl. 2005, 1, 5–11.

[10] Carsel, R.F. and Parrish, R.S. (1988). Developing joint probability distributions of soil water retention characteristics. Water Resources Research 24: doi: 10.1029/88WR01772. issn: 0043-1397.

[11] Da Lio, C.; Carol, E.; Kruse, E.; Teatini, P.; Tosi, L. Saltwater contamination in the managed low-lying farmland of the Venice coast, Italy: An assessment of vulnerability. Sci. Total Environ. 2015, 533, 356–369. [CrossRef]

[12] Duan, Q., Sorooshian,S. and Gupta, V.K., 1992. Effective and efficient global optimization for conceptual rainfall-runoff models.Water Resour. Res.,28(4):1015-1031

[13] Duan, Q., Gupta, V.K. and Sorooshian,S., 1993. A shuffled complex evolution approach for effective and efficient optimization. J. Optimization Theory Appl., 76(3):501-521.

[14] EEA (2018) European Waters Assessment of Status and Pressure 2018. EEA Report, 7/2018, vol. 2018, European Environmental Agency, Publications Office of the European Union, Luxembourg. Available: https://www.eea.europa.eu/publications/state-of-water.

[15] Feddes, R.A., E. Bresler, and S.P. Neuman. 1974. Field test of a modified numerical model for water uptake by root systems. Water Resour. Res. 10:1199–1206. doi.org/10.1029/WR010i006p01199

[16] Gambolati, G.; Putti, M.; Teatini, P.; Gasparetto-Stori, G. Subsidence due to peat oxidation and impacts on drainage infrastructures in a farmland catchment south of the Venice Lagoon. Environ. Geol. 2006, 49, 814–820. [CrossRef]

[17] Gupta, Hoshin & Sorooshian, Soroosh & Yapo, Patrice. (1998). Toward improved calibration of hydrologic models: Multiple and noncommensurable measures of information. Water Resources Research - WATER RESOUR RES. 34. 10.1029/97WR03495.

[18] Holland, J.H., 1975. Adaptation in Natural and Artificial Systems. University of Michigan Press, Ann Arbor.

[19] Hopmans, J. M., Simunek, J., Romano, N., & Durner, W. (2002). Inverse methods. In J. H. Dane & G. C. Topp (Eds.), Methods of soil analysis, part 4: Physical methods. Soil Science Society of America.

[20] Hoshin V. Gupta, Harald Kling, Koray K. Yilmaz, Guillermo F. Martinez, 2009. Decomposition of the mean squared error and NSE performance criteria: Implications for improving hydrological modelling. Journal of Hydrology. Volume 377, Issues 1–2, Pages 80-91, ISSN 0022-1694. https://doi.org/10.1016/j.jhydrol.2009.08.003.

21] Madsen, Henrik & Wilson, Geoffrey & Ammentorp, Hans. (2002). Comparsion of Different Automated Strategies for Calibration of Rainfall-Runoff Models. Journal of Hydrology. 261. 48-59. 10.1016/S0022-1694(01)00619-9.

[22] Manetsch, T.J., 1990. Towards efficient global optimization in large dynamic systems--adaptive complex method. IEEE Trans. Syst. Man Cybernet., 20(1): 257-261

[23] Mondal, N.C.; Singh, V.P.; Singh, V.S.; Saxena, V.K. Determining the interaction between groundwater and saline water through groundwater major ion chemistry. J. Hydrol. Hydrol. 2010, 388, 100–111. [CrossRef]

[24] Mulligan, A.E.; Evans, R.L.; Lizarralde, D. The role of paleochannels in groundwater/seawater exchange. J. Hydrol. 2007, 335, 313–329. [CrossRef]

[25] Nelder, J.A. and Mead, R., 1965. A Simplex method for function minimization. Comput. J., 7: 308-313.

26 Orlandini, S., and R. Rosso (1996), Diffusion wave modeling of distributed catchment dynamics, J. Hydrol. Eng., 1(3), 103–113.

[27] Orlandini, S., and R. Rosso (1998), Parameterization of stream channel geometry in the distributed modeling of catchment dynamics, Water Resour. Res., 34(8), 1971–1985.

[28] Paniconi, C., and E. F. Wood (1993), A detailed model for simulation of catchment scale subsurface hydrologic processes, Water Resour. Res., 29(6), 1601–1620.

[29] Paniconi, C., and M. Putti (1994), A comparison of Picard and Newton iteration in the numerical solution of multidimensional variably saturated flow problems, Water Resour. Res., 30(12), 3357–3374.

[30] Price, W.L., 1978. A controlled random search procedure for global optimization. In: C.W.L. Dixon and G.P. Szego (Editors), Towards Global Optimization, 2. North-Holland, Amsterdam, pp. 71-84.

[31] Price, W.L, 1983. Global optimization by controlled random search. J. Optimization Theory Appl., 40(3): 333-348.

[32] Pulido-Leboeuf, P.; Pulido-Bosh, A.; Calvache, M.L.; Vallejos, Á.; Andreu, J.M. Strontium, SO42−/Cl− and Mg2+/Ca2+ ratios as tracers for the evolution of seawater into coastal aquifers: The example of Castell de Ferro aquifer (SE Spain). Comptes Rendus Geosci. 2003, 335, 1039–1048. [CrossRef]

[32] Ritzema, Henk & Heuvelink, Gerard & Heinen, Marius & Bogaart, Patrick & Bolt, Frank & Hack-ten Broeke, Mirjam & Hoogland, Tom & Knotters, M. & Massop, H. & Vroon, H.R.J. & van den Bosch, Hendrik. (2018). Review of the methodologies used to derive groundwater characteristics for a specific area in The Netherlands. Geoderma Regional. 14. e00182. 10.1016/j.geodrs.2018.e00182.

[33] Scudiero, E.; Teatini, P.; Corwin, D.L.; Dal Ferro, N.; Simonetti, G.; Morari, F. Spatiotemporal Response of Maize Yield to Edaphic and Meteorological Conditions in a Saline Farmland. Agron. J. 2014, 106, 2163–2174. [CrossRef]

[34] Sebben, M. L., A. D. Werner, J. E. Liggett, D. Partington, and C. T. Simmons (2013), On the testing of fully integrated surface–subsurface hydrological models, Hydrol. Processes, 27, 1276–1285, doi:10.1002/hyp.9630.

[35] Sorooshian, S., Duan, Q. and Gupta, V.K., 1993. Calibration of conceptual rainfall-runoffmodels using global optimization: application to the Sacramento soil moisture accounting model. Water Resour. Res., 29(4): 1185-1194.

[36] Sposito, G. (2017). Understanding the Budyko equation. Water, 9(4), 236.

[37] U.S. Army Corps of Engineers. (1999). Engineering and Design GROUNDWATER HYDROLOGY. Washington, DC. EM 1110-2-1421.

[38] Van Genuchten, M. T. (1980). A closed-form equation for predicting the hydraulic conductivity of unsaturated soils 1. Soil Sci. Soc. Am. J. 44, 892–898.

[39] Viezzoli, A.; Tosi, L.; Teatini, P.; Silvestri, S. Surface water-groundwater exchange in transitional coastal environments by airborne electromagnetics: The Venice Lagoon example. Geophys. Res. Lett. 2010, 37, L01402. [CrossRef]

[40] Wang, Q.J., 1991. The genetic algorithm and its application to calibrating conceptual rainfall-runoff models. Water Resour. Res., 27(9): 2467-2471.

[41] Werner, A.D.; Bakker, M.; Post, V.E.A.; Vandenbohede, A.; Lu, C.; Ataie-Ashtiani, B.; Simmons, C.T.; Barry, D.A. Seawater intrusion processes, investigation and management: Recent advances and future challenges. Adv. Water Resour. 2013, 51, 3–26. [CrossRef]